Development of a novel electromagnetic groundwater flowmeter

Ben Mitchell
B.E. (Hons I)

A thesis presented for the degree of
Doctor of Philosophy
in
Electrical and Computer Engineering
at the
University of Canterbury,
Christchurch, New Zealand.

30 September 2021

ABSTRACT

The concept and implementation of an electromagnetic flowmeter has, until now, remained focused on industrial plant applications and oceanographic measurements. This thesis applies the existing body of electromagnetic flowmeter work to the problem of groundwater measurement. The theoretical framework provided by Shercliff and Bevir is applied to larger geometries through the construction of numerical simulations. The simulations provide the expected sensitivities for a given flowmeter and electrode geometry combination. A model of the measurable signals is constructed and applied through the use of linear least squares estimators. A pre-whitening filter is described to mitigate the low frequency $1/f$ noise as well as a gating algorithm to reduce the effects of the magnetic interference. The concept groundwater flowmeter is tested on two different geometries in the laboratory, at a range of excitation frequencies. The moving gantry laboratory experiments at 1 Hz yield a flow signal of 400 nV, compared to the simulation result of 600 nV. However, the results from a mini aquifer we less conclusive, presumed to be due to the magnetic interference changing with flow speed. An unexpected frequency dependence is present in the measured data preventing accurate results above 1 Hz. This is presumed to be a result of the coil power supply design. A likely source of zero offset drift is also identified as the magnetically coupled interference.

Deputy Vice-Chancellor's Office
Postgraduate Office

UNIVERSITY OF CANTERBURY
Te Whare Wānanga o Waitaha
CHRISTCHURCH NEW ZEALAND

Co-Authorship Form

This form is to accompany the submission of any thesis that contains research reported in co-authored work that has been published, accepted for publication, or submitted for publication. A copy of this form should be included for each co-authored work that is included in the thesis. Completed forms should be included at the front (after the thesis abstract) of each copy of the thesis submitted for examination and library deposit.

Publication 1: Bonnett, B., Mitchell, B., Frampton, M., and Hayes, M. [2019], 'Low-noise instrumentation for electromagnetic groundwater flow measurement', In *IEEE International Instrumentation and Measurement Technology Conference (I2MTC).*

Some material from this publication is presented in Chapter 1 and Chapter 4, including Figures 4.2 and 4.3.

Publication 2: Hayes, M., Mitchell, B., Bonnett, B., Frampton, M., and Heffernan, B. [2019], 'Tank-tests of a Prototype Electromagnetic Groundwater Flowmeter', In *IEEE International Instrumentation and Measurement Technology Conference (I2MTC).*

Some material from this publication is presented in Chapter 4.

Publication 3: Mitchell, B., Hayes, M., and Heffernan, B. [2021], 'Modelling for an Electromagnetic Groundwater Flowmeter', In *IEEE International Instrumentation and Measurement Technology Conference (I2MTC),* (accepted for publication).

Material and results presented in this thesis is used throughout the publication, specifically the figures.

Please detail the nature and extent (%) of contribution by the candidate:

Publication 1: Requirements and specifications developed through discussions between candidate and M. P. Hayes. Hardware designs developed by B. Bonnett and the candidate. Software written by B. Bonnett, M. Frampton, and the candidate. Results and validation performed by B. Bonnett. Written content developed by B. Bonnet and the candidate, with the other authors providing review. 30% of the development, and 20% of the writing provided by the candidate.

Publication 2: Methodology developed through discussions between candidate and M. P. Hayes. Hardware developed by all authors. Experimental results collected by the

candidate and processed using software written by the candidate. 60% of the research, 40% of the writing, and 80% of the figures was contributed by the candidate.

Publication 3: Methodology developed through discussions between candidate and M. P. Hayes. Simulation software built by the candidate. Simulations designed and run by the candidate. Results collected and presented in this thesis. Text written by M. P. Hayes with review and feedback from candidate. 75% of the research and 100% of figures contributed by the candidate.

Certification by co-authors

If there is more than one co-author then a single co-author can sign on behalf of all. The undersigned certifies that:

- The above statement correctly reflects the nature and extent of the PhD candidate's contribution to this co-authored work
- In cases where the candidate was the lead author of the co-authored work, he or she wrote the text.

Name: *Dr Michael P. Hayes* Signature: MPH Date: *30 September 2021*

ACKNOWLEDGEMENTS

My two supervisors, Michael Hayes and Bill Heffernan: thank you for never accepting the simple answer. I greatly appreciate your guidance and suggestions, especially during the many periods of confusion. Mostly, I am grateful for showing me how to think outside of the box when it comes to solving sticky problems. Thank you very much for your continual support.

A big thank you to the departments mechanical technicians: Paul Agger, David Healy, and Nigel Pink. I would never have been able to achieve physical experiments without your help. As for Scott Lloyd: it has been a pleasure to work with you all these years. I wish you good luck with future cohorts.

A special thank you to my fellows through our various postgraduate adventures, Byron, Tom, and Eugene. Thanks for always being there. Our lunchtime chats were always a highlight, and most importantly, you've helped me understand the true differences between a boat and a ship.

Finally, to my family. None of this would have been possible without your guidance and support. Thank you all.

PREFACE

This thesis aims to apply electromagnetic flowmeter (EMFM) methods to the measurement of groundwater flows. Chapter 1 provides the history and context of the EMFM, as well as some of the principles behind groundwater flow. Chapter 2 describes geometries and simulations of the EMFM method to determine expected sensitivities. Chapter 3 describes how the raw measurements are processed into useful flow signals and Chapter 4 covers the laboratory equipment. Chapters 5 and 6 describe the experiments and results for two different experiment rigs. Finally Chapter 7 provides a summary of the presented research.

This work was particularly challenging as there is sizeable literature surrounding EMFMs, but little on their use outside a narrow range of industrial cases. The trial experiments performed would work sometimes, but not others, seemingly at random. Interference would spontaneously show up in the recorded data that had never been seen previously, often from bizarre and unexpected sources (see Appendix B) which had not been encountered in previous works. The exacting precision required in the measurements required the systematic amelioration of these problems. This also challenged various assumptions, such as that running with a higher excitation frequency, and thus reducing the effects of $1/f$ noise, would result in a more accurate result.

Part of the research presented involved the design and implementation of a high dynamic range instrumentation system, and a novel magnetic field interference nulling device. A large amount of custom software was also authored including a three dimensional finite-difference method (FDM) flowmeter simulator and a complete signal processing pipeline. Some tools utilised in the research were developed by colleagues in the department. Specifically, the final version of the instrumentation were primarily built and programmed by Blair Bonnet and Mike Frampton [Bonnett et al. 2019], as well as the coil power supply which was designed by Bill Heffernan [Heffernan et al. 2020]. These projects were instrumental to the completion of this thesis, and as such the author was involved in their implementations.

The research presented here was funded as a part of the Science for Technological Innovation (SfTI) National Science Challenge: Inverting Electromagnetics project. This work would not have been possible without the contributions from the various academic and commercial partners in the project.

PUBLICATIONS

The following papers were published during the course of this thesis:

Hayes, M. P., Mitchell, B., Bonnet, B., and Heffernan, B. (2017). 'Preliminary results from an electromagnetic groundwater flow measurement system', In *Electronics New Zealand Conference (ENZCon)*, New Zealand.

Mitchell, B., Bonnet, B., and Hayes, M. P. (2017). 'Measurement of nanovolt-scale signals for electromagnetic groundwater flow determination', In *Electronics New Zealand Conference (ENZCon)*, New Zealand.

Bonnett, B., Mitchell, B., Frampton, M., and Hayes, M. (2019). 'Low-noise instrumentation for electromagnetic groundwater flow measurement', In *2019 IEEE International Instrumentation and Measurement Technology Conference (I2MTC).*

Hayes, M., Mitchell, B., Bonnett, B., Frampton, M., and Heffernan, B. (2019). 'Tank-tests of a Prototype Electromagnetic Groundwater Flowmeter', In *2019 IEEE International Instrumentation and Measurement Technology Conference (I2MTC).*

Heffernan, B., Mitchell, B., and Hayes, M. (2020, May). 'Trapezoidal Current Generator for an Electromagnetic Groundwater Flowmeter', In *2020 IEEE International Instrumentation and Measurement Technology Conference (I2MTC).*

Mitchell, B., Hayes, M., and Heffernan, B. (2020). 'Nonlinear System Identification for an Electromagnetic Groundwater Flowmeter', In *2020 IEEE International Instrumentation and Measurement Technology Conference (I2MTC).*

CONTENTS

Glossary

AC	alternating current
ASD	amplitude spectral density
BVP	bounding value problem
CPE	constant-phase element
DC	direct current
EMFM	electromagnetic flowmeter
EMI	electromagnetic interference
ETI	electrode tissue interface
FDM	finite-difference method
FPGA	field programmable gate array
GLS	generalised least squares
MCU	microcontroller
OLS	ordinary least squares
PCB	printed circuit board
PMFM	permanent magnet flowmeter
PSD	power spectral density
SDR	software defined radio
SfTI	Science for Technological Innovation
SNR	signal-to-noise ratio

Nomenclature

$\mathbf{x}$	Bold script denotes a vector, usually $\in \mathbb{R}^3$	
$\hat{x}$	Estimate for the value of x	
∇f	Gradient of the scalar field $f \in \mathbb{R}$, equivalent to $(\frac{\partial f}{\partial x}, \frac{\partial f}{\partial y}, \frac{\partial f}{\partial z})^T$	
$\nabla \cdot \mathbf{f}$	Divergence of the vector $\mathbf{f} \in \mathbb{R}^3$, equivalent to $\frac{\partial f_x}{\partial x} + \frac{\partial f_y}{\partial y} + \frac{\partial f_z}{\partial z}$	
$\nabla^2 f$	Laplacian of the scalar field $f \in \mathbb{R}$, equivalent to $\frac{\partial^2 f}{\partial x^2} + \frac{\partial^2 f}{\partial y^2} + \frac{\partial^2 f}{\partial z^2}$	
σ	Conductivity	$\mathrm{S\,m^{-1}}$
$\mathbf{B}$	Magnetic flux density	T
$\mathbf{E}$	Electric field	$\mathrm{V\,m^{-1}}$
$\mathbf{J}$	Current density	$\mathrm{A\,m^{-2}}$
$\mathbf{J}^V$	Virtual current density	$\mathrm{m^{-2}}$
$\mathbf{n}$	Surface normal	unitless
$\mathbf{u}$	Water velocity	$\mathrm{m\,s^{-1}}$
$\mathbf{W}$	Bevir weight vector	$\mathrm{T\,m^{-2}}$
I	Electric current	A
k	Flowmeter geometry scale factor	unitless
S	Flowmeter sensitivity	V/A/(m/s)
V	Electric potential	V

Chapter 1

INTRODUCTION AND HISTORY

Groundwater is one of the few sources of potable water available for people and agriculture. Half of New Zealand's population uses groundwater as a primary source of drinking water [Rosen et al. 2001]. On a global scale, groundwater comprises 30% of the total fresh water [Gleick 1996]. With the majority of the fresh water locked in the form of ice caps, glaciers, and snow; groundwater makes up over 98% of the remaining available water [Fetter 2001]. The importance of having reliable access to clean drinking water was recognised by the United Nations in 2010.

Making land-use decisions to improve water quality requires accurate knowledge of groundwater flow [Lovett and Cameron 2015]. Existing models for groundwater flow are built and tuned using measurements from monitored wells. These wells are expensive and difficult to drill, and as such the data points are sparse resulting in a lack of spatial knowledge of water flows.

1.1 ELECTROMAGNETIC FLOWMETER

A form of EMFM was first theorised by electrical pioneer Michael Faraday in the 1800s. Since then, discoveries have been made by other researchers, such as Charlton Wollaston who was able to measure the effects proposed by Faraday. The first modern flowmeter was created by Williams [1930] in his attempts to observe the flow velocity distribution in a pipe. Oceanographers have also attempted to use the EMFM methodology to measure the currents of large bodies of water, with varying degrees of success, in the English Channel [Bowden 1956] and Irish Sea [Bowden and Hughes 1961, Robinson and Deacon 1976]. Recent developments in the last century have enabled a more analytical approach to flowmeter design [Bevir 1970]. The EMFM approach has been extended to cover poorly conducting fluids such as transformer oil [Cushing 1965] and industrial fuels [Amare 1999]. Modern computing power has also enabled numerical solutions to complex geometries and boundary conditions [Michalski et al. 1988]. The simplicity and reliability of the modern EMFM has made it one of the default choices for a variety of industrial cases, and even in hostile environments such as flow measurement in

radioactive liquid metal circuits in nuclear reactors [Shercliff 1962]. This chapter covers the history of the EMFM, its governing principles, and describes modern developments on this technology.

1.2 OPERATING PRINCIPLE

The operating principle of an EMFM can be derived from Ohm's law

$$\mathbf{J} = \sigma(\mathbf{E} + \mathbf{u} \times \mathbf{B}) \,, \tag{1.1}$$

where $\mathbf{J}$ is the electrical current density, $\mathbf{E}$ is the electric field, $\mathbf{u}$ is the conductor velocity (in this case the water velocity), $\mathbf{B}$ is the magnetic flux, and σ is the electrical conductivity, which is assumed to be homogeneous and isotropic. If the $\mathbf{B}$ field is constant with time, then $\mathbf{E}$ is a conservative field defined by

$$\mathbf{E} = -\nabla V, \tag{1.2}$$

with V being the electric potential. Substituting (1.2) into (1.1), the current density becomes

$$\mathbf{J} = \sigma(-\nabla V + \mathbf{u} \times \mathbf{B}) \,. \tag{1.3}$$

Note the current density (the eddy currents) produce an opposing magnetic field to $\mathbf{B}$ but this is assumed to be negligible since the water is a poor conductor. Taking the divergence of $\mathbf{J}$, assuming σ is constant, gives

$$\nabla \cdot \mathbf{J} = \sigma(-\nabla \cdot \nabla V + \nabla \cdot (\mathbf{u} \times \mathbf{B})) \,. \tag{1.4}$$

From the continuity of current, the divergence of the current density is zero, so

$$\nabla \cdot \mathbf{J} = 0 \,, \tag{1.5}$$

which leads to a form of Poisson's equation

$$\nabla \cdot \nabla V = \nabla^2 V = \nabla \cdot (\mathbf{u} \times \mathbf{B}) \,. \tag{1.6}$$

In other words, the magnetic field interacting with the moving water sets up a measurable electric field orthogonal to both the magnetic and flow fields. If the boundary conditions for the problem can be determined, then the solution for V leads to the practical implementation of an EMFM. This can be solved numerically for specific geometries such as a pipe, an experiment tank, or a field test site. Figure 1.1 shows the geometry of a typical pipe flowmeter where the potential difference can be measured.

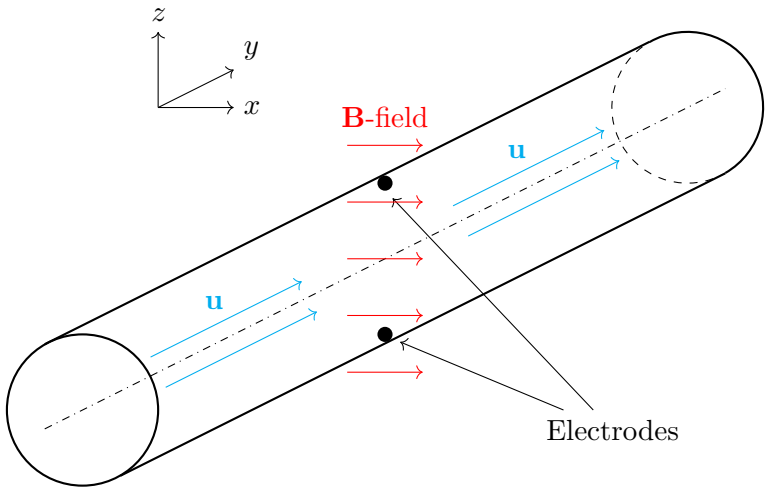

Figure 1.1 The typical layout in a modern EMFM. The transverse **B** field is designed to be as uniform as possible and is aligned orthogonal to **u** in order to maximise the $\mathbf{u} \times \mathbf{B}$ effect. The electrodes are arranged on the pipe walls, perpendicular to both the **B** field, and the flow velocity **u**. They are shown here as points but often larger plate electrodes are used instead. The axes are aligned such that the flow vector is rectilinear, $\mathbf{u} = (0, u_y, 0)$.

1.3 EARLY ATTEMPTS

Some early attempts at using the EMFM principles were performed by Faraday [1832]. The experiment consisted of two metal plates, which were connected to a galvanometer, being lowered from Waterloo bridge into the fast current of the river Thames. The aim was to show the effect of the water interacting with the Earth's magnetic field and generating a measurable current. Ultimately the experiment failed, likely due to the riverbed short-circuiting much of the genuine signal leaving only random noise caused by electrochemical and thermoelectric effects [Shercliff 1962].

Wollaston [1881] describes an experiment performed in 1851 where a sensitive galvanometer was attached to an under-sea cable running between England and France as shown in Figure 1.2. He recounts "very strong" movement of the needle from "about 40 degrees on the one side to 45 to 48 on the other". These deviations were so strong that he believed his experiment erroneous. After a fortnight of observations every 5 minutes and some time to think, Wollaston came to the conclusion in 1854 that the needle was moving in concert with the tides. The needle would change directions four times a day, the time of the changes varying about 40 minutes from day to day. These results coincided with effects such as Faraday has predicted and during consultation, Faraday remarked "Oh, beautiful, beautiful" [Wollaston 1881].

The results reported by Wollaston indicated a strong correlation with the tidal motion of the English Channel. It is now understood that the vertical component of

;

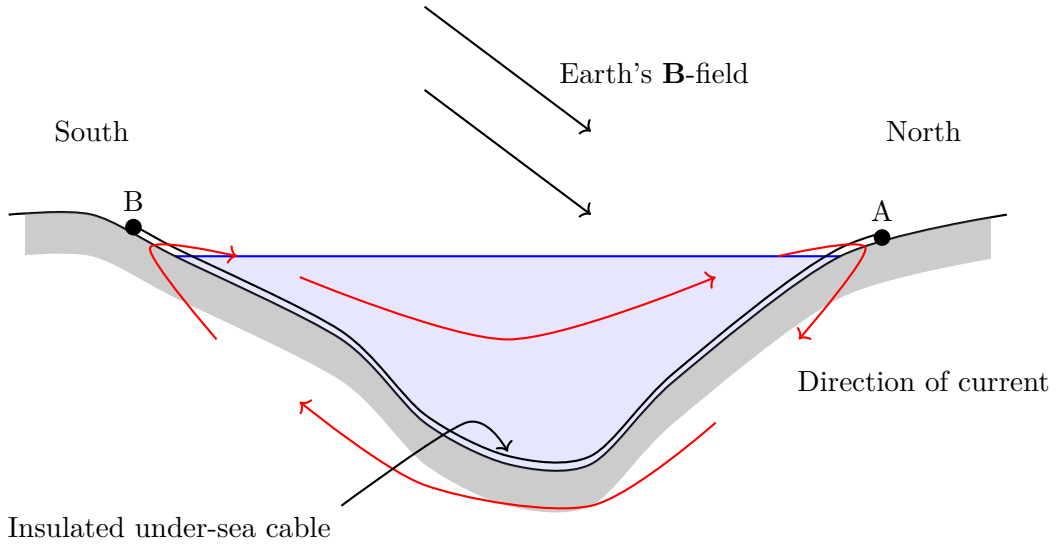

Figure 1.2 Diagram of the typical setup for the early oceanographic flowmeter experiments. The vertical component of the Earth's magnetic field interacting with the water movement down the channel induced an e.m.f. across the channel. The potential difference was measured between the two ground points at stations A and B by breaking the ground connection and inserting instrumentation between the cable and ground. The early pioneers used galvanometers to measure the current flowing through the loop as some would pass through the cable [Wollaston 1881].

the magnetic field would intersect with the east-west flow of water in the channel and produce an electric field in the north-south direction. The electric field induced an electric current to flow through the water and return through the Earth under the channel. In his experiment, Wollaston had essentially connected his galvanometer-cable circuit in parallel with the water and was able to measure some of the electrical current. Figure 1.3 shows a simplified circuit diagram of his experiment. This result, predicted by Faraday and demonstrated by Wollaston, would prove to have great implications and, in fact, launch the field of inductive current flowmeters for oceanographic purposes and eventually the study of modern EMFMs.

The first modern EMFM was proposed by Williams [1930]. He used a 1.075 cm glass tube with one fixed copper electrode, and a second electrode mounted in a brass tube which could, through screw movement, be moved along the measurement axis of the flowmeter. The adjustable electrode was encased in a tight-fitting glass capillary

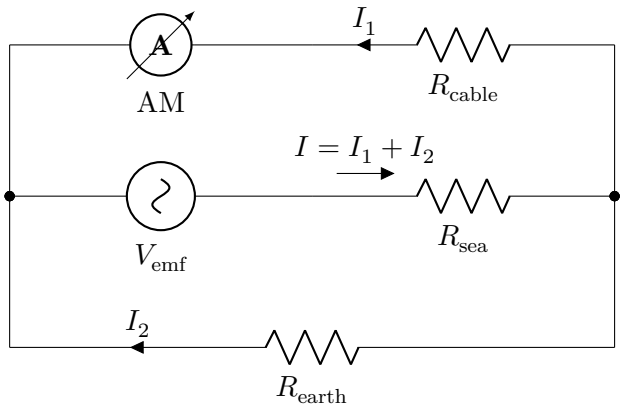

Figure 1.3 Circuit diagram of Wollaston's English Channel experiment. V_{emf} is the voltage source of the moving water interacting with the magnetic field and R_{sea} is the impedance of the myriad paths through the water. R_{earth} is the return path impedance through the ground, and R_{cable} is the impedance of the submarine telecommunications cable. Wollaston's galvanometer (AM) was connected in series with the cable and measured the current through the cable, I_1. The cable and the Earth paths are in parallel and act as a current divider for the return path.

with thin walls to keep it both rigid and insulated. A diagram of the setup is shown in Figure 1.4. A 1 T magnetic field was applied and the potential difference was measured by flipping the polarity of the magnetic field. Williams used this flowmeter to measure the axial velocity distribution of a copper sulfate solution by adjusting the distance between the electrodes, ε, and comparing the measured voltages, $V_P - V_A$, to the total voltage across the tube, $V_B - V_A$. He was able to show that, for a laminar flow, the water moves the fastest in the middle, confirming established theory, and that for a turbulent flow the distribution is flat and much faster at the edges than expected. Figure 1.5 shows his recorded measurements. The difference between laminar and turbulent flow can be clearly seen in the measured voltages and the estimated flow profiles.

1.4 EMPIRICAL MODEL

The use of electromagnetic flowmeters began in earnest in 1936 [Kolin 1945]. These devices typically consisted of a sinusoidal alternating current (AC) magnetic field and a phase sensitive detector. The measurable output was empirically found to be linear, and can be summarised in the form of

$$V = kBuD\,, \tag{1.7}$$

where V is the measured voltage, k is a calibration constant,[1] B is the transverse magnetic field strength, u is the mean flow velocity, and D is the electrode separation (usually the same as the pipe diameter). The industrial adoption of the electromagnetic flowmeter was due to its independence from viscosity, density, and temperature as well

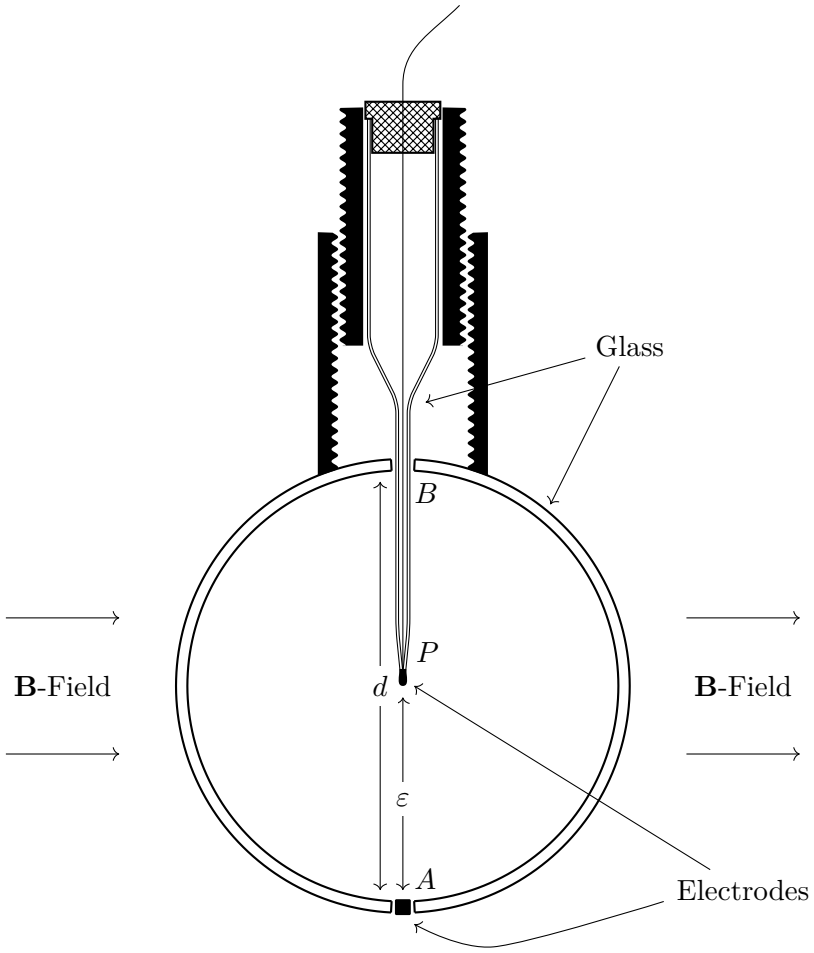

Figure 1.4 Cross-section of Williams' flowmeter, redrawn from Williams [1930]. One electrode is fixed in the bottom of the glass tube while the other can be raised or lowered into the flow stream adjusting ε. A constant transverse magnetic field is applied and the potential difference is measured between the electrodes when the magnetic field is reversed.

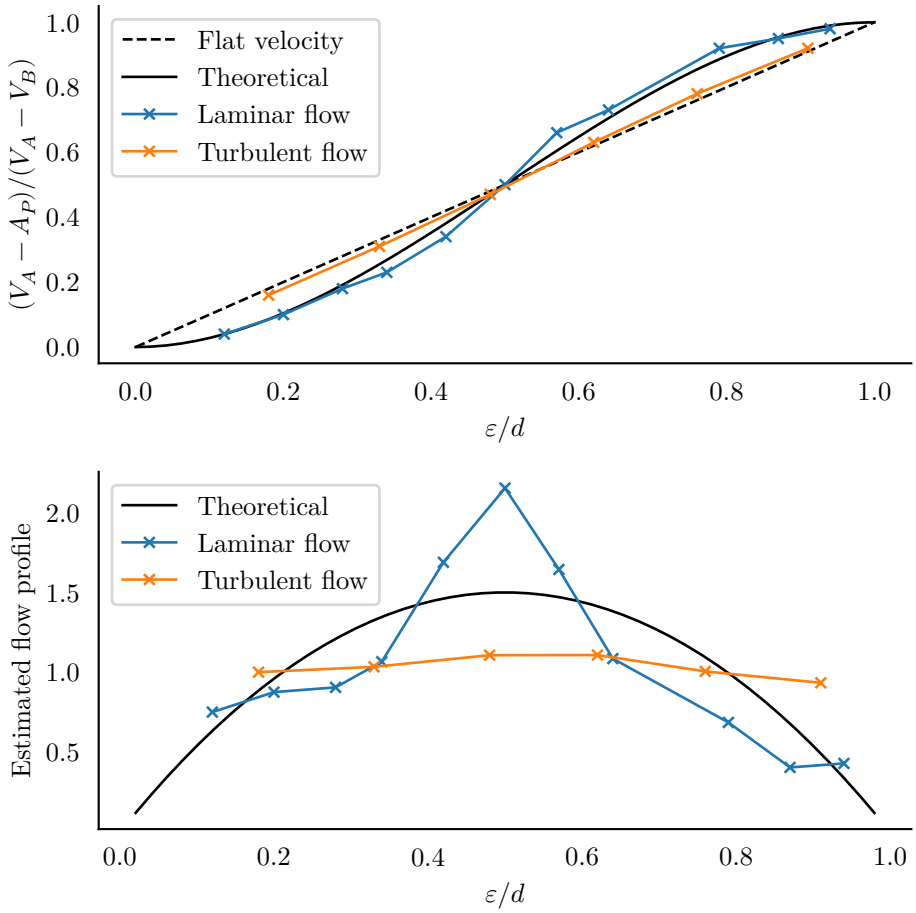

Figure 1.5 Results from Williams' experiment [Williams 1930]. The first plot shows the measured voltage as a fraction of the total voltage across the tube. The stable flow clearly has a stronger voltage contribution around the centre of the tube while the turbulent flow appears to have a constant contribution across the flow. The second plot shows the gradient of the measured voltage and gives an estimate of the flow profile. The laminar flow has a strong peak in the centre of the tube with a much lower speed on the outside as predicted.

as its fast response time.

1.5 SHERCLIFF AND BEVIR

Shercliff [1962] neatly summarises the field of EMFM used in industrial settings, as of 1962. His book lays out the operating principle for an EMFM, and then proceeds to perform a two dimensional analysis for the common flowmeter cases. This is followed by the introduction of the concept of a weight function, $W(x, z)$, which represents the contribution across the flow velocity to the output signal. Figure 1.6 shows Shercliff's weight function for a circular pipe with two point electrodes in a uniform transverse magnetic field. The equation is given as

$$W(x,z) = \frac{a^4 + a^2(x^2 - z^2)}{a^4 + 2a^2(x^2 - z^2) + (x^2 + z^2)^2}\,, \tag{1.8}$$

where a is the inner radius of the pipe wall. This result showed that for flow near the pipe wall the minimum sensitivity is bounded at 1/2, whereas, for flow near the point electrodes the sensitivity can increase without limit. This makes the flowmeter extremely sensitive to turbulent flows around the electrodes. Shercliff suggests ensuring a reasonably long settling length between any violent flow disturbances and the meter to avoid erroneous sensitivity. He points out that "reasonably long" is still vague, but that EMFMs appear less demanding than orifice or Venturi meters.

Shercliff's result is useful for the specific case but struggles with more complex geometry. The main assumption of (1.8) is that the flowmeter is sufficiently long, and that the magnetic field is uniform along this length. In most cases the magnetic field cannot meet this constraint resulting in different weight functions along the length of the pipe. Equation (1.8) also makes assumptions about the geometry and position of the two electrodes and does not allow for geometries such as plate electrodes or a number of point electrodes simulating a virtual plate.

1.5.1 Weight vector

Shercliff's student, M. K. Bevir, proceeded to develop the weight function into a more general weight vector [Bevir 1970, 1969]. A modified derivation of the weight vector, $\mathbf{W}$, is presented here.

Consider Ohm's law with fluid in motion through a flowmeter, such as one in Figure 1.7,

$$\mathbf{J}^m = \sigma\Big[-\nabla V^m + \mathbf{u}\times\mathbf{B}\Big]\,, \tag{1.9}$$

[1] If the flowmeter has uniform flow speed, u, uniform magnetic field B, and the electrodes are placed on the outer walls of the flowmeter, then $k \approx 1$. As these constraints are weakened, k reduces in value which lowers the sensitivity of the flowmeter. Chapter 2 shows simulations of this effect.

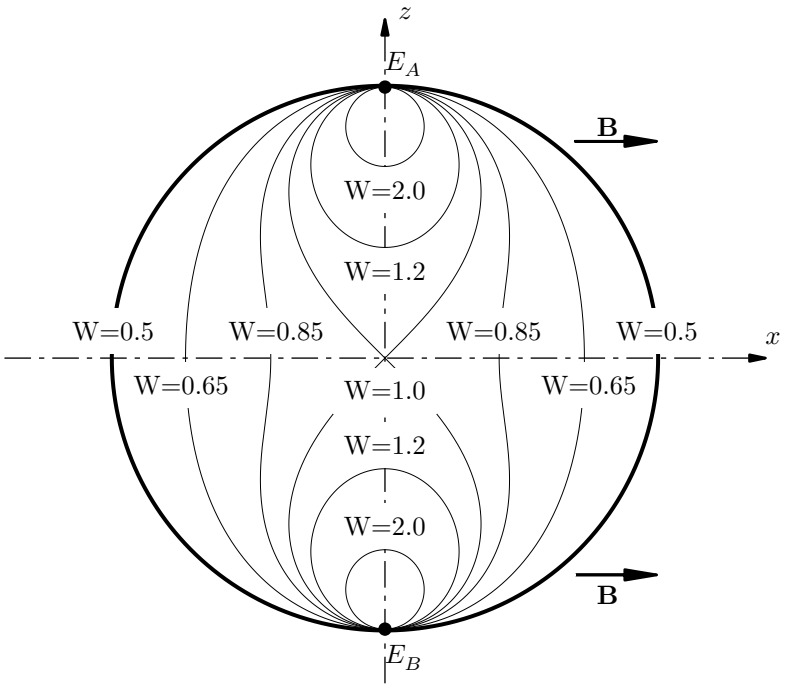

Figure 1.6 Shercliff's weight function, (1.8), for the circular flowmeter geometry shown in Figure 1.1. This shows how water flow near the electrodes disproportionately contribute to the output signal. The weight function has a lower bound of 0.5 at the wall of the pipe but has no upper bound near the electrode. Reproduced from Shercliff [1962].

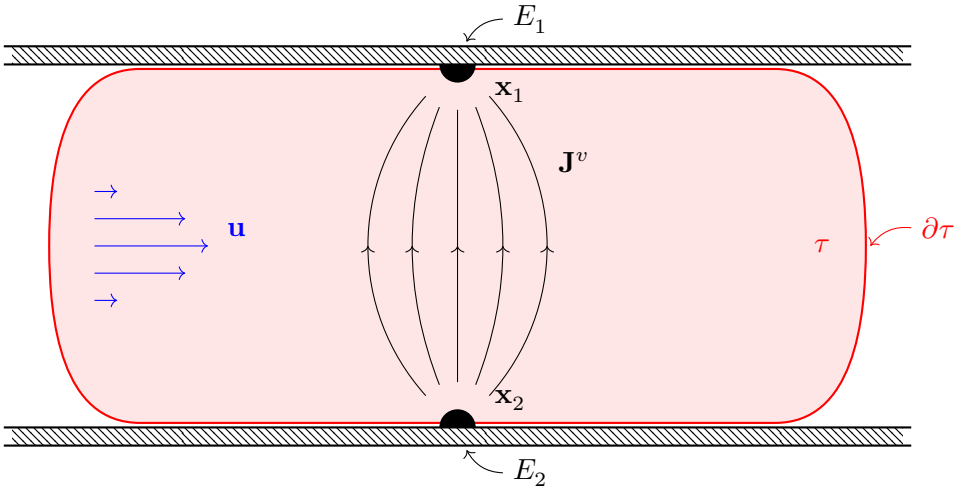

Figure 1.7 A depiction of the geometry for a typical pipe flowmeter. In this scenario the water flows from the left to right. The magnetic field is through the page, and the electrodes are embedded in the walls at positions $\mathbf{x}_1$ and $\mathbf{x}_2$. The volume τ is the volume of the flowmeter with a non-negligible source contribution, and $\partial\tau$ is the boundary of this volume. The virtual current vector, $\mathbf{J}^v$, shown here is the result of 1 A being injected between the electrodes. The magnitude of $\mathbf{J}^v$ is much greater near the electrodes, where the field lines are closer together.

which is equivalent to

$$\nabla V^m = \mathbf{u} \times \mathbf{B} - \frac{1}{\sigma}\mathbf{J}^m \,. \tag{1.10}$$

Green's second identity can be applied to V^m by introducing another function, G, such that

$$\int_\tau \left[V^m \nabla^2 G - G\nabla^2 V^m\right] \mathrm{d}V = \oint_{\partial\tau} \left[V^m \nabla_{\mathbf{n}} G - G\nabla_{\mathbf{n}} V^m\right] \mathrm{d}S\,, \tag{1.11}$$

where τ is the volume of the flowmeter, $\partial\tau$ is the insulating surface of the volume τ, $\mathbf{n}$ is the normal of the surface $\partial\tau$, and $\nabla_{\mathbf{n}}$ is the directional derivative ($\nabla_{\mathbf{n}}\varphi = \nabla\varphi \cdot \mathbf{n} = \frac{\partial\varphi}{\partial\mathbf{n}}$).

The monopole solution for V^m can be determined by choosing the function G such that it is a fundamental solution of the Laplace operator,

$$\nabla^2 G(\mathbf{x}, \mathbf{x}_i) = \delta(\mathbf{x} - \mathbf{x}_i) = \delta_{\mathbf{x}_i}\,, \tag{1.12}$$

equation (1.11) simplifies to

$$\int_\tau \left[V^m \delta_{\mathbf{x}_i} - G\nabla^2 V^m\right] \mathrm{d}V = \oint_{\partial\tau} \left[V^m \nabla_{\mathbf{n}} G - G\nabla_{\mathbf{n}} V^m\right] \mathrm{d}S\,, \tag{1.13}$$

$$\int_\tau V^m \delta_{\mathbf{x}_i}\, \mathrm{d}V - \int_\tau G\nabla^2 V^m \,\mathrm{d}V = \oint_{\partial\tau} \left[V^m \nabla_{\mathbf{n}} G - G\nabla_{\mathbf{n}} V^m\right] \mathrm{d}S\,, \tag{1.14}$$

$$\int_\tau V^m \delta_{\mathbf{x}_i}\, \mathrm{d}V = \int_\tau G\nabla^2 V^m \,\mathrm{d}V + \oint_{\partial\tau} \left[V^m \nabla_{\mathbf{n}} G - G\nabla_{\mathbf{n}} V^m\right] \mathrm{d}S\,, \tag{1.15}$$

$$V^m(\mathbf{x}_i) = \int_\tau G\nabla^2 V^m \,\mathrm{d}V + \oint_{\partial\tau} \left[V^m \nabla_{\mathbf{n}} G - G\nabla_{\mathbf{n}} V^m\right] \mathrm{d}S\,, \tag{1.16}$$

which gives an exact potential, measured at $\mathbf{x}_i$, which is the result of a source also located at $\mathbf{x}_i$, and the boundary effects of the system. Applying a Neumann boundary condition sets

$$\nabla_{\mathbf{n}} G = 0\,, \tag{1.17}$$

which can be substituted into (1.16) resulting in

$$V^m(\mathbf{x}_i) = \int_\tau G\nabla^2 V^m \,\mathrm{d}V - \oint_{\partial\tau} G\nabla_{\mathbf{n}} V^m \,\mathrm{d}S\,. \tag{1.18}$$

Substituting (1.10) into (1.18) gives

$$V^m(\mathbf{x}_i) = \int_\tau G\nabla \cdot (\mathbf{u} \times \mathbf{B} - \frac{1}{\sigma}\mathbf{J}^m)\,\mathrm{d}V - \oint_{\partial\tau} G\,(\mathbf{u} \times \mathbf{B} - \frac{1}{\sigma}\mathbf{J}^m) \cdot \mathbf{n}\,\mathrm{d}S\,. \tag{1.19}$$

No current can flow through the insulating surface,

$$\mathbf{J}^m \cdot \mathbf{n} = 0\,, \tag{1.20}$$

and the conservation of charge requires

$$\nabla \cdot \mathbf{J}^m = 0\,, \tag{1.21}$$

thus (1.19) simplifies to

$$V^m(\mathbf{x}_i) = \int_\tau G \nabla \cdot (\mathbf{u} \times \mathbf{B})\,\mathrm{d}V - \oint_{\partial\tau} G\,(\mathbf{u} \times \mathbf{B}) \cdot \mathbf{n}\,\mathrm{d}S\,. \tag{1.22}$$

Integration by parts allows

$$\int_\tau \nabla G \cdot (\mathbf{u} \times \mathbf{B})\,\mathrm{d}V = \oint_{\partial\tau} G\,(\mathbf{u} \times \mathbf{B}) \cdot \mathbf{n}\,\mathrm{d}S - \int_\tau G \nabla \cdot (\mathbf{u} \times \mathbf{B})\,\mathrm{d}V, \tag{1.23}$$

thus (1.22) can be written as

$$V^m(\mathbf{x}_i) = -\int_\tau \nabla G \cdot (\mathbf{u} \times \mathbf{B})\,\mathrm{d}V, \tag{1.24}$$

which is the solution for V^m to a single monopole source at $\mathbf{x}_i$.

The dipole form can be written as

$$V^m(\mathbf{x}_1) - V^m(\mathbf{x}_2) = -\int_\tau \nabla G_1 \cdot (\mathbf{u} \times \mathbf{B})\,\mathrm{d}V + \int_\tau \nabla G_2 \cdot (\mathbf{u} \times \mathbf{B})\,\mathrm{d}V \tag{1.25}$$

where

$$G_1 = G(\mathbf{x}, \mathbf{x}_1) \quad \text{and} \quad G_2 = G(\mathbf{x}, \mathbf{x}_2)\,. \tag{1.26}$$

Combining terms in (1.25) gives

$$V^m(\mathbf{x}_1) - V^m(\mathbf{x}_2) = -\int_\tau \nabla (G_1 - G_2) \cdot (\mathbf{u} \times \mathbf{B})\,\mathrm{d}V \tag{1.27}$$

or

$$V^m(\mathbf{x}_1) - V^m(\mathbf{x}_2) = \int_\tau \mathbf{J}^v \cdot (\mathbf{u} \times \mathbf{B})\,\mathrm{d}V, \tag{1.28}$$

where

$$\mathbf{J}^v = -\nabla (G_1 - G_2) \tag{1.29}$$

is termed the virtual current vector. $\mathbf{J}^v$ represents the current flow as if 1 A were

injected through one electrode and out the other as depicted in Figure 1.7. Note that the units of $\mathbf{J}^v$ are actually m^{-2} and not $\mathrm{A\,m}^{-2}$. Rearranging (1.28) gives

$$V^m(\mathbf{x}_1) - V^m(\mathbf{x}_2) = \int_\tau \mathbf{u} \cdot (\mathbf{B} \times \mathbf{J}^v)\,\mathrm{d}V, \tag{1.30}$$

which can be expressed in terms of Bevir's weight vector,

$$V^m(\mathbf{x}_1) - V^m(\mathbf{x}_2) = \int_\tau \mathbf{u} \cdot \mathbf{W}\,\mathrm{d}V, \tag{1.31}$$

where

$$\mathbf{W} = \mathbf{B} \times \mathbf{J}^v\,. \tag{1.32}$$

This derivation allows the analysis of the flowmeter performance independent of the water flow as it is only defined by the chosen magnetic field and the electrode geometry. $\mathbf{B}$ has an analytical solution in the form of the Biot-Savart law, and $\mathbf{J}^v$ neatly packages the electrode geometry and the boundary conditions imposed by the flowmeter.

The solution for $\mathbf{J}^v$ can be numerically determined by solving for $G = G_1 - G_2$ where

$$\nabla^2 G = -\nabla \cdot \mathbf{J}^v = \delta_{\mathbf{x}_1} - \delta_{\mathbf{x}_2}\,. \tag{1.33}$$

Different electrode geometries can be considered by adjusting the source term in (1.33) with the only constraint being

$$\oint_{S_1} \mathbf{J}^v \cdot \mathbf{n}\,\mathrm{d}S = \int_{E_1} \nabla \cdot \mathbf{J}^v\,\mathrm{d}V = 1\,, \tag{1.34}$$

and

$$\oint_{S_2} \mathbf{J}^v \cdot \mathbf{n}\,\mathrm{d}S = \int_{E_2} \nabla \cdot \mathbf{J}^v\,\mathrm{d}V = -1\,, \tag{1.35}$$

where S_1 and S_2 are the surfaces around the electrodes E_1 and E_2 located at $\mathbf{x}_1$ and $\mathbf{x}_2$.

If the water flow is further defined to be rectilinear and constant along y, $\mathbf{u} = (0, u(x,z), 0)$, then (1.31) becomes

$$\begin{aligned} V^m(\mathbf{x}_1) - V^m(\mathbf{x}_2) &= \int_\tau u(x,z) W_y\,\mathrm{d}V, \\ &= \oint_A u(x,z) \int_{-\infty}^{\infty} \left(B_z J_x^v - B_x J_z^v\right), \mathrm{d}y \quad \mathrm{d}A \\ &= \oint_A u(x,z) W(x,z)\,\mathrm{d}A\,. \end{aligned} \tag{1.36}$$

where

$$W(x,z) \equiv \int_{-\infty}^{\infty} (B_z J_x^v - B_x J_z^v)\,\mathrm{d}y \tag{1.37}$$

is the rectilinear weight function (analogous to Shercliff's weight function) and A is the surface that intersects the flowmeter volume, τ, along the xz-plane.

Figure 1.8 shows a numerical simulation of Shercliff's pipe function using Bevir's weight vector approach. The contours of the weight function clearly follow those of Figure 1.6, although there are some small differences due to the method of simulating the boundary conditions. The heat-map of the weight function clearly indicates the regions of maximum influence around the electrodes themselves which leads to the sensitivity to the flow profile. The weight vector analysis has been used in many places, such as Cha et al. [2002], Cox and Wyatt [1984], Michalski et al. [1998], Watral et al. [2015] where the goal has been to design a flowmeter to accurately measure the overall volumetric flow. The principle can also be used for calibration purposes as demonstrated by Baker [2011]. Yin and Li [2013] has presented an alternative approach for the solution of the weight functions by modelling the problem as a resistor network.

1.6 OCEANOGRAPHY

Oceanographers have built upon the observations of Wollaston [1881] and have attempted to use the Earth's magnetic field in conjunction with undersea telecommunications cables to measure the flowrate through various channels. Experiments performed by Bowden [1956], Bowden and Hughes [1961], Filloux [1973], Hughes [1969] are typical examples of attempts to correlate the measured current through these cables. Longuet-Higgins [1949] performed similar experiments although they made use of electrodes suspended from buoys instead of measuring the voltage across an entire channel. These authors limit their analyses to the correlation of electrical current with measured flow rate and the results are of mixed success. This is due to a variety of reasons; however, predominantly, the different channels the experiments are performed with all have vastly differing geometries. Each channel has a unique flow distribution and virtual current density function. The sensitivity of the various flowmeters is not constant and varies with flowrate, conductivity (salinity), season, and local weather conditions. Robinson and Deacon [1976] used a two dimensional grid to model the weight vector across the Irish Sea. However, ultimately Robinson and Deacon were unable to relate the measured voltage to the volume transport through the sea. They attributed this failure to the spatial deviation of the flow velocity across the channel, particularly around the Isle of Man. The core challenge of designing an oceanographic EMFM is controlling the sensitivity of the flowmeter and its probes to reduce the effects of spatially varying flow speeds. Given the complexity of the flow's velocity distribution and variations in conductivity, this appears to be impractical on such large scales.

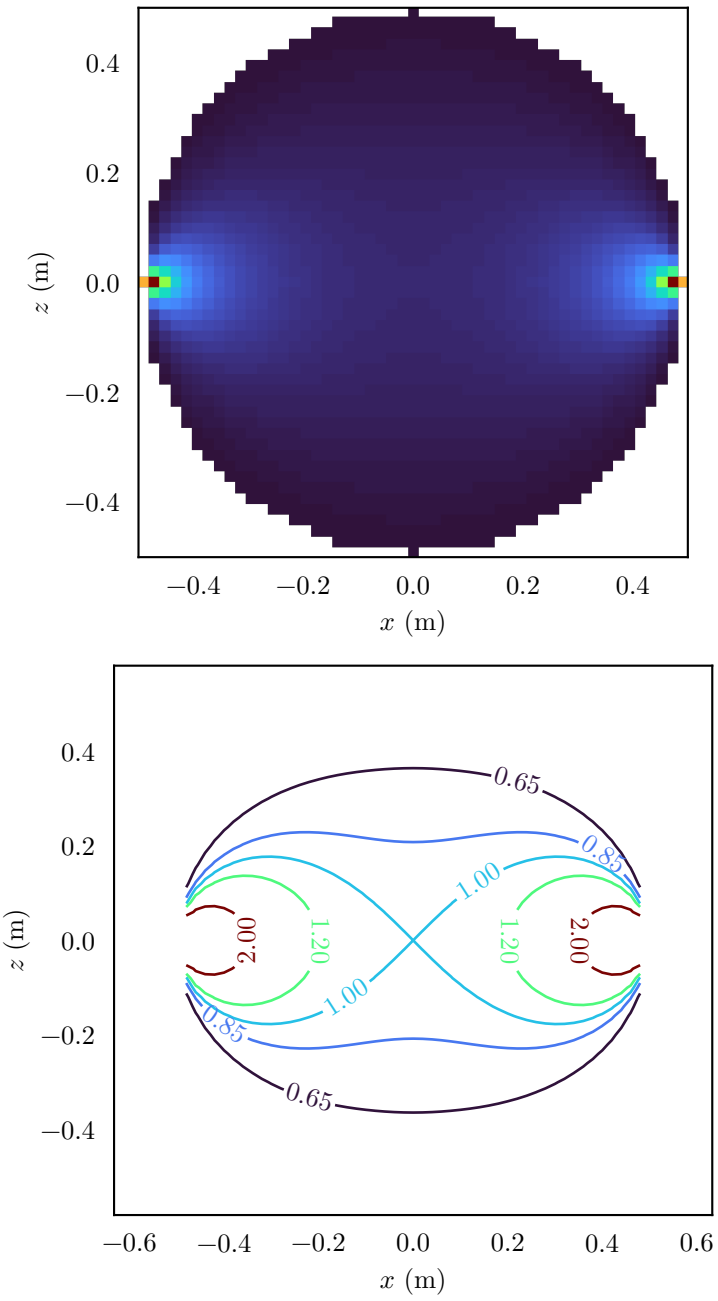

Figure 1.8 A simulated heat-map and contour plot of Bevir's rectilinear weight function from (1.37). The heat-map indicates a strong contribution to the output signal from the area immediately surrounding the electrodes, but little from the rest of the pipe geometry.

Figure 1.9 Photograph of a conventional flowmeter design. An insulating pipe in the bottom allows a fluid to pass through unobstructed. The pipe is surrounded by a Helmholtz coil arrangement to generate a nearly uniform magnetic field. Electrodes in the pipe walls measure the generated electromotive force. The top half of the device contains the power supply and instrumentation electronics used to operate the flowmeter. By ASDFS - Own work, CC BY-SA 3.0, `https://commons.wikimedia.org/w/index.php?curid=29166889`, [Accessed 10/2020]

1.7 MODERN ELECTROMAGNETIC FLOWMETERS

Modern EMFMs are used in a variety of places with a variety of fluids. Many developments have been made over the past century [Alexander 1939, Appel et al. 1976, Cushing 1973, Mannherz et al. 1974, Okaniwa et al. 1995, Sai and Kubota 1999]. Figure 1.9 shows a conventional EMFM design as would be used in an industrial plant to measure the flow of water or other fluid. These devices have found use cases in fields such as medicine, power generation, resource management, and manufacturing. Further research has been performed using the EMFM such as flow velocity tomography [Teshima et al. 1994, 1995]. AC excitation became the norm after Williams's original work [Kolin 1945]. This AC excitation allowed for improved accuracy in measurements. However, it did introduce interference in the form of a transformer signal with amplitude proportional to the excitation frequency [Xu and Wang 2007a, b]. The magnitude of this interference forced the resurgence of the direct current (DC) method in the form of a square wave (or switched DC) excitation [Denison et al. 1955, Jakubowski and Michalski 2005, Mannherz et al. 1974, Spencer and Denison 1959]. The use of the square wave allowed the flowmeter designers to effectively ignore the interference by only measuring the flow signals during the steady state periods.

1.7.1 Blood flow

An interesting alternative use of the EMFM is measuring the flow of blood through an exposed vessel. Denison et al. [1955] started development of an electromagnetic blood flowmeter which could be used to measure the blood flow without damaging the blood vessels. This flowmeter design made use of a square wave excitation and only samples the output signal during the phases of constant magnetic flux. This gated square wave sampling allows for the elimination of most spurious electrode potentials. Further research on the subject by Spencer and Denison [1959] allowed for the zero reference calibration prior to a measurement and the removal of all spurious non-flow signals. The flowmeter designed by Denison and Spencer was also applied by Cordell and Spencer [1959] for measurement of blood flow outside of the body and has been used for animals and humans.

1.7.2 Dielectric and poorly conducting fluids

A typical assumption of the EMFM is that the fluid is of uniform conductivity and supports ionic conduction. Cushing [1965] was able to show that the velocity of a dielectric fluid such as transformer oil could be accurately measured using the electromagnetic technique. His method made use of large plate electrodes completely immersed in the fluid, a 10 kHz sinusoidal excitation, a "hum generator" used to reduce the transformer effect interference, a very large input impedance, and relied upon the induced polarisation currents to operate. Al-Rabeh et al. [1978] further developed the theory set out by Bevir [1970] by solving the weight vector equations for the case of poorly conducting or dielectric fluids providing a more general solution. Amare [1999] proved the results from Al-Rabeh et al. by developing a so called "universal liquid flowmeter" that provided a linear output with flow speed for both dielectric oil and tap water.

Hemp et al. [2002] started research into problems associated with the electromagnetic flowmeter theory when used on dielectric fluids such as BP180 oil. Hemp worked with a series of authors to analyse the effects of the dielectric on the measured signals and interference. Rosales et al. first investigated the noise generated by the flowing water interfering with the diffuse ionic charge layer present near the pipe boundary [Rosales et al. 2002b] and secondly the noise generated by charged particles present in the system [Rosales et al. 2002a]. The result from these papers is a complete analytical model of the noise present in the dielectric flowmeter system. The following year Hemp and Youngs [2003] modelled the zero drift phenomenon with respect to the transformer interference. This provided a framework for estimating and eliminating the zero drift offset introduced by the transformer effect for AC excitation.

1.7.3 Liquid metal circuits

EMFMs as a class of devices possess a combination of properties that make them well suited to measuring the flow in certain harmful environments. One such use case is inside liquid metal cooled nuclear reactors. As the flowmeter does not impede the fluid flow, can remain in situ for long periods of time without maintenance, and can use capacitively coupled electrodes, they make for a simple measurement system for control loops. Tarabad and Baker [1982] has shown that the large induced eddy currents in the liquid metals can cause variations in the calibration of the flowmeter, but this can be corrected through the use of multiple electrodes as well as correcting for variations in conductivity. Rajan and Vijayakumar [2014] investigated the performance of permanent magnet flowmeters (PMFMs) which are used in sodium cooled fast breeder reactor coolant circuits. They found the loss in field strength with respect to time and temperatures to be negligible.

1.7.4 Open channel flowmeter

Open channel EMFMs are an offshoot of the traditional EMFM methodology where the fluid flows through a channel with an open top. In these flowmeters, the water level is also unknown and is required for volumetric flowrate estimation. Typically the level is determined using an alternative sensor like an ultrasonic level meter [Watral et al. 2015].

Use of Bevir's weight vector method, and numerical optimisation algorithms allows Michalski et al. [1998] to numerically evaluate the signal-to-noise ratio (SNR) of an open channel flowmeter [Michalski et al. 1988, 1998]. The magnetic coils were modelled using up to 14 design parameters which were varied and optimised using an iterative evaluation process. Jakubowski applied further signal processing methodologies [Jakubowski and Michalski 2005, 2006, 2008] to Michalski's work to improve the accuracy of the measurements and remove the effects of interference.

Jakubowski and Michalski [2009] added a novel method to also measure the height of the water in the channel by tilting one of the electrodes slightly to intentionally introduce some transformer interference. The amplitude of this interference would be proportional to the filling height and could be calibrated to account for a linear gain factor.

1.7.5 Borehole flowmeter

A relatively recent innovation of the EMFM is its use as a borehole flowmeter. In this case, the flowmeter is designed as a tall, narrow cylinder that can be lowered down existing boreholes to measure the vertical water velocity component [Molz et al. 1994, Molz and Young 1993]. A complication for this method is the requirement of post

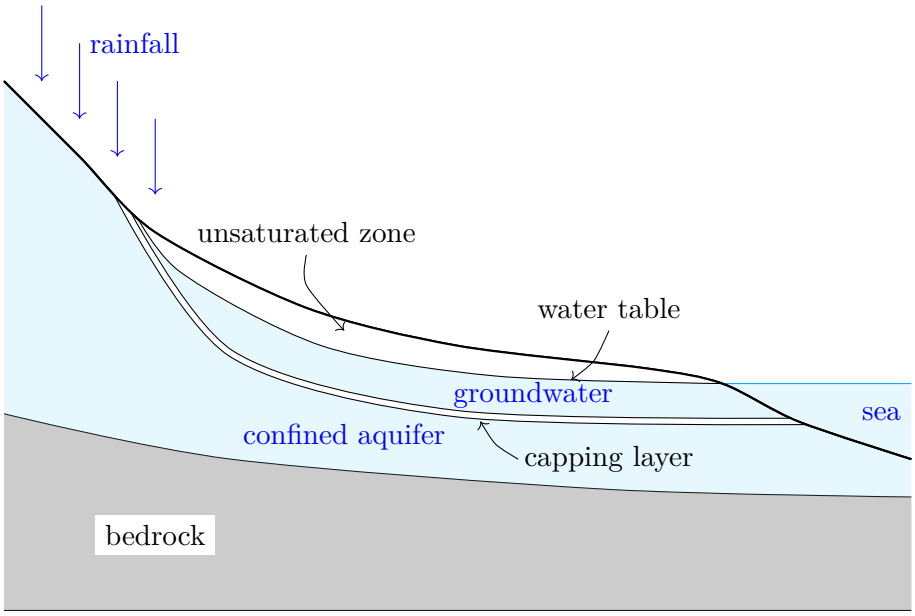

Figure 1.10 A diagram showing three different types of water. Here the rainfall acts as a source of water that flows down into the earth. Some of the water will travel down the slope and eventually become part of the groundwater, just beneath the soil. Some of the rest of the water will drain directly down into the aquifer, which is trapped below the capping layer. This capping layer is a layer of rock or clay, that restricts the water flow between the aquifer and the groundwater. Alluvial wells are drilled down through the capping layer to access the source of clean drinking water in the aquifer. Often the alluvial water is under enough pressure to generate a positive head such that the water flows out of the well without external pumping.

processing the measurements with as many as five different corrections [Paillet 2004]. These borehole flowmeters primary use case is analysing the composition of underground strata by recording the various physical properties.

1.7.6 Zero drift phenomenon

A common problem with EMFMs designs is the zero drift phenomenon [Saito et al. 1994, Wantzelius and Goetz 1977]. This has been a recurring problem that is not yet fully understood. Attempts to correct for the drift have been made by Hemp and Youngs [2003], Michalski et al. [2013], and Linnert et al. [2018]. These authors typically attempt to solve the problem through adaptive modelling of the measured signal such that the zero point is automatically adjusted to compensate for the drift. This phenomenon reduces the effectiveness of the flowmeter, particularly in industrial applications where the flowmeter must be regularly recalibrated to maintain accuracy. There remains a lack of understanding of the mechanism behind the drift despite the work performed by Hemp and Youngs.

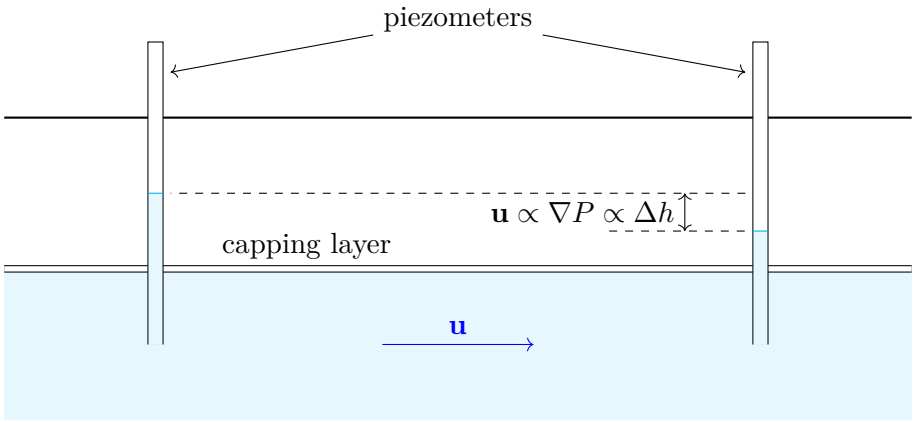

Figure 1.11 Diagram showing the method of operation for flow measurement using piezometers. The piezometer tubes allow the flowing water to escape up the tube, with a height proportional to the static pressure at the bottom of the tube. The pressure difference between two tubes is thus proportional to the pressure difference over the separation of the wells and thus the pressure gradient. When the hydraulic properties of the aquifer medium are known, then the flow velocity can be derived.

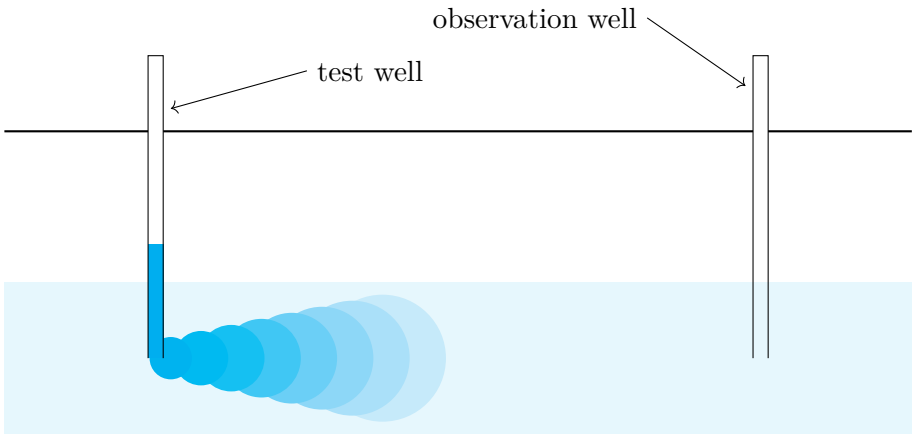

Figure 1.12 Diagram of a simple slug test measurement. There are a variety of slug methods, but the common principle is to inject a traceable material or fluid, and inject it into the flow stream. Measurements can then be made from the observation well to detect the passage of the tracer and determine the velocity. Various tracers can be used such as salts to change the conductivity, dyes to change the colour, or radioactive isotopes.

1.8 GROUNDWATER MEASUREMENT

Groundwater, as one of the sources of clean drinking water, is an important resource and as such needs to be monitored [Igor 1993]. It is distinct from other water sources such as aquifers or surface water, and is defined as the water saturating the soil just below the surface. Figure 1.10 shows the difference between groundwater and an aquifer. Typical groundwater measurement techniques involve measuring the head pressure in wells over an area such as a city or countryside, as shown in Figure 1.11, or performing slug tests over distances of hundreds of metres as in Figure 1.12. The slug tests operate by inserting a 'slug' of traceable mineral or dye into the flow stream and measuring its displacement over time [Bouwer and Rice 1976].

1.8.1 Darcy's law

Darcy's law describes the inviscid flow of a fluid through a medium, originally formulated experimentally by Henry Darcy in 1855 and 1856 for water flowing through sand. Whitaker [1986] has since theoretically derived the law. Darcy's law as refined by Muskat [1937] states

$$q = -\frac{k}{\mu}\nabla p\,, \tag{1.38}$$

where q is the instantaneous flux ($\mathrm{m\,s^{-1}}$), k is the permeability of the medium ($\mathrm{m^2}$), μ is the dynamic viscosity ($\mathrm{Pa\,s}$), and ∇p is the pressure drop over a distance ($\mathrm{Pa\,m^{-1}}$). The fluid velocity is related to the flux by

$$u = \frac{q}{\varphi} \tag{1.39}$$

where φ is the medium porosity (unitless). In other words, the smaller the volume of the voids in the medium, the faster the fluid particles move to give a constant flux. Figure 1.13 shows two different soil granularities with differing porosities to illustrate this concept. For a groundwater flow, $10\,\mathrm{mm\,h^{-1}}$ ($2.78\,\mathrm{\mu m\,s^{-1}}$) is considered to be a fast flow [Alley et al. 1999].

1.9 SUMMARY

EMFMs have been in use, in one form or another, for almost two centuries now. During that time the core operating principle, pioneered by Michael Faraday, has not changed at all. In the early years this technology remained solely the realm of oceanographers attempting to map the many ocean channels around the world using undersea communications cables. The work performed by Williams in 1930, however,

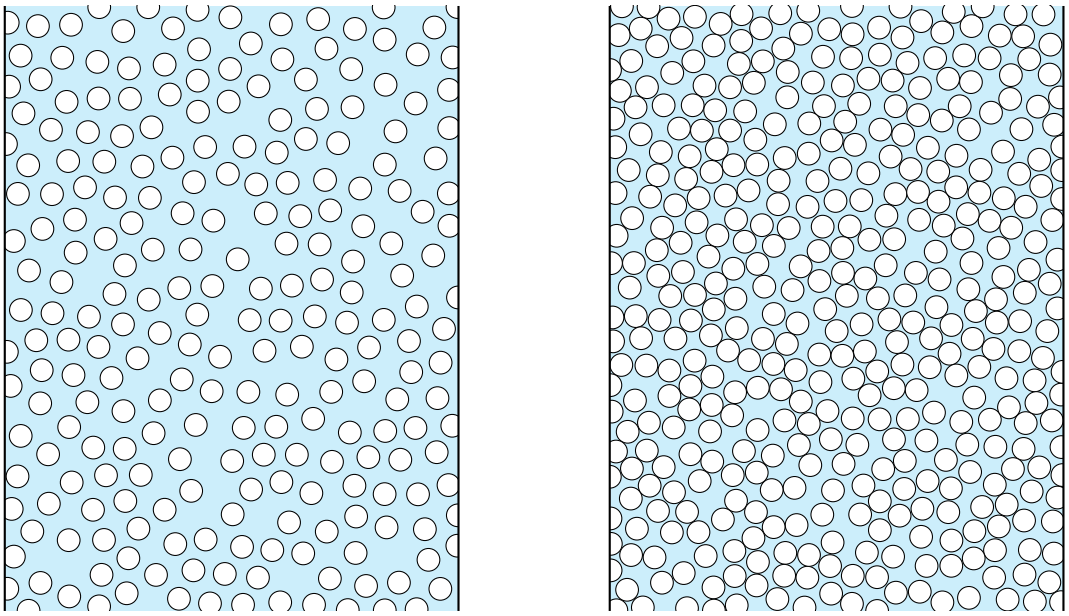

Figure 1.13 An example showing how much available surface area the fluid can flow through. In this example the blue fluid is flowing into the page with a constant volumetric flowrate. The white circles represent the grains of solid matter that the fluid cannot flow through. The left panel has a porosity of 60% and the right has a porosity of 35%. Because there is less available area in the right panel, the water has to flow faster to deliver the same discharge.

suddenly made the EMFM an appealing device to various industries due to its non-invasive measurement technique. The flowmeter found uses in many new fields such as medicine as a blood flowmeter, or as part of a feedback system in a liquid metal nuclear power plant control loop. Further research by Shercliff and subsequently Bevir have firmly established the fundamental theories of operation for the EMFM with all modern techniques making use of Bevir's weight vector analysis. Researchers such as Jakubowski and Michalski have adapted the technique for open channel flow measurement for use in rivers or canals. However, there have been no attempts to apply the EMFM method to the measurement of groundwater flows. This is likely due to the incredibly slow velocities present.

Chapter 2

GROUNDWATER FLOWMETER

The goal of this thesis is to use the methods and technology of the EMFM technique described in Chapter 1 and demonstrate a method to estimate the velocity of near surface groundwater flows such as those shown in Figure 2.1. The ideal solution should not require much manual work such as digging large holes in which to place the flowmeter. The result of these requirements leads to a design depicted in Figure 2.2. The problem can be broken down into four categories: coil and magnetic field design, electrode geometry, instrumentation, and signal processing.

2.1 COIL DESIGN

The primary goal of this flowmeter is to measure the groundwater velocity. The groundwater table is not constant so the ideal flowmeter will be able to average over a large volume. The pancake coil, shown in Figure 2.3, is made from nine individual pancake coils, connected as shown in Figure 2.4, each of which comprises 27 turns of 6 mm $\times$ 3 mm copper bar giving the coil a total mass of 175 kg. The coil has a free-space inductance of 8.4 mH and a DC resistance of 68 mΩ. However, at higher frequencies the impedance of the coil becomes more complicated due to the proximity effect. The coil is modelled as a 1 m $\times$ 1 m square made from four separate conductors, as shown in Figure 2.5. The resultant field, with 50 A of excitation current, is shown in Figure 2.6 with a flux density of approximately 0.5 mT one metre above and below the coil. The coil was designed and constructed by the Robinson Research Institute at the Victoria University of Wellington in New Zealand.

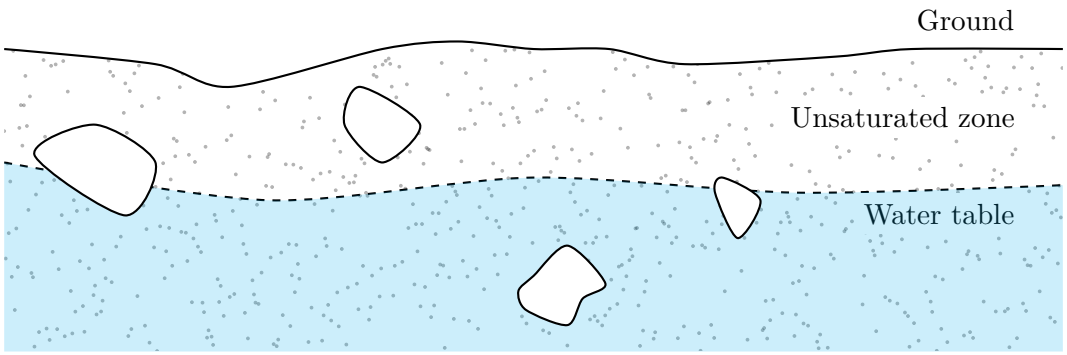

Figure 2.1 An example diagram of groundwater conditions under the soil. The depth of the water table varies from point to point. The presence of unknown obstacles such as the rocks pictured is also likely.

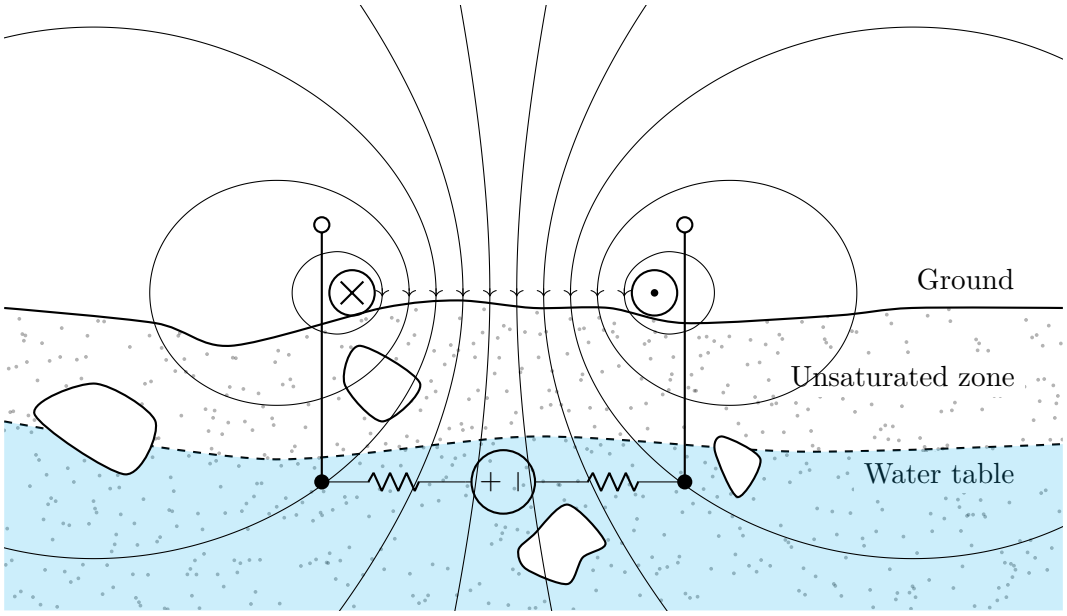

Figure 2.2 Simplified diagram of the groundwater flowmeter concept. A large coil is placed on the surface of the ground and an electrical current is passed through it. This generates a magnetic field which penetrates down to the water table. Two electrodes are inserted into the water table layer. In this example the water is moving into the page resulting in an electric potential being generated between the two electrodes. Instrumentation equipment can be connected to measure potential and estimate the water velocity.

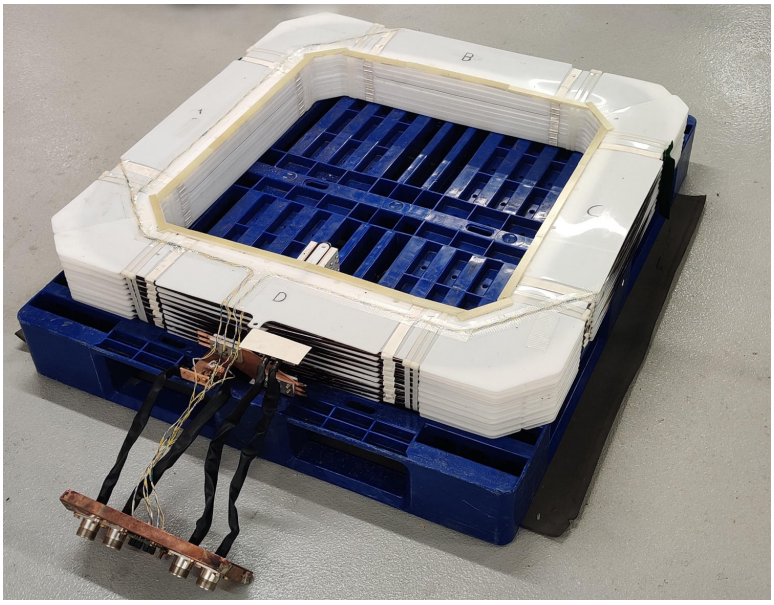

Figure 2.3 Photo of the pancake coil used in laboratory and field experiments sitting upon a blue plastic pallet. The nine pancake layers are connected in three groups of three parallel coils. The thin wires connect a series of thermocouple temperature sensors to the front plate of the coil.

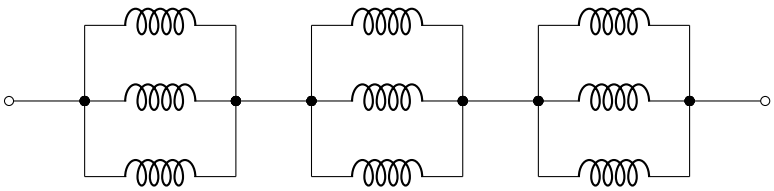

Figure 2.4 Diagram of the internal connections inside the excitation coil. It is constructed from nine individual pancake coils which are connected in three series groups of three parallel coils.

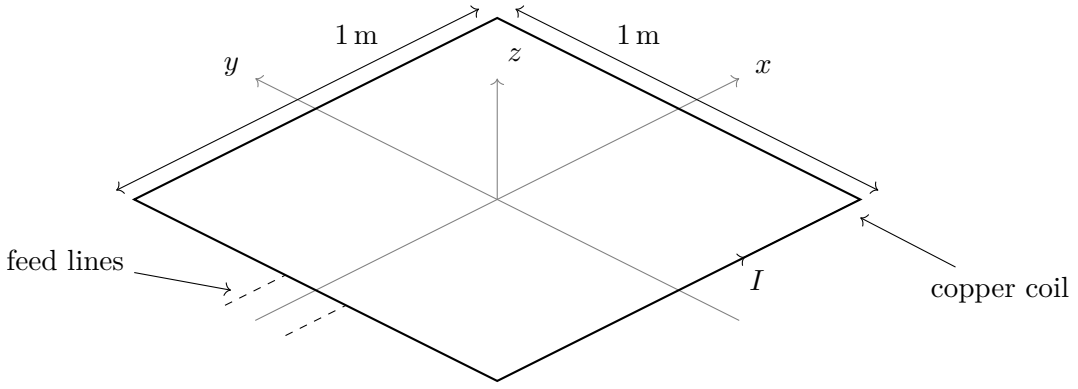

Figure 2.5 Diagram of the pancake coil geometry as simulated. The coil consists of four, one metre sections arranged in a square. The feed lines contribute negligible magnetic field and are omitted from the simulation.

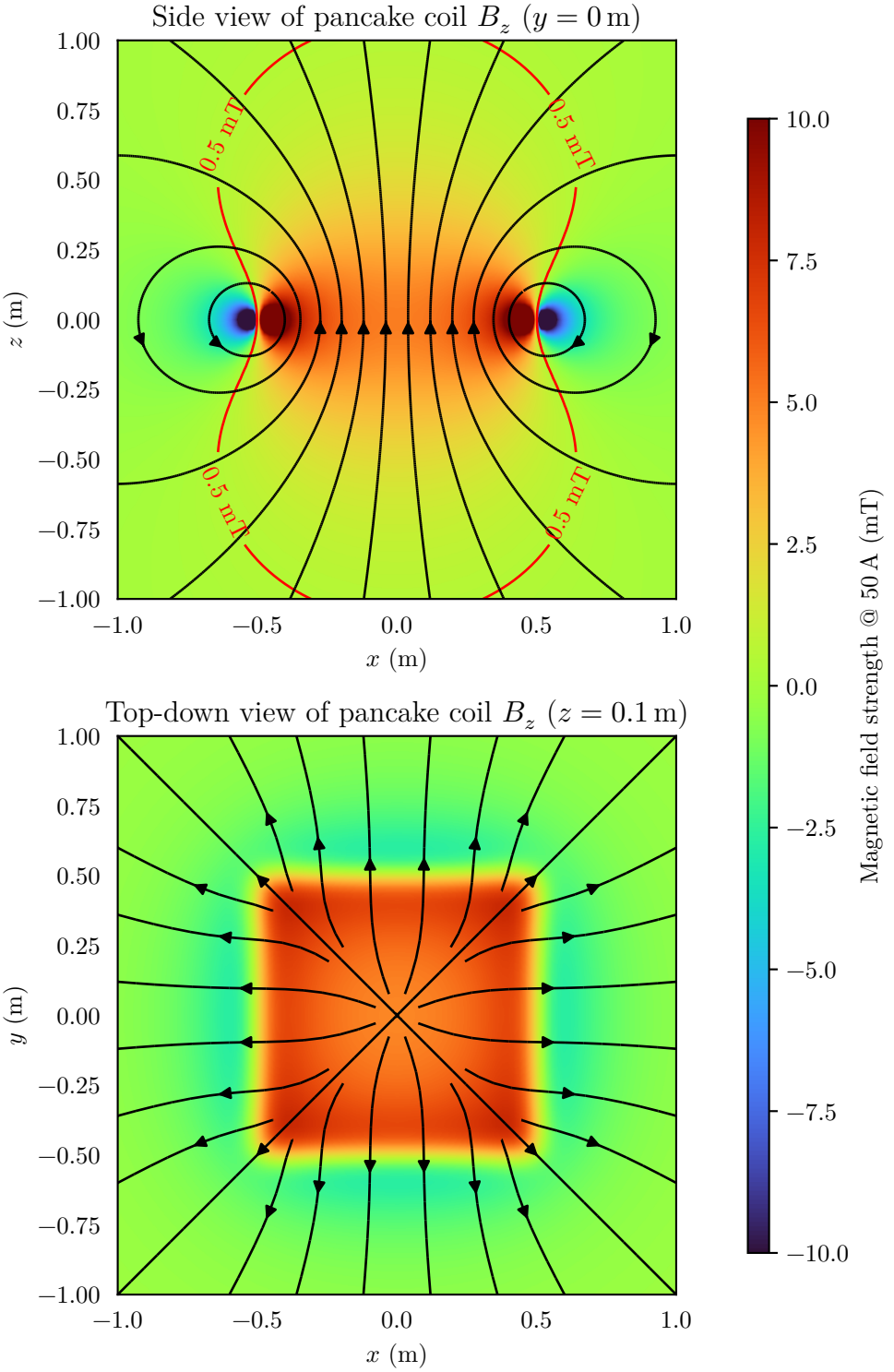

Figure 2.6 Plot of the vertical magnetic field component, B_z, around the pancake coils. The field is viewed from the side of the coil and from above the coil, respectively. The field lines indicate flow of the magnetic field. The red contour shows where the field has a field strength of 0.5 mT.

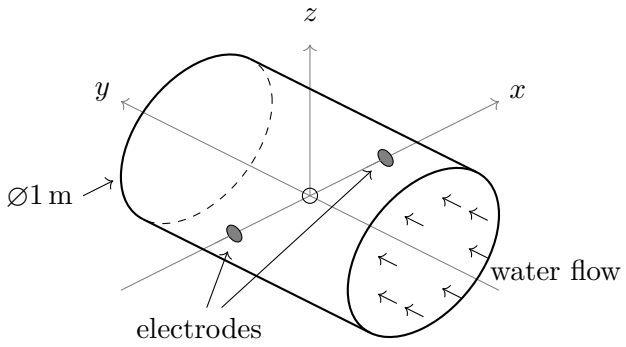

Figure 2.7 Layout of the traditional pipe flowmeter geometry for modelling. The laminar water flow occurs down the y-axis of the pipe. A magnetic field is applied in the z-axis and two electrodes are located in the walls of the pipe along the x-axis.

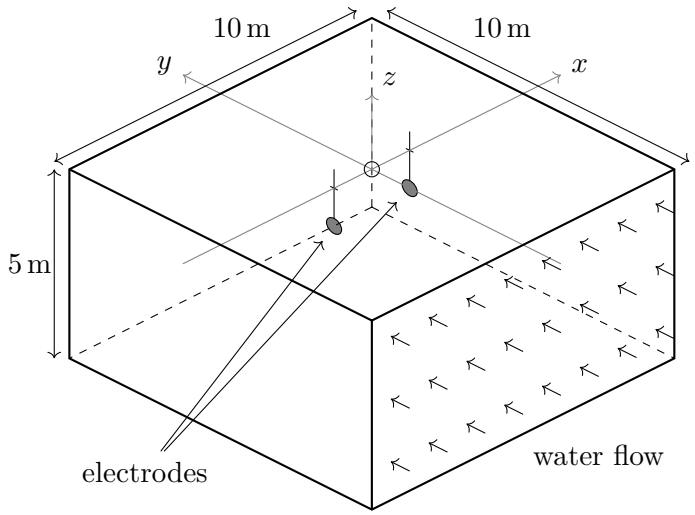

Figure 2.8 Layout of the field flowmeter geometry. The Earth is modelled as a large volume of uniform conductivity to reduce the effect of the boundaries on the output signal. The electrodes and the excitation coil are located around the origin, located in the centre of the top face of the volume.

2.2 MODELLING GEOMETRIES

Flowmeter modelling is done over three different geometries representing different physical flowmeters. Figure 2.7 shows the traditional pipe flowmeter geometry which is used to validate answers against theoretical models. Figure 2.8 shows an approximation of a groundwater flowmeter context. In a real-world field measurement scenario, the edge effects generated by the boundary conditions occur at a greater distance (>5 m) and have much less impact than in a traditional pipe (<1 m radius). The geometry in Figure 2.8 attempts to mimic this by moving the boundaries further away from the measurement. Finally Figures 2.9 and 2.10 show the geometries of the laboratory equipment that is used to validate the simulations and signal processing methods experimentally.

The choice of electrode shape directly influences the virtual current density, $\mathbf{J}^v$.

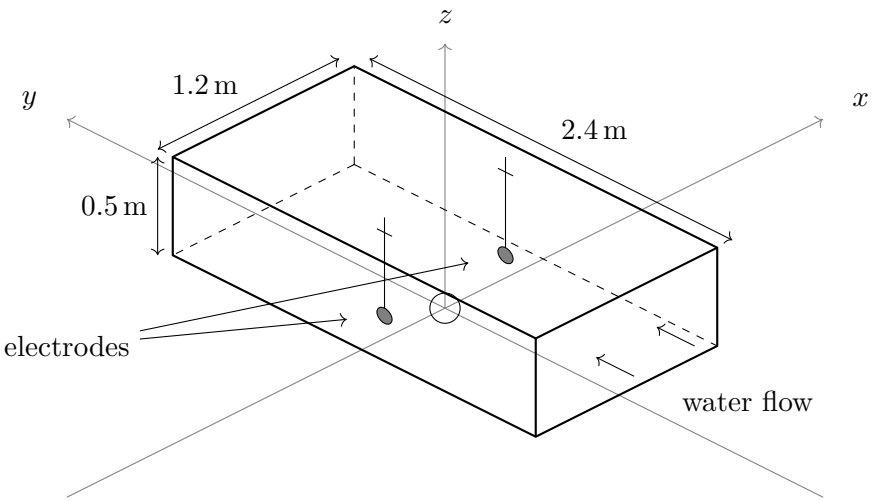

Figure 2.9 Layout of the laboratory tank flowmeter geometry. In this geometry the excitation coil is located 0.1 m below the tank.

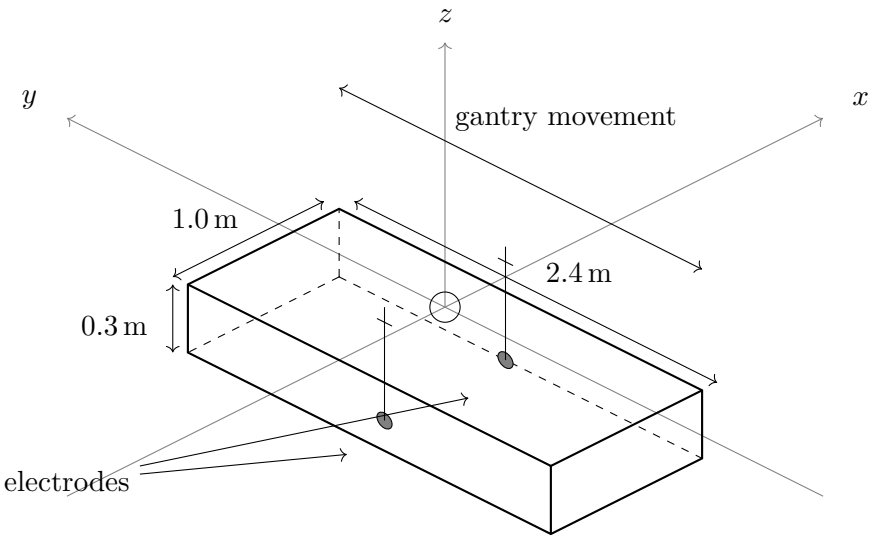

Figure 2.10 Layout of the laboratory gantry flowmeter geometry. In this geometry the excitation coil is located on rollers above the geometry and moves from one end to the other at $0.6\,\mathrm{mm\,s^{-1}}$.

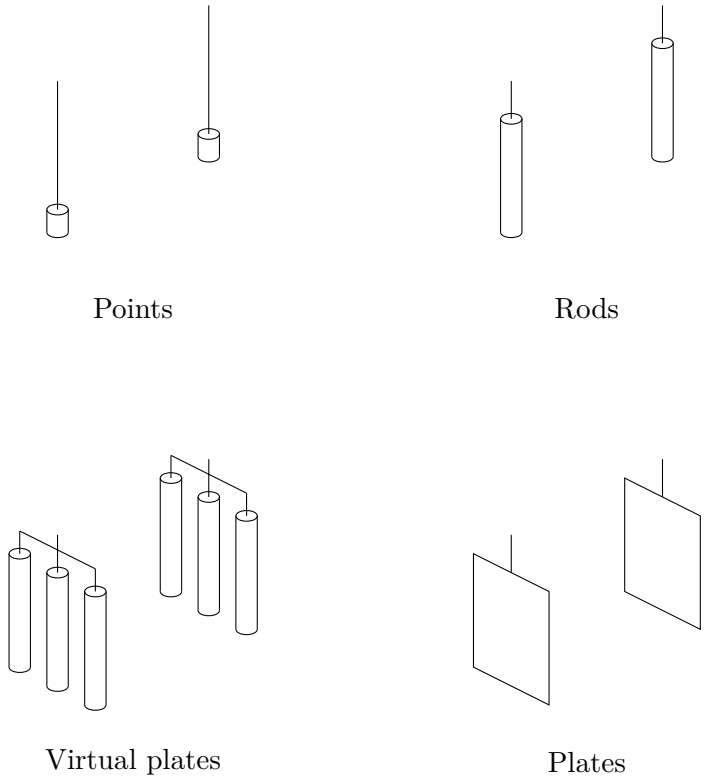

Figure 2.11 Diagram of the different electrode geometries for modelling. Point electrodes represent the typical analytical case, whereas plates provide the flattest virtual current densities. Virtual plates are constructed from a row of rods that are electrically connected. This geometry is easier to insert into the ground than actual plates and may result in similar performance.

Four geometries, shown in Figure 2.11, are simulated to determine relative sensitivities to velocity flows.

2.3 SIMULATIONS

Simulations of the geometries and magnetic field are built using iterative methods as described in Appendix A. These are used to determine which electrodes perform the best, what electrode spacing should be used, and how the different magnetic field affects these results. An example of the simulations is shown in Figure 2.12 where the simulation recreates Shercliff's weight function result from Chapter 1.

2.3.1 Electrode comparison

The weight vector is defined, in part, by the geometry of the electrodes and the boundary conditions imposed by the environment. Figure 2.13 shows plan views of the weight vector's y component, overlaid with the field lines of the virtual current vector. The ideal virtual current vector is a 'flat' uniform field, such that the current density is uniform. These figures illustrate how the plate and virtual plate electrodes have the

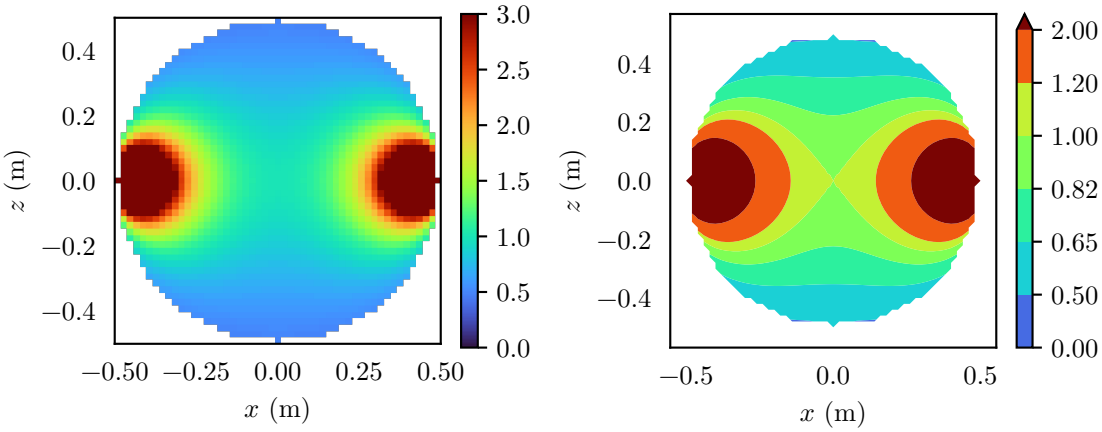

Figure 2.12 Plot of the weight vectors y-component, $W_y(x, 0, z)$ for a simulation of the typical pipe flowmeter as modelled by Shercliff. Note that this is a slice across the pipe and not an integral down the length of the flowmeter. The point electrodes are located at $(\pm 0.5, 0, 0)$ and a transverse magnetic field is applied along the z-axis. This simulation matches the results calculated by Shercliff shown in Figure 1.6.

virtual current spread across a larger surface area. This avoids strong concentrations of weighting immediately around the electrodes such as the point and rod electrodes. Figure 2.14 shows a comparison of the weight vector uniformity for the four electrode types. The measurements are made in a line across the tank, through the centre of each pair of electrodes located at $x = \pm 0.4\,\mathrm{m}$. The figure shows that the volume surrounding the point electrodes has a strong influence on the results compared to the region halfway between them. Compare this with the even weighting distribution for the plate electrodes. Note that a completely flat weight distribution would lead to a linear cumulative sum. These simulations show that the plate electrode has the best performance with regard to an even distribution of weighting, but also that the virtual plate and rod electrodes have a similar performance when considering the rectilinear weight function.

2.3.2 Tank simulations

Figure 2.15 shows the rectilinear weight functions of the four electrode arrangements with the pancake coil in the experiment tank. The sensitivity, S, is calculated as

$$S = \frac{V_1 - V_2}{u_y I} = \frac{\int_V W_y \,\mathrm{d}V}{u_y I}\,, \tag{2.1}$$

where I is the excitation current, and u_y is the rectilinear flow speed in the y, direction which must be slow enough for inviscid flow. Notably all four electrode pairs exhibit similar sensitivity of $\approx 30\,\mu\mathrm{V\,s\,A^{-1}\,m^{-1}}$ for the tank geometry. This is due to the fact that over the volume of non-negligible virtual current densities, the magnetic field is

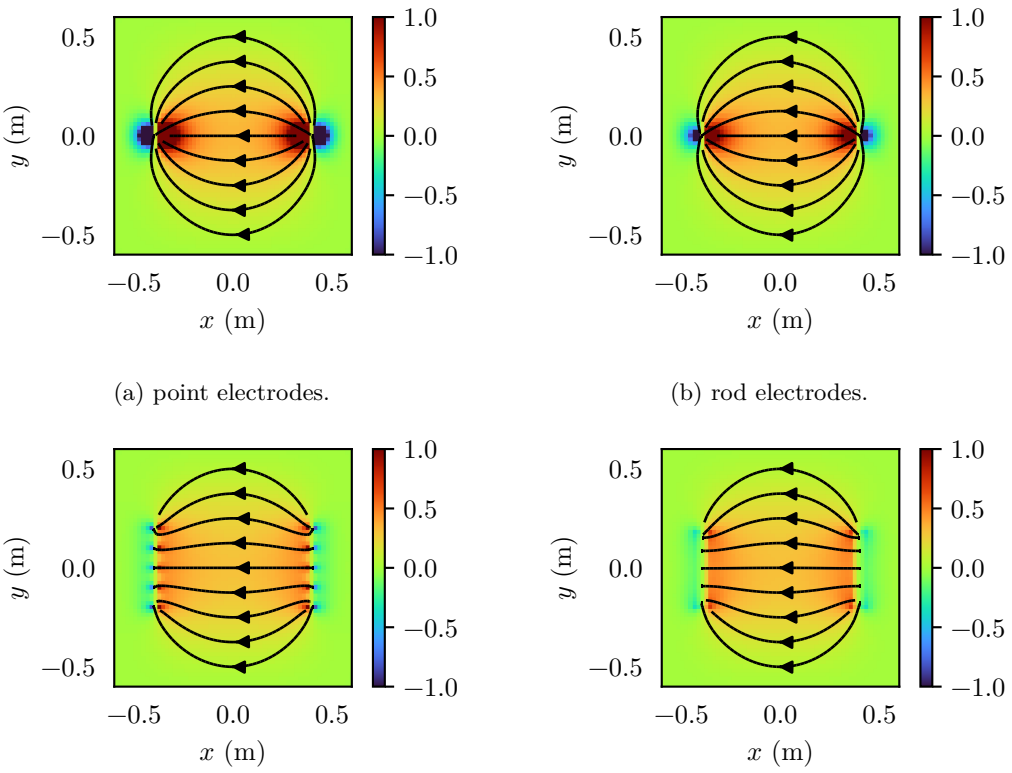

(a) point electrodes.

(b) rod electrodes.

(c) virtual plate electrodes.

(d) plate electrodes.

Figure 2.13 A top-down plot of the y-component of the weight vector, $W_y(x, y, 0.3)$, for the different electrodes, located at $z = 0.3\,\mathrm{m}$, with the pancake coil at $z = 0\,\mathrm{m}$. The field lines indicated the virtual current flow between the electrodes. Note the strong weighting immediately around the point and rod electrodes compared with the plate and virtual plate electrodes.

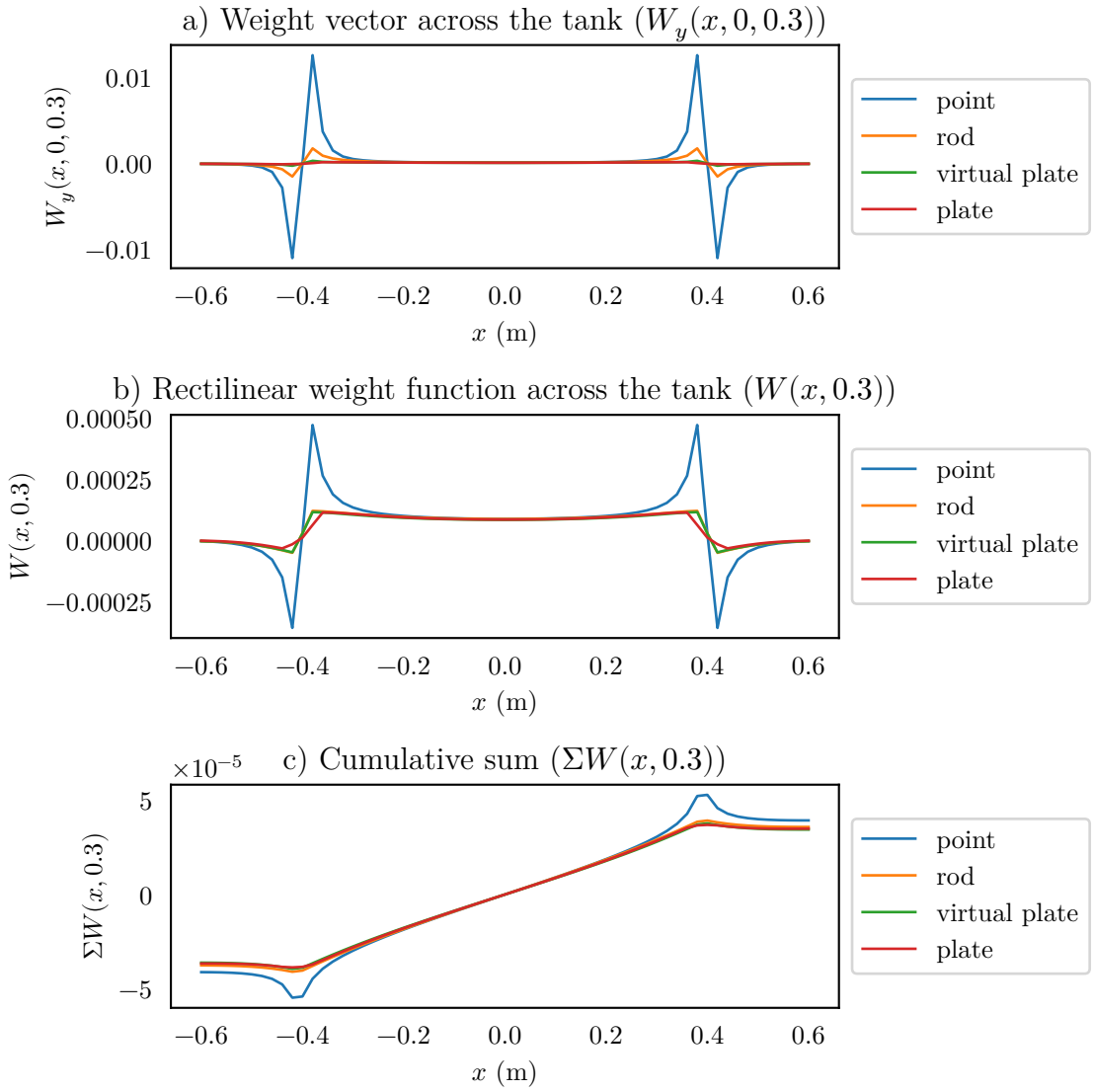

Figure 2.14 Comparison of the sensitivity of the different electrodes across the width of the experiment tank. The top plot shows the sensitivities at each point. The middle plot shows the rectilinear weight function, which is the sum of all of the weights along the length of the measurement tank. The bottom plot shows the cumulative sum of the rectilinear weight function across the tank. Ideally the weighting would be equal across the width of the tank which would also be shown as a linear cumulative sum.

consistent. Taken to the extreme, this can be represented by a constant magnetic field over the geometry in which case, (1.32) becomes

$$\mathbf{W}(\mathbf{x}) = \mathbf{B} \times \mathbf{J}^v(\mathbf{x}) \,, \tag{2.2}$$

where $\mathbf{B} = (0, 0, B)$ is the average (vertically aligned) magnetic field over the measurement volume. When also considering a rectilinear flow, u_y, (1.31) becomes

$$V^m(\mathbf{x}_1) - V^m(\mathbf{x}_2) = u_y \int_\tau (\mathbf{B} \times \mathbf{J}^v)_y \, \mathrm{d}V, \tag{2.3}$$

$$= u_y \int_\tau B J_x^v \, \mathrm{d}V, \tag{2.4}$$

$$= u_y B \int_\tau J_x^v \, \mathrm{d}V. \tag{2.5}$$

The implication of this result is that, in scenarios where the magnetic field is consistent over the volume between the electrodes, they will result in approximately the same *overall* sensitivity to flow speeds, unless the two electrode geometries are *radically* different. The only difference between the electrode pairs is the spatial weightings throughout the measurement volume. The plate, virtual plate, and rod electrodes, as stated in Section 2.3.1, have a more even distribution throughout the volume than the point electrodes. All three of these electrode types could be used to measure the same flow speed through the electrodes, but the plate and virtual plate electrodes are sensitive to a larger volume than the simple rod electrodes allowing a more accurate estimate when spatial variations in flow speed are present.

2.3.3 Gantry simulations

The gantry geometry simulation shown in Figure 2.16 shows similar results to the tank simulations. Due to even smaller measurement space than in the tank geometries, the sensitivities are again consistent around $\approx 25\,\mu\mathrm{V\,s\,A^{-1}\,m^{-1}}$.

2.3.4 Field simulations

Figure 2.17 show the results of simulating the plate electrode type in the field geometry with the pancake coil. The results follow those of Sections 2.3.2 and 2.3.3 with the exception of the sensitivity which drops from $25\,\mu\mathrm{V\,s\,A^{-1}\,m^{-1}}$ to $30\,\mu\mathrm{V\,s\,A^{-1}\,m^{-1}}$ down to $\approx 21.5\,\mu\mathrm{V\,s\,A^{-1}\,m^{-1}}$.

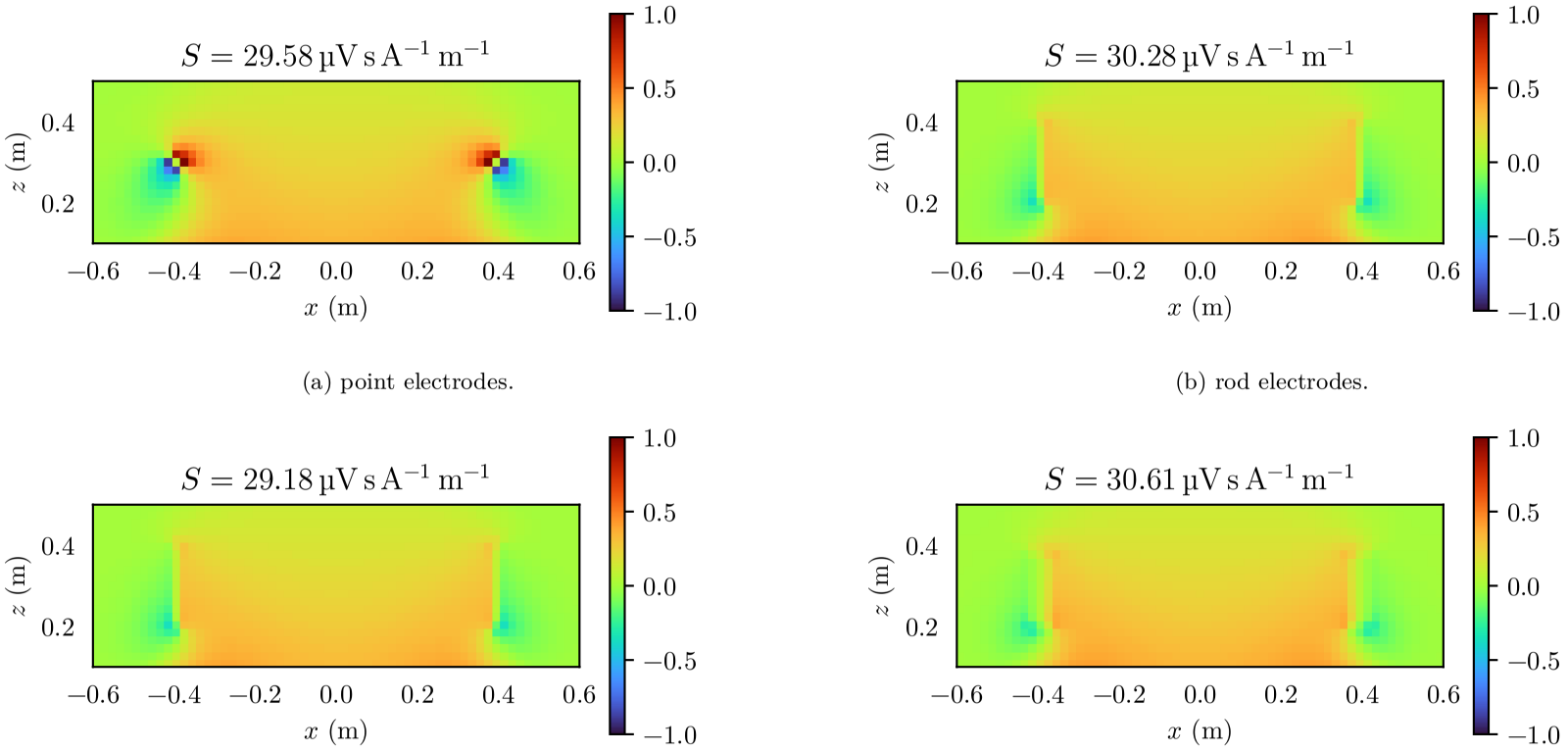

(a) point electrodes.

(b) rod electrodes.

(c) virtual plate electrodes.

(d) plate electrodes.

Figure 2.15 Rectilinear weight functions, $W(x, z)$, for electrodes in the experiment tank with a pancake coil for excitation. Note the strong positive and negative influence around the electrodes at $(\pm 0.4, 0, 0.3)$. The excitation coil is located beneath the tank leading to a stronger weighting to the lower half of the volume.

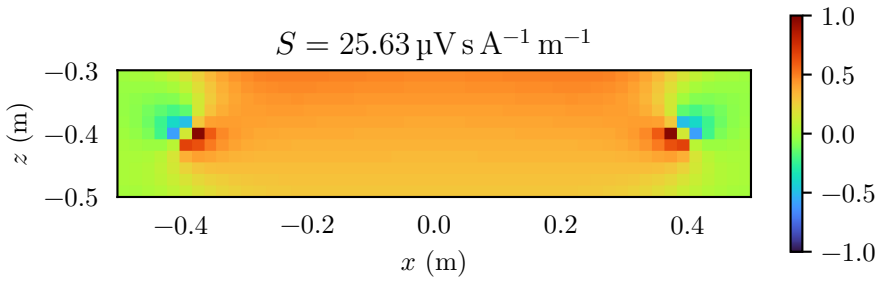

(a) point electrodes.

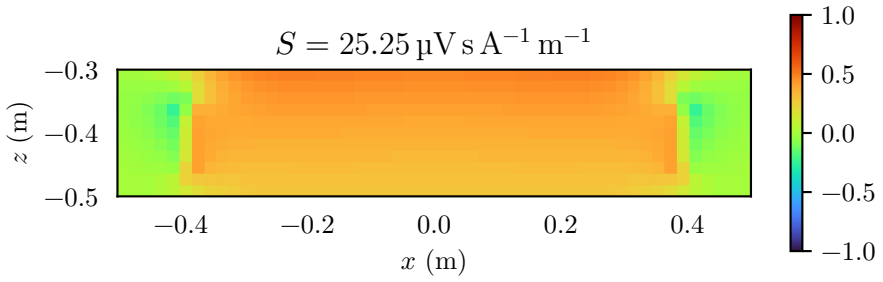

(b) rod electrodes.

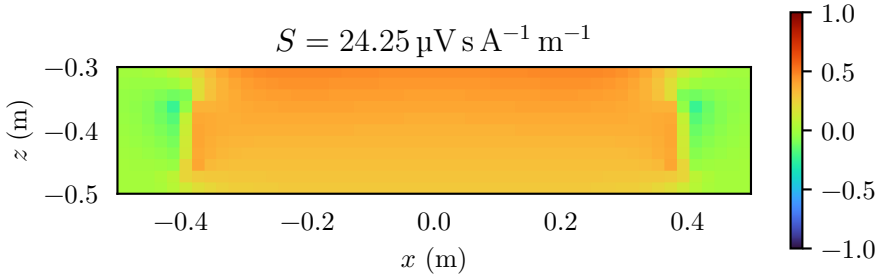

(c) virtual plate electrodes.

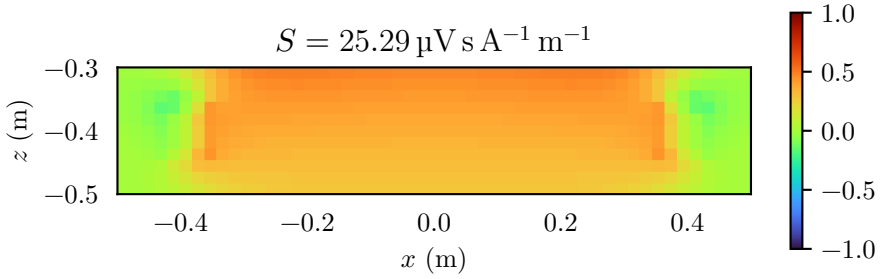

(d) plate electrodes.

Figure 2.16 Rectilinear weight functions for the electrodes in the gantry geometry. In this geometry the coil is located above the pool of water.

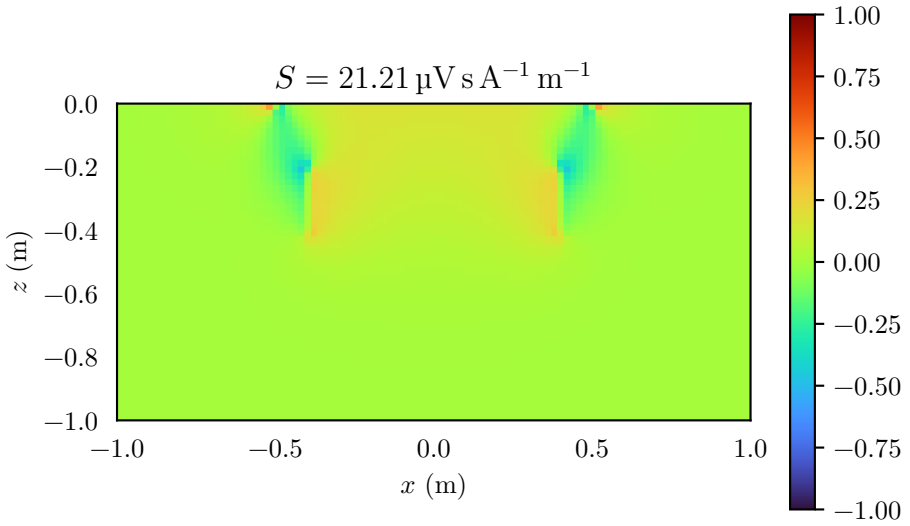

Figure 2.17 Rectilinear weight function for virtual plate electrodes in the field geometry with a pancake coil for excitation.

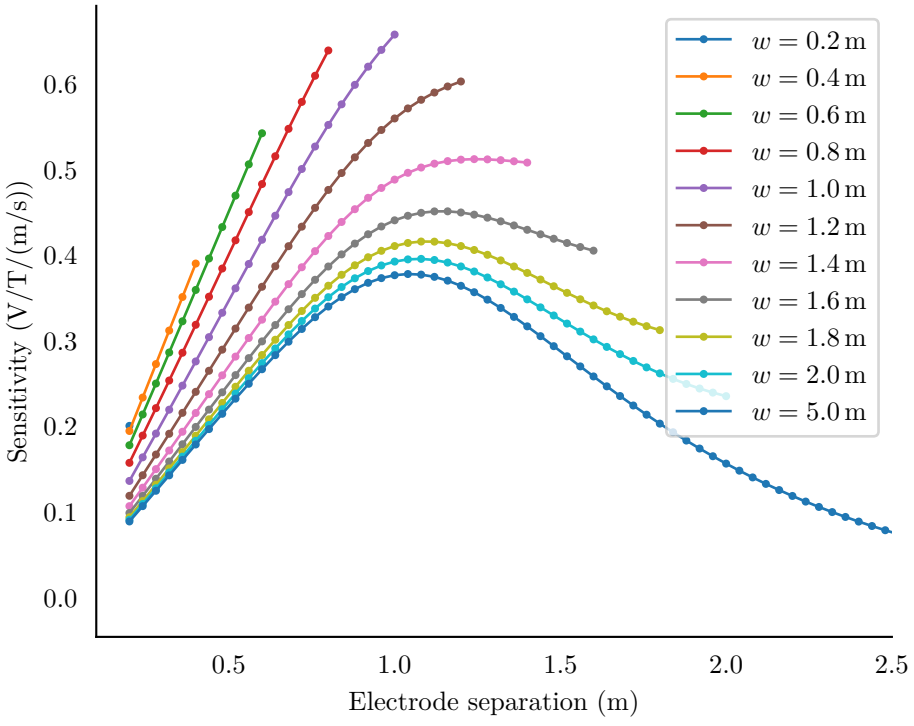

Figure 2.18 Comparison of different sensitivities for varying electrode separation and geometry widths. The simulation volume spans $w \times 2.4\,\mathrm{m} \times 1\,\mathrm{m}$ where each series is a different width. The electrode separation is varied from 0.4 m up to the tank width, w. Notably the maximum sensitivity occurs when the flowmeter width, electrode separation, and excitation coil width are all the same, at 1 m in this figure. The sensitivity is almost linear for the flowmeter experiments that are narrower than, or equal to, the excitation coil width (1 m).

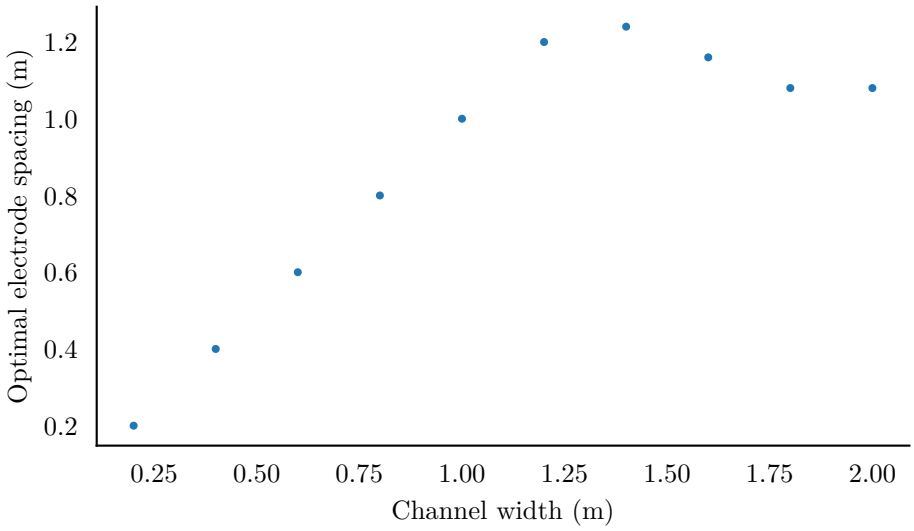

Figure 2.19 Plot of the optimal electrode separations for different channel widths. For the smaller geometries (<1 m) the optimal separation is the same as the width of the channel. For larger geometries the optimal separation is slightly larger than the width of the excitation coil (1 m).

2.4 OPTIMAL ELECTRODE SEPARATION

One remaining question is how the sensitivity changes with respect to electrode separation. Figure 2.18 shows a simulation using the tank geometry and point electrodes. The tank width and electrode separation are varied and the sensitivities determined. The largest sensitivity occurs when the electrode separation and tank width equal the coil size of 1 m. Figure 2.19 shows the optimal electrode separation for a given channel width. This shows that for smaller geometries, the widest electrodes give the strongest signal but for geometries larger than the coil, placing the electrodes at the outer edge of the coil gives the strongest signal.

For the geometries where the separation and the tank width are smaller than the coil (<1 m), the sensitivity is approximately proportional to the separation distance. This agrees with the empirical flowmeter equation, (1.7), and applies to the majority of industrial flowmeter designs. However, tank widths larger than the coil show the empirical equation does not apply as the electrode separation approaches and passes the coil width. The maximum sensitivity asymptotically decreases as the separation is increased. A side note regarding the larger geometries is as the electrode separation surpasses the width of the coil, the approximation in (2.5) no longer applies and choice of electrode geometries may have a larger impact on the sensitivities.

Comparing the measured sensitivities with the empirical flowmeter equation, (1.7), allows for the estimation of the k parameter for a given geometry. Equating (1.7) with

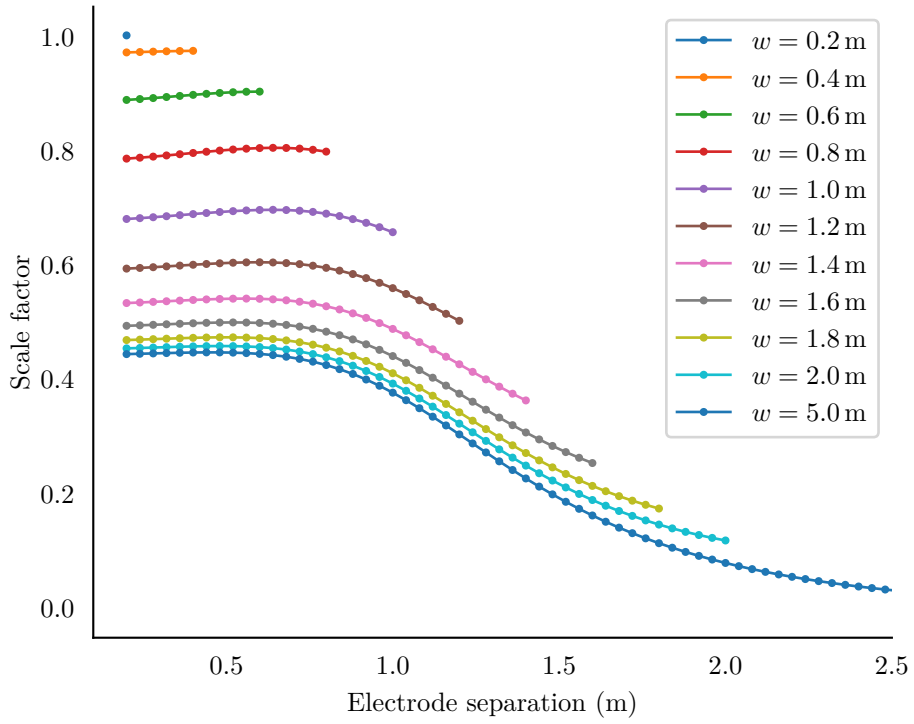

Figure 2.20 Estimation of the scale factor, k, for the empirical flowmeter model for various geometries. The estimated k value is constant for separations $<0.7\,\mathrm{m}$ showing it is a good estimate. For larger geometries, the varying k factor indicates the empirical model is a poor choice.

(2.1), where $V = V_1 - V_2$, gives

$$kBu_yD = V = Su_yI\,, \tag{2.6}$$

$$k = \frac{Su_yI}{Bu_yD}\,, \tag{2.7}$$

$$= \frac{S}{D}\frac{I}{B}\,. \tag{2.8}$$

Given that the empirical flowmeter equation only applies for smaller geometries in which the magnetic field is almost constant, B represents the average transverse magnetic flux and can be determined through a field sensor or taken from a model of the excitation coil. The I/B ratio is the inverse of the flux generating capacity of the excitation coil and is a constant factor. Figure 2.20 shows the estimation of the k scale factor for the same range of geometries. For any electrode separation less than $0.7\,\mathrm{m}$ the scale factor remains constant and is determined only by the separation of the boundaries. For larger separations the estimate for k from (2.8) no longer applies as the magnetic field is no longer consistent over the measurement volume.

2.5 SUMMARY

The results of the simulations show that:

1. A voltage should be measurable in all geometries with any electrode pairs.
2. The choice of electrode geometry has no effect on average sensitivity, but does affect sensitivity to spatial changes in velocity.
3. Plate (and virtual plate) electrodes provide the most uniform spatial averaging for the simulated electrodes due to their spread out surface area.
4. Choice of flowmeter geometry, i.e. pipe diameter or tank/channel width, have the largest impact on measurement sensitivity.
5. The ideal electrode spacing is the width of the excitation coil, or the tank (whichever is smaller).

Chapter 3

SIGNAL PROCESSING

The signals recorded by the instrumentation are more complicated than the expected values indicated by Chapter 2. This is due to a number of simplifying assumptions, such as that of a time invariant magnetic field, necessary to simplify the calculations. In practice, the instrumentation measures a superposition of signals, including but not limited to: the desired flow signal, time varying interference, 50 Hz mains power interference, random 'white' Gaussian noise, and some low frequency $1/f$ Gaussian noise causing a random drift [Keshner 1982]. Figure 3.1 shows some raw data (after applying a mains filter) measured from three separate experiments, each with a different flow speed. The signal amplitude is of the order of 1 mV, three orders of magnitude larger than the expected flow signal amplitude of $\approx$1.1 µV with flow speeds of $\approx$1 mm s^{-1}. The fundamental problem for the signal processing is trying to measure the small flow voltages in the presence of interference and $1/f$ noise.

3.1 MAINS FILTERING

Mains interference is present in the laboratory setting caused by the power wiring in the walls and floor of the building. There are three phases present and an unknown amount of current flowing. This produces an unknown amount of electrical coupling and magnetic coupling which cannot be effectively shielded against. The removal of this unknown 50 Hz interference is facilitated by a 50 Hz digital 8-tap moving average filter, shown in Figure 3.2 with stop-bands at 50 Hz, 100 Hz, 150 Hz, and 200 Hz. Figure 3.3 shows the results from applying the mains filter to the measured signal. Alternative filtering methods, such as those used in biomedical applications [Levkov et al. 2005], could also be applied.

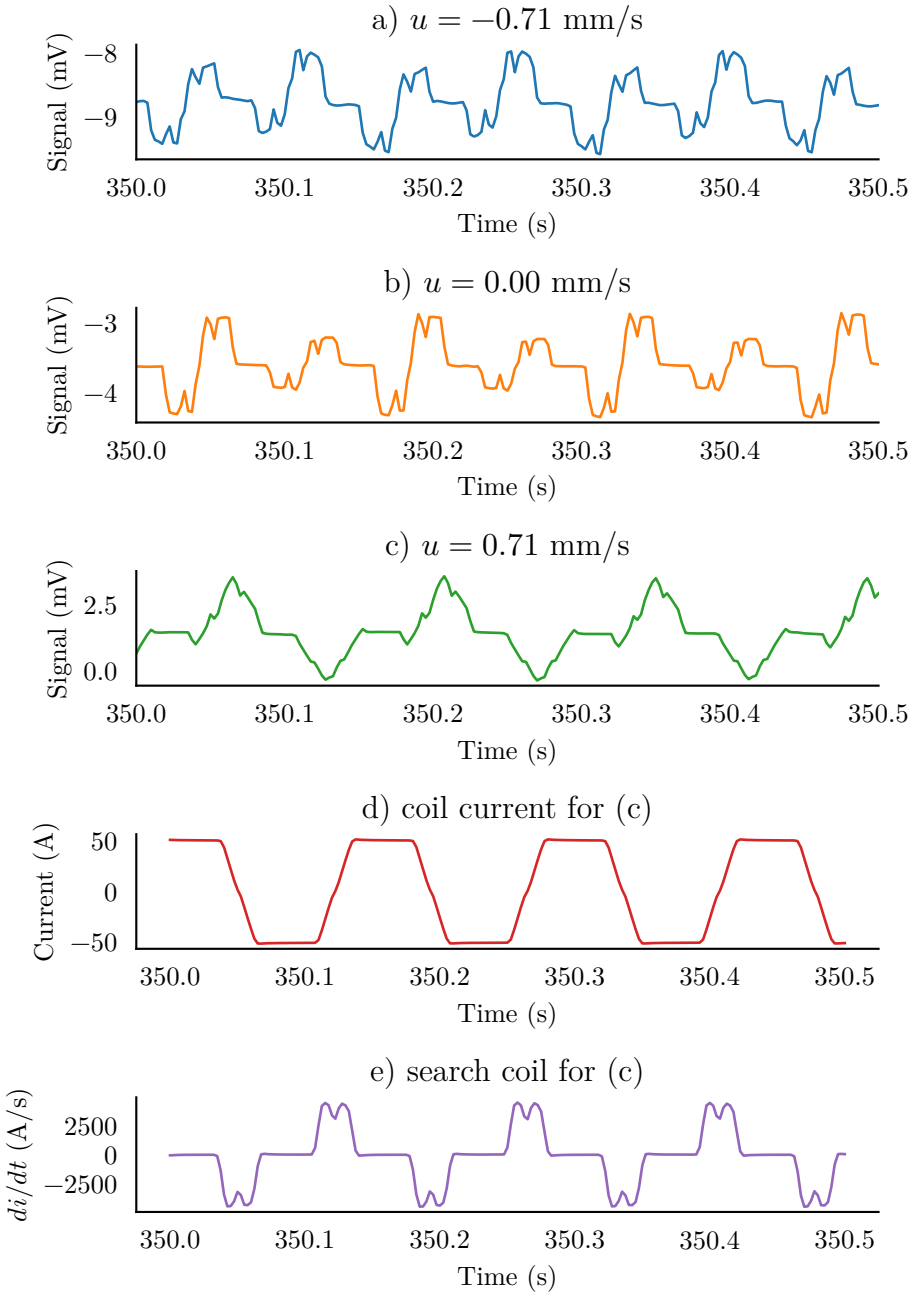

Figure 3.1 Sections of the voltage signals measured at the electrodes from three experiments with different flow speeds. The only processing is a mains filter to remove the 50 Hz interference. These signals all show different interference with different mean offsets and amplitudes. The measurements were taken in the mini-aquifer with 7 Hz excitation.

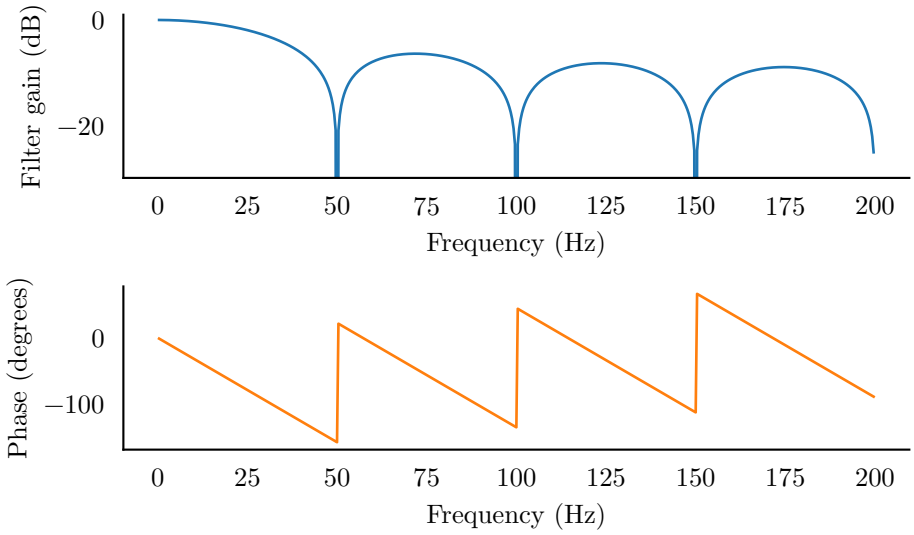

Figure 3.2 Filter response for the 50 Hz mains 8-tap moving average filter.

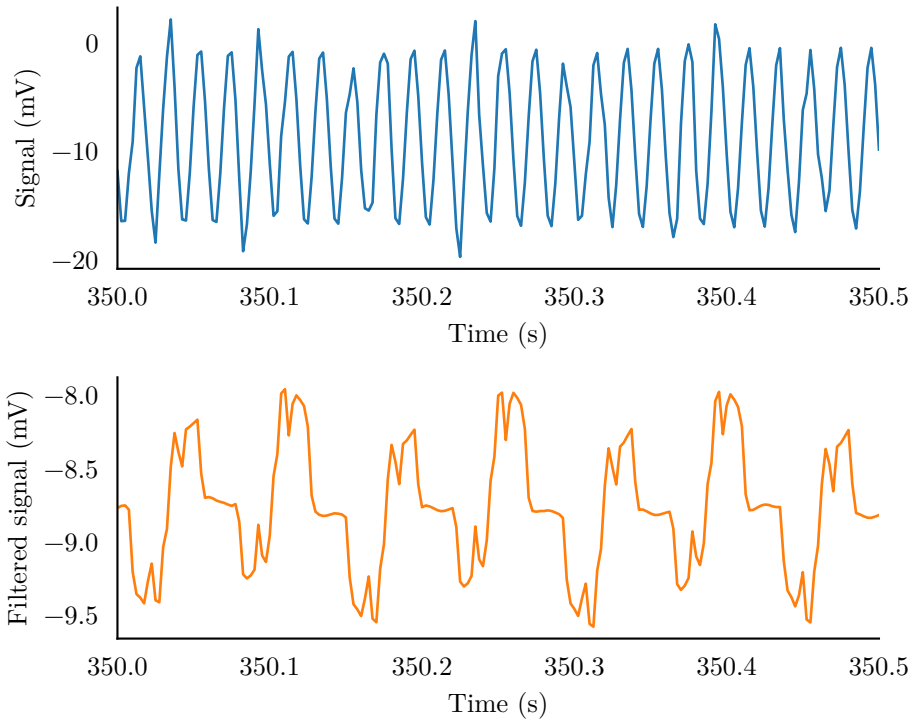

Figure 3.3 Plot of the raw measured signal before and after the application of the mains filter. Note the change in signal amplitude.

3.2 SYSTEM NOISE

Electrical noise is pervasive and unavoidable. In this experiment, two types are expected and measurable: additive 'white' Gaussian noise and low frequency $1/f$ Gaussian

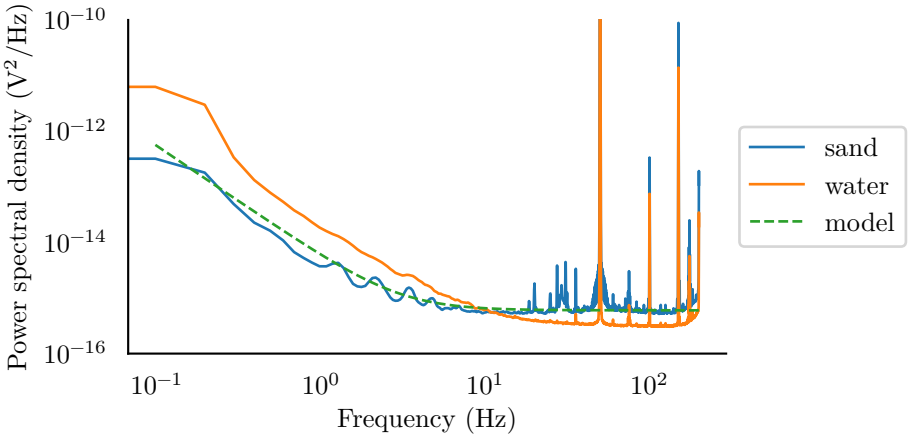

Figure 3.4 Power spectral density plot of the system noise. This shows a clear $1/f$ power law below 7 Hz and white noise (and 50 Hz interference and its harmonics) above. The model shown uses the parameters f_c=3 Hz, β=2, and n=6×10^{-16} V^2 Hz^{-1}.

noise [Horowitz and Hill 2015]. Figure 3.4 shows the power spectral density (PSD) from a background noise measurement taken over 8 hours with no excitation and a Blackman-Harris window applied [Mack 2013, Nuttall 1981]. The noise has been modelled as

$$S_n(f) = \left[\left(\frac{f}{f_c} \right)^{-\beta} + 1 \right] N_0 \,, \tag{3.1}$$

where f_c is the corner frequency, β is the noise power, and N_0 is the power spectral density of the white noise. (3.1) fits the measured spectrum in Figure 3.4 with values of $f_c = 3$ Hz, $\beta = 2$, and $N_0 = 6 \times 10^{-16}$ V^2 Hz^{-1}. Figure 3.4 also shows a comparative PSD for the same noise measurement without the presence of the sand. As the sand is a higher resistance path, there is a slightly higher noise floor. However during the noise measurement, air bubbles were seen to form on the electrodes in the water reducing the contact area. Due to the 20× amplification present on the instrumentation front-end, the noise from the remaining electronics is reduced below this noise floor and can be ignored. The noise measured is thus generated in the experiment tank and the electrodes themselves.

3.3 MAGNETIC INTERFERENCE

There are two distinct types of interfering signals also being measured by the electrodes, distinct from the noise in that they are not random signals. A transformer effect is present, as described by Faraday's law [Hemp and Sanderson 1981]. The alternating magnetic flux cutting through the measurement loop generates a measurable voltage across the electrodes, orders of magnitude greater than the desired flow signal. This

interference is modelled as

$$v_{\text{transformer}}(t) = \frac{\mathrm{d}\Phi(t)}{\mathrm{d}t}\,, \tag{3.2}$$

where Φ is the magnetic flux intersecting the measurement loop which is defined as

$$\Phi(t) = \int_S \mathbf{B}(t) \cdot \hat{\mathbf{n}}\,\mathrm{d}S = AB(t)\,, \tag{3.3}$$

with the measurement loop surface S, effective magnetic field strength, $B(t)$, and effective loop area, A. With an electromagnetic coil generating the magnetic field, the field strength $B(t)$ is proportional to the energising current $i(t)$ such that

$$\Phi(t) = AB(t) = Ak_M i(t)\,, \tag{3.4}$$

where k_M is a magnetic coupling coefficient. Substituting (3.4) into (3.2) gives

$$v_{\text{transformer}}(t) = \frac{\mathrm{d}(Ak_M i(t))}{\mathrm{d}t}\,, \tag{3.5}$$

$$= Ak_M \frac{\mathrm{d}i(t)}{\mathrm{d}t}\,, \tag{3.6}$$

under the assumption that the loop geometry remains constant over time. Figure 3.5 shows a comparison of some measured data and the first derivative of current. This shows the measured signal contains a strong magnetic component, approximately 2 mV in amplitude whereas the expected flow signal is in the order of 1 µV. The amplitude of this transformer signal is defined by the measurement loop geometry, the rate of change of the excitation current, and the excitation coil. Given a large, misaligned loop, the transformer signal has the potential to exceed 1 V which can drown out the flow signal or saturate the instrumentation.

3.4 ELECTRICAL INTERFERENCE

The second source of interference is capacitive coupling between external electric fields and the electrodes. There are a number of potential sources such as the power supply and the voltage across the excitation coil, $v_{\text{coil}}(t)$. The primary source of this interference is the electric fields surrounding the excitation coil and its power supply as it switches through its waveform. These transitions occur in phase with the flow signal and can easily be misinterpreted during parameter estimation. The electric fields from the alternating sources couple capacitively into the electrodes as shown in Figure 3.6. When the capacitances, C_1 and C_2, are different, the signal $v(t)$ becomes a common mode signal and manifests at the output as $\gamma \mathrm{d}v(t)/\mathrm{d}t$. Figure 3.7 shows some raw measured data superimposed with the time derivative of the coil voltage, $\mathrm{d}v_{\text{coil}}(t)/\mathrm{d}t$. The measured

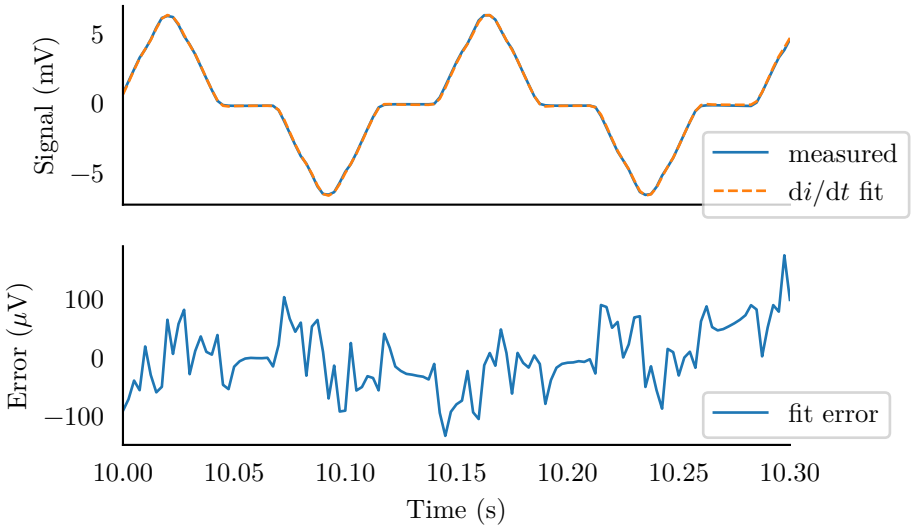

Figure 3.5 Plot of a section of the measured signal, mains filtered and with zeroed mean, superimposed with the time derivative of the excitation current.

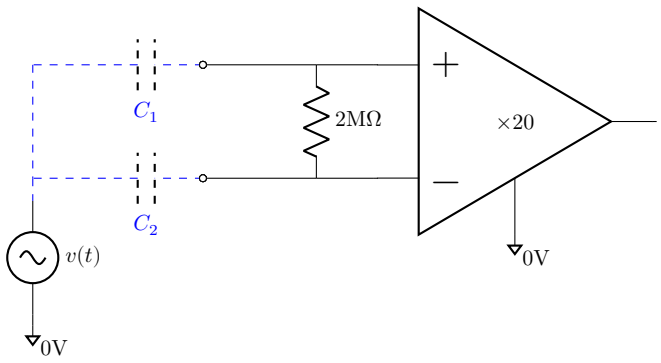

Figure 3.6 Schematic diagram showing the capacitive coupling from an external AC voltage source such as the excitation coil. The capacitances, C_1 and C_2, represent two distinct paths to the electrodes. If the capacitances are equal then the differential measurement cancels the interference out. However, in practice, $C_1 \neq C_2$, and the instrumentation measures the time derivative of the source signal, $\mathrm{d}v(t)/\mathrm{d}t$.

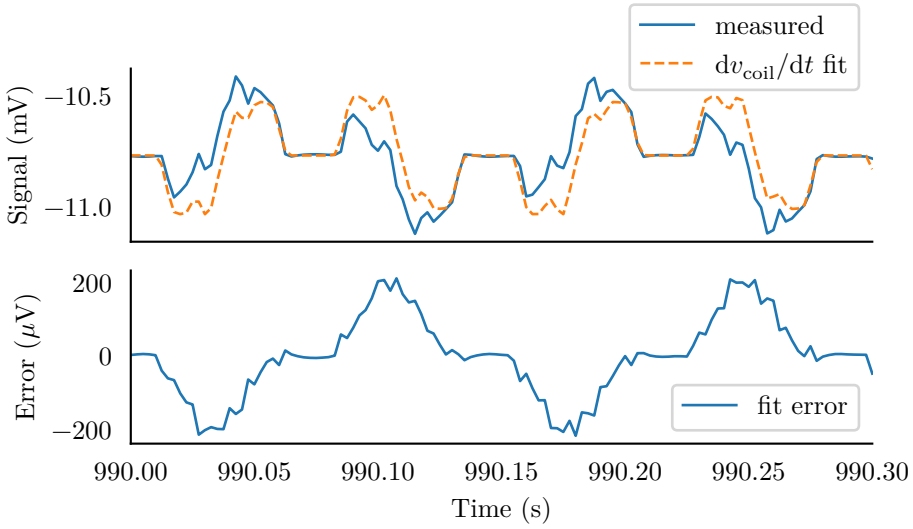

Figure 3.7 Plot of a section of the measured signal, superimposed with the time derivative of the excitation voltage. The measured signal exhibits the capacitive interference in addition to other signals.

signal has a strong component proportional to this interference. Figure 3.8 shows an ordinary least squares (OLS) fit using both the transformer and capacitive interference functions.

The capacitive interference signal is defined as a linear combination of several sources, each with their own coefficient,

$$v_{\text{capacitive}}(t) = \gamma \frac{\mathrm{d}v_{\text{coil}}(t)}{\mathrm{d}t} \,. \tag{3.7}$$

The coupling coefficient, γ, has the form

$$\gamma = CR' \,, \tag{3.8}$$

where C is the capacitance from the source to the electrode and R' is the effective resistance of the instrumentation as seen by the interference source. In practice, the effective capacitance and input impedance can be difficult to determine due to the presence of the electrodes. However, since the γ coefficients contain no information about the flow speed, their physical values can be ignored after parameter estimation.

3.5 FLOW SIGNAL

The flow signal is modelled after the empirical equation, (1.7),

$$v_{\text{flow}}(t) = kS\frac{B}{I} i(t)u(t) \,, \tag{3.9}$$

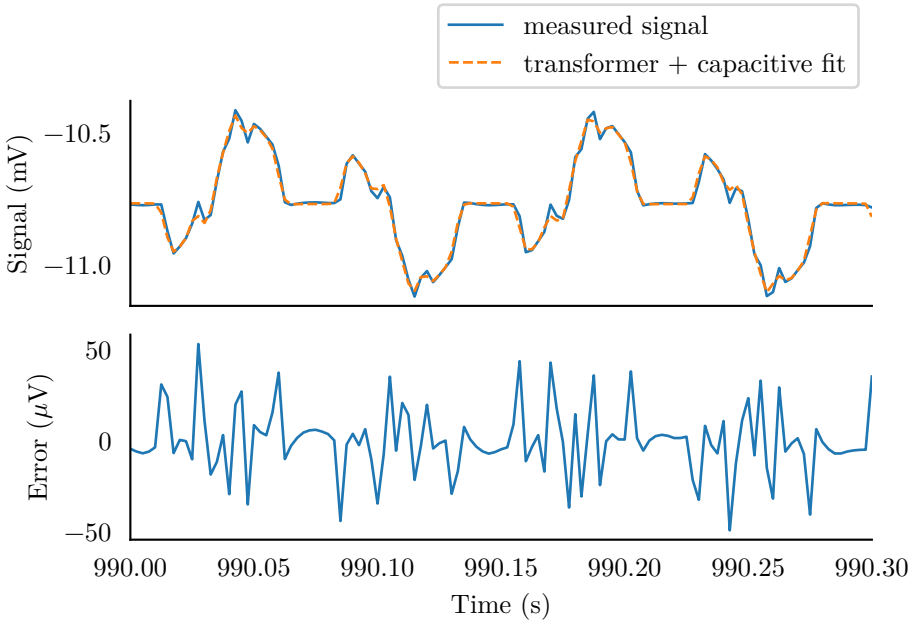

Figure 3.8 Plot of the same signal in Figure 3.7, superimposed with an OLS fit using both transformer and capacitive models. The combination of the two functions provides a good fit to the measured data.

where k is the sensitivity scale factor, B is the mean magnetic field strength during steady state, I is the steady state current, S is the electrode separation, $u(t)$ is the flow speed, and $i(t)$ is the excitation current. The values for k and B/I are scaling coefficients and can be estimated numerically through simulations as described in Chapter 2.

3.6 INPUT MODEL

The input model for the instrumentation is shown in Figure 3.9. The measured voltage, $v_i(t)$, is a super position of the voltage across the input resistance, R_i, induced by the individual sources, $v_f(t)$, $v_b(t)$, and $v_e(t)$. The steady state model is shown in Figure 3.10 where the magnetically coupled and electrically coupled interferences have been eliminated. The source impedance, R_s, has a value in the 1 kΩ to 10 kΩ range and the magnitude of the electrodes impedance is less than 10 Ω. The instrumentation input impedance is 2 MΩ resulting in $v_i(t) = 0.995 v_f(t)$ during steady state periods.

The total measured signal can be approximately modelled as a linear combination of the various interference effects and the flow signal as

$$y(t) = v_{\text{flow}}(t) + v_{\text{transformer}}(t) + v_{\text{capacitive}}(t) + n(t) + m(t) + c\,, \tag{3.10}$$

where $n(t)$ is the noise term, $m(t)$ is the mains interference, and c is the mean offset.

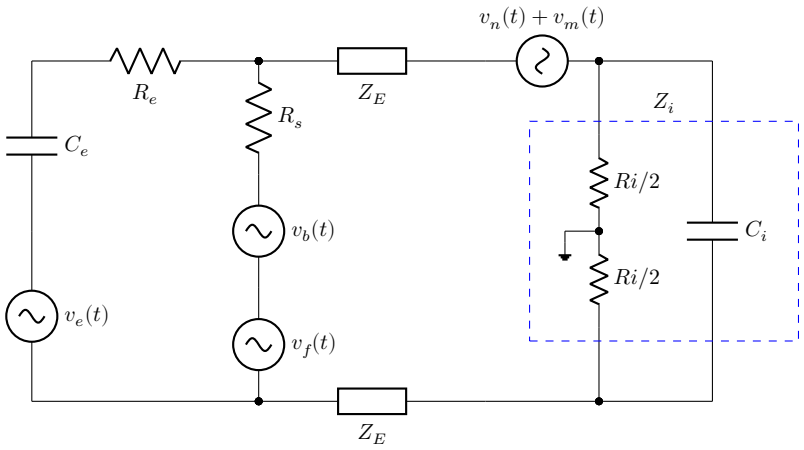

Figure 3.9 Input model for the instrumentation including the electrically and magnetically coupled interference sources. The voltage across in the input resistance, R_i, is the input for the signal processing. The capacitance, C_i, is a combination of the instrumentations input capacitance and the capacitance of the input cabling. The three source terms, $v_f(t)$, $v_b(t)$, and $v_e(t)$ represent the sources of the flow signal, magnetically coupled interference, and electrically coupled interference terms respectively. The $v_n(t) + v_m(t)$ source represents the random noise and mains signals picked up by the instrumentation. The two electrodes, Z_E, can be modelled with constant phase elements. R_s represents the resistive path through the water between the electrodes, and R_e and C_e the impedance of the electrical coupling path.

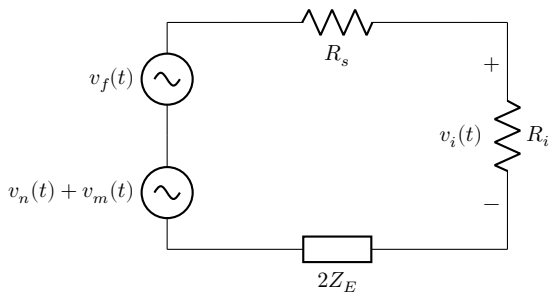

Figure 3.10 Steady state input model for the instrumentation. The capacitively coupled interference and the input capacitance have been removed as open circuits. The magnetic interference source is modelled as $v_b(t) \propto \mathrm{d}i/\mathrm{d}t$ and is zero during steady state periods. The resulting circuit is a voltage divider where $v_i(t) = (v_f(t) + v_n(t) + v_m(t))R_i/(R_i + R_s + 2Z_e)$, and if $R_i \gg R_s + 2Z_E$ then $v_i(t) \approx v_f(t) + v_n(t) + v_m(t)$.

The mains filter, $M(t)$ is applied such that

$$m(t) * M(t) = 0\,, \tag{3.11}$$

where $*$ is the convolution operator, and

$$\begin{aligned} y_M(t) &= y(t) * M(t) && (3.12)\\ &= \big(v_{\text{flow}}(t) + v_{\text{transformer}}(t) + v_{\text{capacitive}}(t) + n(t) + c\big) * M(t)\,. && (3.13) \end{aligned}$$

The resultant model, combined from (3.6), (3.7), (3.9), and (3.13) is

$$y_M(t) = \alpha i_M(t) + \beta \frac{\mathrm{d}i_M(t)}{\mathrm{d}t} + \gamma \frac{\mathrm{d}v_{\text{coil}\,M}(t)}{\mathrm{d}t} + n_M(t) + c\,, \tag{3.14}$$

where

$$\alpha = kS\frac{B}{I}u(t)\,, \tag{3.15}$$

$$\beta = k_M A\,, \tag{3.16}$$

and γ is the electrical coupling coefficient with no flow speed information, and c is a constant DC offset.

3.7 PARAMETER ESTIMATION

The model, (3.14), is linear in the unknown parameters with additive Gaussian noise. Therefore linear least squares is applicable. However, the presence of the coloured $1/f$ noise is likely to introduce a bias into the estimate. The application of an OLS linear estimator gives the estimates for the values of α, β, γ, and c. The system can be expressed in matrix form

$$\mathbf{y} = \mathbf{A}\mathbf{x} + \varepsilon\,, \tag{3.17}$$

where

$$\mathbf{y} = \begin{bmatrix} y_M[1] \\ y_M[2] \\ \vdots \\ y_M[N] \end{bmatrix}, \tag{3.18}$$

$$\mathbf{A} = \begin{bmatrix} i_M[1] & i'_M[1] & {v_{\text{coil}}}'_M[1] & 1 \\ i_M[2] & i'_M[2] & {v_{\text{coil}}}'_M[2] & 1 \\ & & \vdots & \\ i_M[N] & i'_M[N] & {v_{\text{coil}}}'_M[N] & 1 \end{bmatrix}, \tag{3.19}$$

$$\mathbf{x} = \begin{bmatrix} \alpha \\ \beta \\ \gamma \\ c \end{bmatrix}, \tag{3.20}$$

and ε is the residual error. The signals are sampled as

$$f[i] = f(i\Delta t) \quad \text{and} \quad f_M[i] = (f * M)(i\Delta t)\,. \tag{3.21}$$

OLS provides the estimate for the parameter vector, $\mathbf{x}$, with

$$\hat{\mathbf{x}} = (\mathbf{A}^T\mathbf{A})^{-1}\mathbf{A}^T\mathbf{y}\,. \tag{3.22}$$

Of these coefficients, only α is needed since the estimated flow speed is

$$\hat{u} = \frac{\hat{\alpha} I}{kSB}\,, \tag{3.23}$$

thus solving for the flow speed if the K and G factors are known. Alternatively, the flow signal may be calculated as a voltage using

$$\hat{v}_{\text{flow}} = \hat{\alpha} I\,. \tag{3.24}$$

Figure 3.11 shows the OLS fit of the measured data from a moving gantry experiment and Figure 3.12 shows the fitting residuals. Figure 3.13 shows the estimation of the flow signal from the same experiment as Figure 3.11. The raw measured signal is split into 30 s slices which are then individually processed to estimate the flow signal over time. The resulting flow signal shows strong correlation with the gantry velocity. For the experiment shown, the simulation results in Figure 2.16a give an expected flow signal of 0.75 µV with 0.6 mm s^{-1} velocity and 50 A current. The measured peak-to-peak in Figure 3.13 is approximately 1 µV giving a flow signal of 0.5 µV. However, a bias of 1 µV is present in the estimated flow signal. This offset voltage is greater than the generated voltage of the actual flow speed giving an estimation error of over 100%.

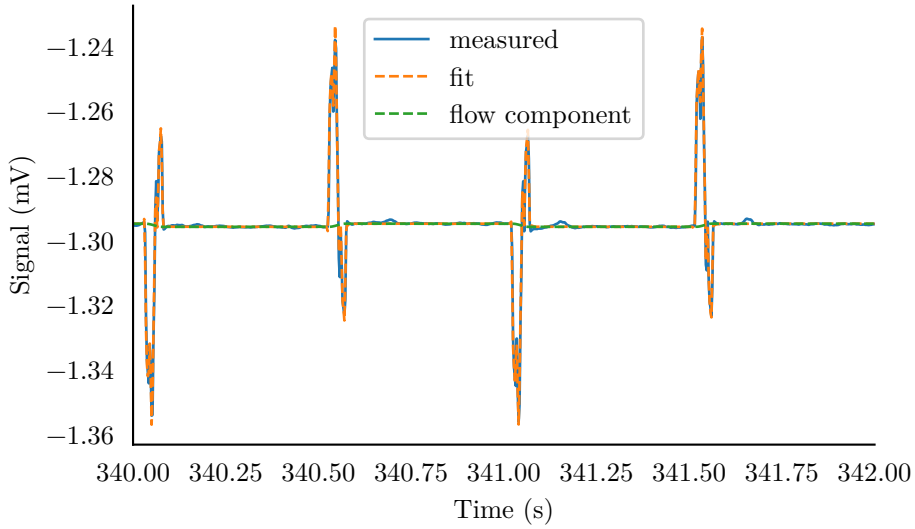

(a) Plot of a section of the measured signal, superimposed with the OLS fit.

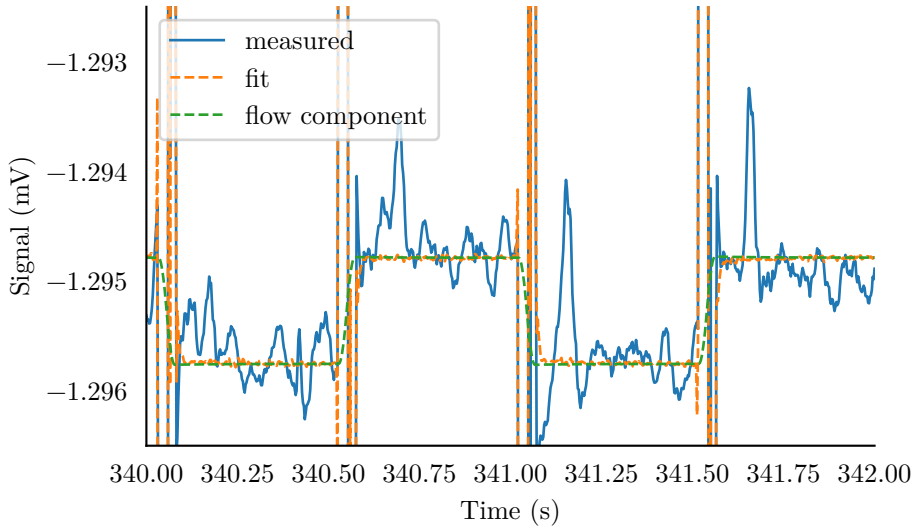

(b) Close-up plot of the section of the measured signal, superimposed with the OLS fit. The flow component has a peak-to-peak of approximately 1 µV. Note the appearance of a systematic interference spike occurring approximately 100 ms after each transition.

Figure 3.11 Plot of a parameter estimation fit for a gantry experiment. The experiment was performed with 1 Hz excitation and a velocity of $0.6\,\mathrm{mm\,s^{-1}}$.

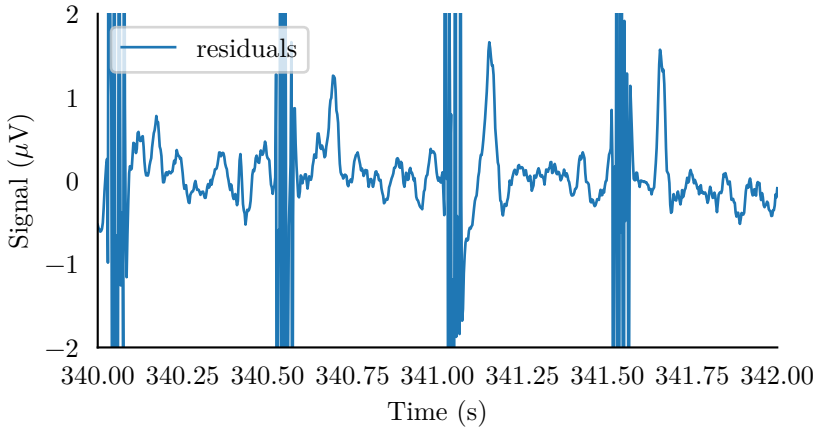

Figure 3.12 Plot of the residuals from parameter estimation for a gantry experiment. During the steady state periods the residual error is consistently reduced. However, during the switching transitions, the model provides a poor fit.

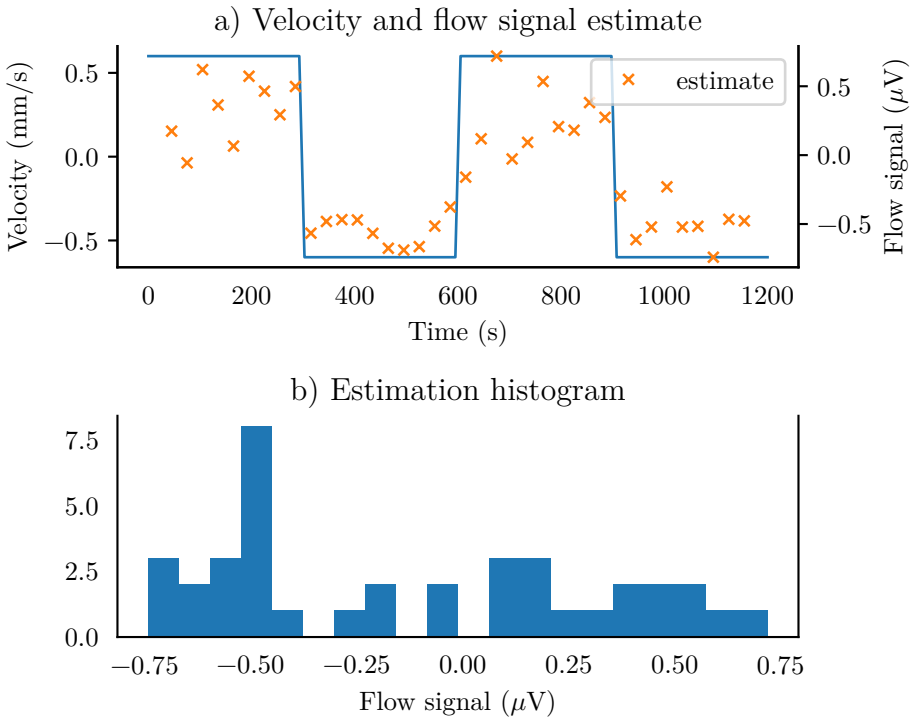

Figure 3.13 Plot of the flow signal estimates for a gantry tank experiment moving at $0.6\,\mathrm{mm\,s^{-1}}$. The estimations resemble the gantry velocity with a large variance. The estimated flow signal for this experiment, read as half of the peak-to-peak, is approximately $0.5\,\mu\mathrm{V}$. Simulations of this geometry give an expected flow signal of $0.75\,\mu\mathrm{V}$.

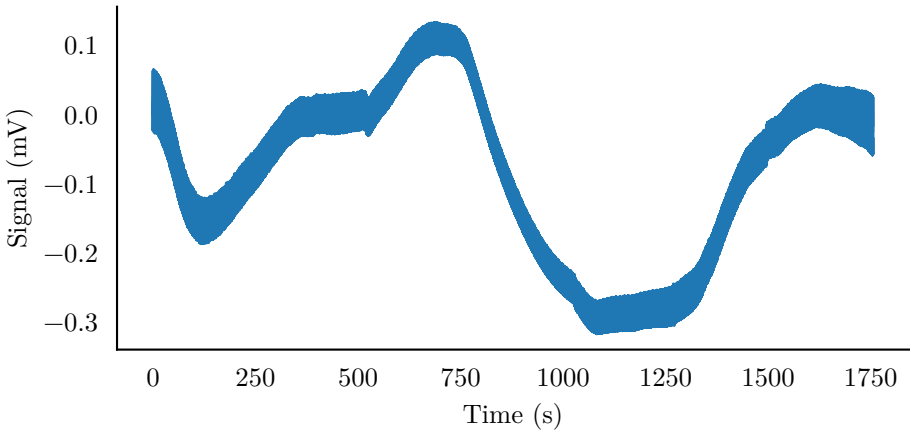

Figure 3.14 Plot of the measured signal in an experiment exhibiting the random walk over time. This is indicative of a coloured noise spectrum. The thickness of the line is due to the presence of the magnetic interference spikes.

3.8 GENERALISED LEAST SQUARES AND SIGNAL PRE-CONDITIONING

Given the model of the noise shown in (3.1), the samples measured from any experiment will have noise that is correlated in time. This is visible in the 'random walk' seen in Figure 3.14. OLS assume a white noise model and the addition of coloured noise can introduce a bias into the estimations [Nguyen et al. 1993, Strejc 1980]. Generalised least squares (GLS) is an improvement to OLS which includes a 'de-correlation' method:

$$\hat{\mathbf{x}} = (\mathbf{A}^T\Omega^{-1}\mathbf{A})^{-1}\mathbf{A}^T\Omega^{-1}\mathbf{y}\,, \tag{3.25}$$

where Ω is the non-singular covariance matrix of the noise term, $n(t)$. (3.25) is equivalent to

$$\hat{\mathbf{x}} = (\mathbf{A}^{\dagger T}\mathbf{A}^{\dagger})^{-1}\mathbf{A}^{\dagger T}\mathbf{y}^{\dagger}\,, \tag{3.26}$$

where

$$\mathbf{y}^{\dagger} = \mathbf{C}^{-1}\mathbf{y}\,, \tag{3.27}$$

$$\mathbf{A}^{\dagger} = \mathbf{C}^{-1}\mathbf{A}\,, \tag{3.28}$$

and $\mathbf{C}^{-1}$ is determined using the Cholesky decomposition, $\Omega = \mathbf{C}\mathbf{C}^T$. This has the effect of linearly transforming the original system into a form which can be solved using OLS by de-correlating the noise samples. In practive, the Cholesky decomposition is infeasible due to the size of the matrix. A computationally simpler approximation of

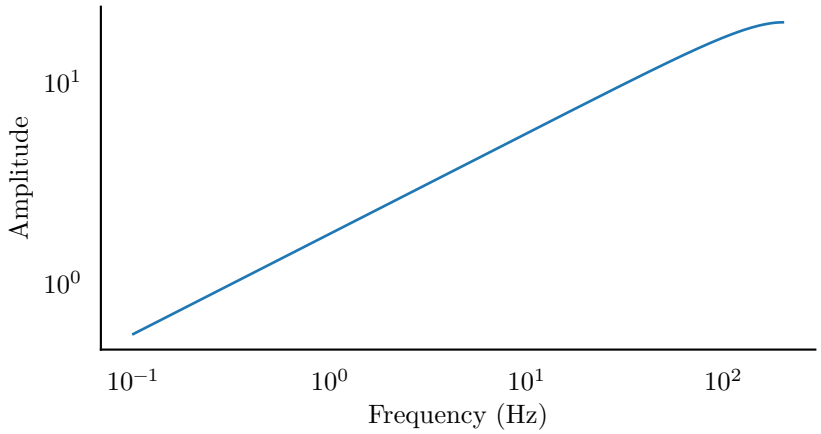

Figure 3.15 Plot of the de-correlating transformation frequency response. This has the same effect as a high-pass filter. Note that there is zero phase delay making this a non-causal filter.

the de-correlating transformation can be performed using

$$Y^{\dagger}[k] \approx \frac{Y[k]}{\sqrt{S_n[k]}}\,, \tag{3.29}$$

where $Y[k]$ is the discrete Fourier transform of $y[i]$ and $S_n[k]$ is the discrete power spectral density model of the noise. This whitening filter has the frequency response shown in Figure 3.15 and is essentially the same as applying a high-pass filter. The result of applying the filter to real measured data is shown in Figure 3.16.

Figure 3.17 shows the estimation of the flow signal from the same experiment as Figure 3.13 with the addition of the prewhitening. This result suggests that the large variance between samples in Figure 3.13 is due to the bias introduced by the OLS algorithm. Note that this bias is introduced on a per-sample basis and thus it appears as a variance in the estimate. With the application of the prewhitening, this per-sample bias is greatly reduced resulting in a strong correlation with the input velocity. However, a 1 µV zero offset is present and constant for the entire experiment. This suggests an error in the model fitting, likely during the switching periods where the model is a poor approximation.

3.9 SIGNAL GATING

The challenges in the signal processing revolve around fitting the interference signals such that they can be removed without affecting the estimate of the flow signal. A common approach when using a bipolar DC supply is to simply ignore samples taken during the transient events while fitting samples taken during the steady state periods. This has the effect of setting $\mathrm{d}i(t)/\mathrm{d}t \approx 0$ and $\mathrm{d}v_{\mathrm{coil}}(t)/\mathrm{d}t = 0$ which removes the interference signal altogether. This is referred to as 'gating' in older analogue applications as this

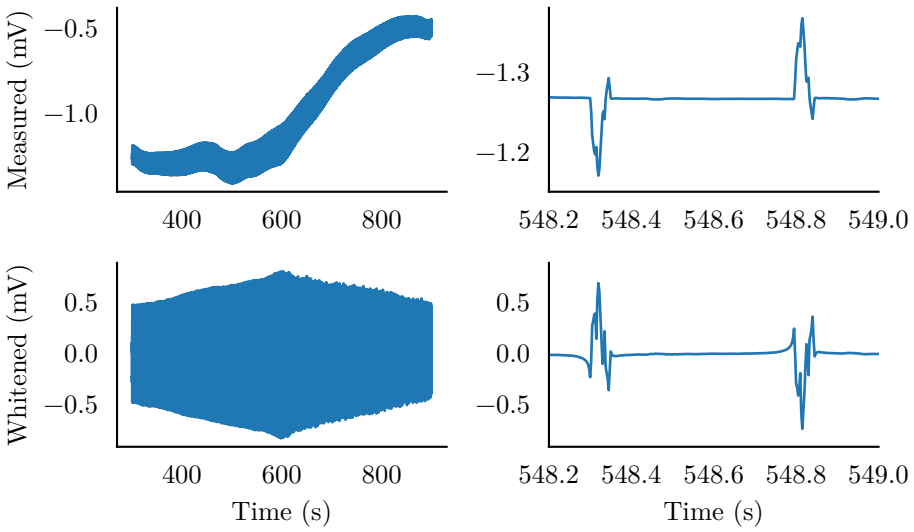

Figure 3.16 Plots showing the effects of the de-correlating transformation, (3.29). The random walk offset is removed from the top row to the bottom while preserving high frequency details.

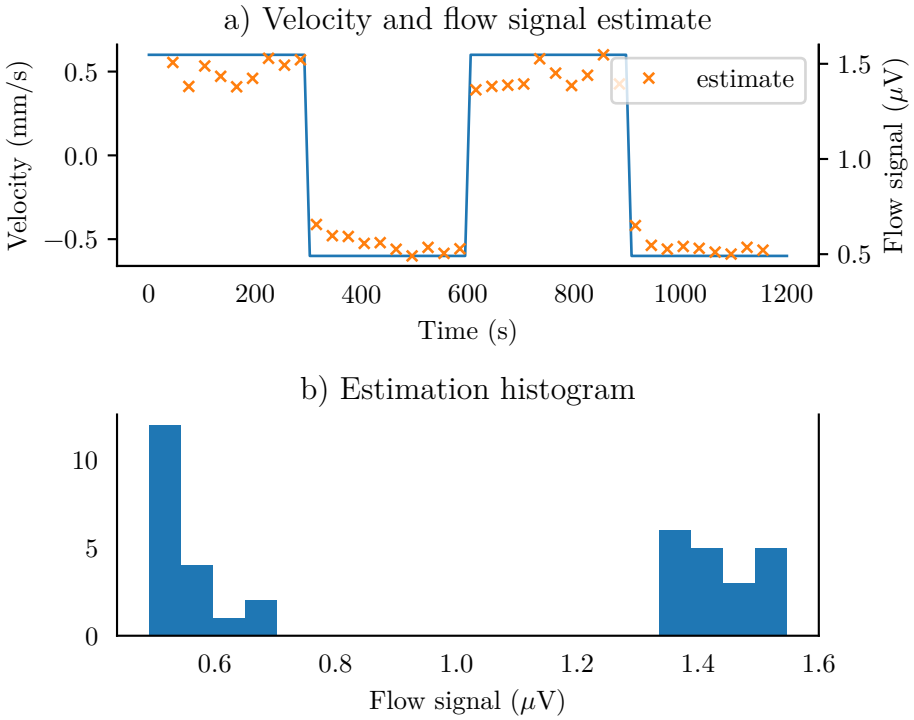

Figure 3.17 Plot of the flow signal estimates for a gantry tank experiment moving at $0.6\,\mathrm{mm\,s^{-1}}$ with prewhitening. The estimations match the input velocity profile with a greatly reduced variance compared to Figure 3.13. However, a bias of $1\,\mu\mathrm{V}$ has been introduced. Simulations of this geometry give an expected flow signal of $0.75\,\mu\mathrm{V}$ while the estimate shows a flow signal of $1\,\mu\mathrm{V}$.

was performed through a gating circuit [Appel et al. 1976, Cushing 1973, Mannherz et al. 1974, Polo et al. 2001].

Figure 3.18a shows a simplistic gating algorithm where the samples are valid when the coil current is considered constant, i.e., $|\mathrm{d}i/\mathrm{d}t| < \epsilon$ where ϵ is a chosen threshold. A closer examination, shown in Figure 3.18b, shows that a large transient response is still present around the leading edge. This is the primary issue with the gating methodology: where is the excitation "steady" enough? An improvement is to require that the previous n samples also pass the threshold before considering a sample as valid. Figures 3.19a and 3.19b shows the samples that are considered when applying a 20 sample requirement on the leading and trailing edges. As the excitation frequency is increased, the fixed switching time means that the available number of samples will decrease. The available number of samples can be calculated with

$$S'_H(f) = \lfloor f_s(\frac{1}{2} - f t_s) \rfloor - 2\varepsilon \,, \tag{3.30}$$

where S'_H is the number of samples available during the hold period for averaging, f_s is the sampling rate, f is the excitation frequency, t_s is the switching time defined by the power supply, and 2ε is the number of leading and trailing samples ignored. Figure 3.20 shows the decreasing number of available samples as the excitation frequency increases as well as the relative increase of the flow signal estimates standard deviation compared to 1 Hz.

Figure 3.21 shows the results from applying the gating algorithm alongside the GLS parameter estimation. The results show the same estimated flow signal amplitude as in Figure 3.17 but with the zero offset greatly reduced to $\approx$1 µV.

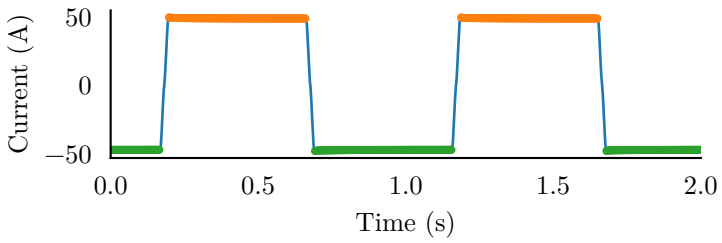

(a) Example of a simple gating algorithm shown here applied to the current signal. The steady-state condition applied is $|\mathrm{d}i/\mathrm{d}t| \leq 500\,\mathrm{A\,s^{-1}}$. The positive and negative regions are differentiated by the sign of the current signal.

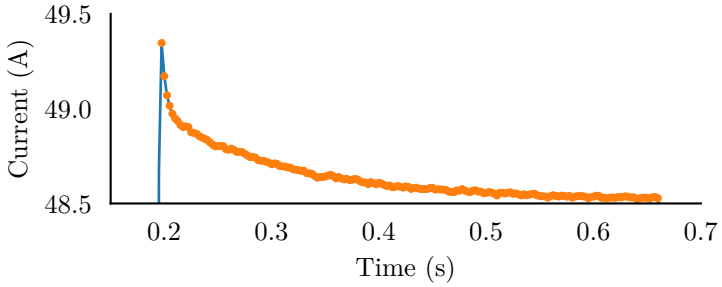

(b) Close-up of the simple gating algorithm showing the inclusion of a strong transient at the leading edge. This overshoot and decay of the current in the excitation coil is caused by the complex impedance of the coil due to the proximity effect. The long RL time constant causes a slow decay.

Figure 3.18 Example of a simple gating algorithm passing sharp transients at the edges.

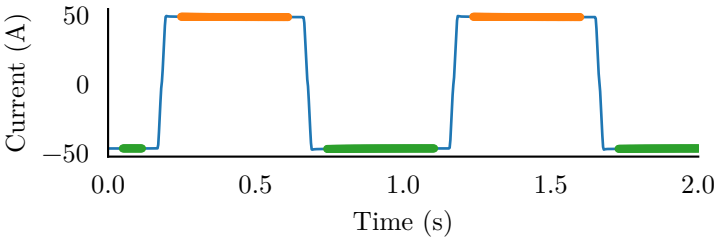

(a) Example of an improved gating algorithm where each sample also depends on the condition of its neighbours.

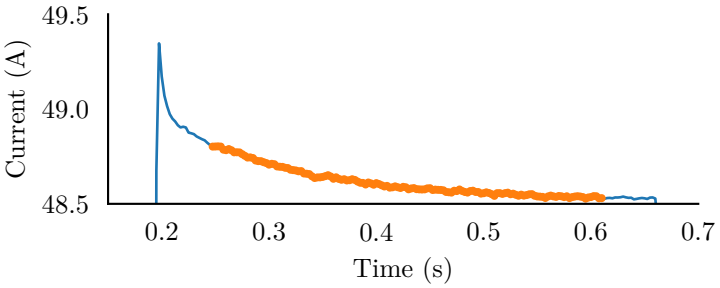

(b) Close-up of an improved gating algorithm where each sample also depends on the condition of its neighbours. In this case each of the 20 previous samples must also pass the gating test for a sample to be considered valid.

Figure 3.19 Example of an improved gating algorithm masking the sharp transients at the edges.

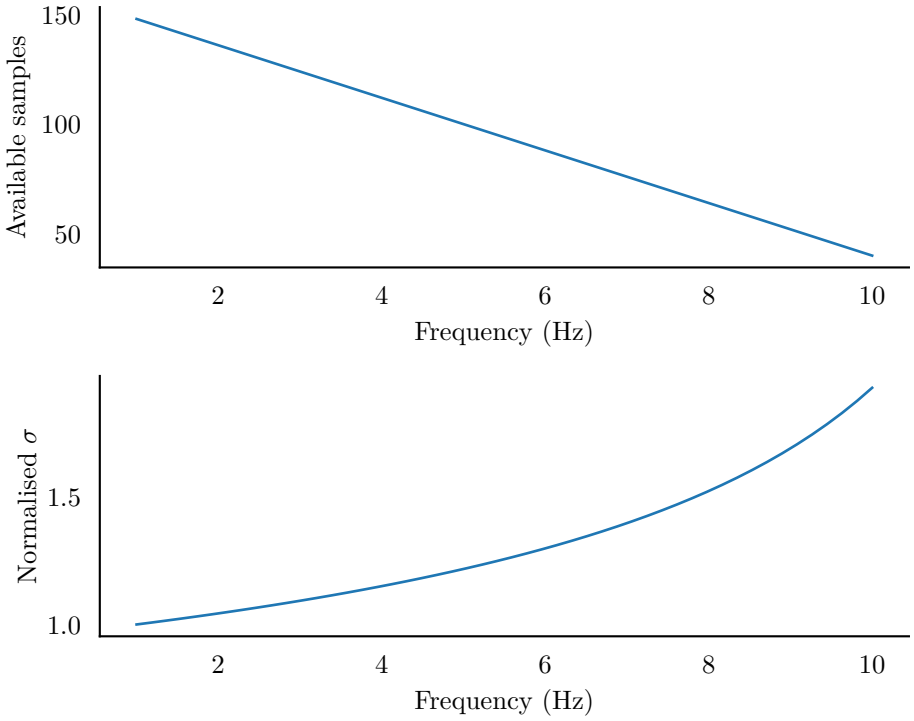

Figure 3.20 Plot showing the number of samples available for averaging as a function of the excitation frequency. The top plot shows how the number of samples decreases linearly as the excitation frequency is increased. The bottom plot shows the relative increase in the standard deviation as the number of samples is decreased relative to 1 Hz.

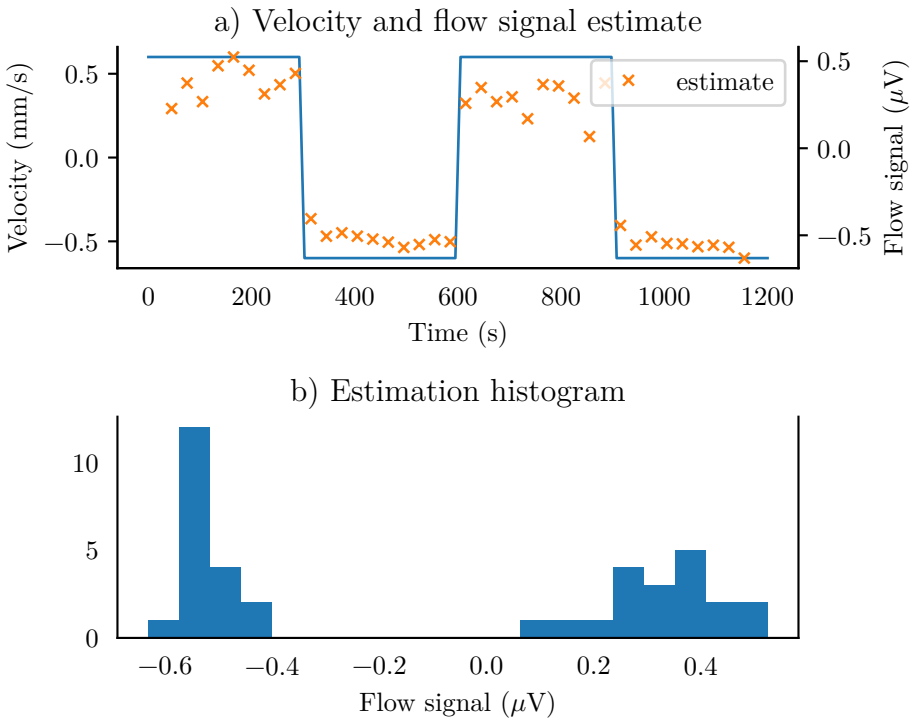

Figure 3.21 Plot of the flow signal estimates for a gantry tank experiment moving at 0.6 mm s^{-1} with pre-whitening and gating. The bias has been greatly reduced from Figure 3.17 with a small increase in the variance of the estimates. Simulations of this geometry give an expected flow signal of 0.75 µV.

3.10 SIMULATED SIGNAL GENERATOR

Through construction of a simulated signal using the model described in (3.14), the performance of the parameter estimation methods can be estimated. While this method commits the 'inverse crime' [Colton et al. 1998], it can still be a useful tool to examine the expected *best-case* variance of the estimator output.

The simulated signal can be constructed from three base signals: an excitation current, a coil voltage, and a random noise realisation. The $1/f$ flicker noise can be generated by creating a white noise signal and passing it through a filter with the same frequency response as the amplitude spectral density (ASD) of the desired noise spectrum [Billah and Shinozuka 1990, Zhivomirov 2018]. Figure 3.22 shows a flow diagram of this process. The initial white noise is oversampled by a factor of eight. This is required to calculate the 'true' spectral density without artefacts before applying a rectangle window by measuring it for a given period [Kirchner 2005, Mack 2013]. The final truncation gives the correct number of samples and implicitly applies the same rectangle window to the noise as the other signals. Figure 3.23 shows some realisations of flicker noise matching the PSD of the modelled system noise.

The excitation current and coil voltage are taken from real laboratory experiments. Figure 3.24 shows the separate basis functions that are linearly combined into the simulated signal such as in Figure 3.25. The parameters for the model, (3.14), are then estimated over 1000 trials and the errors are shown in Figure 3.26.

3.11 SIMULATED RESULTS

A synthetic signal generator allows for a wider range of scenarios to be simulated. This can be used to examine how the statistical properties of the output vary. Figures 3.26 and 3.27 show the results from a synthetic simulation at 1 Hz, 4 Hz, and 7 Hz with no

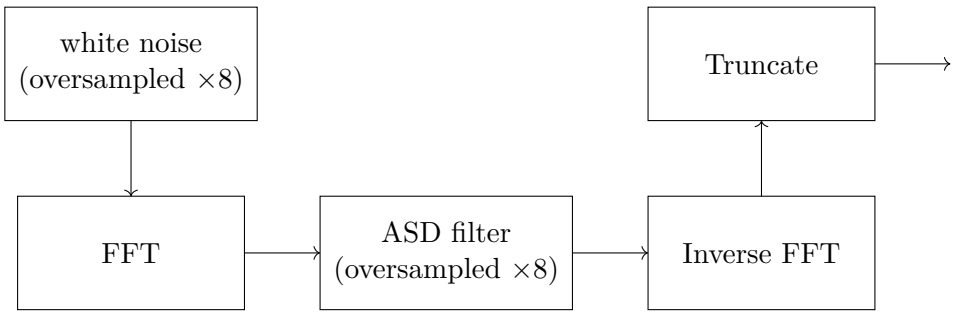

Figure 3.22 Flow diagram for the random coloured noise generator. The white noise is generated using standard normal distributions in time space and then transformed into frequency space. A filter is then applied shaping the noise spectrum as required. Finally the inverse transform is applied and the results are then truncated. The oversampling is required to prevent the implicit rectangle window causing spectral leakage and altering the spectral distribution.

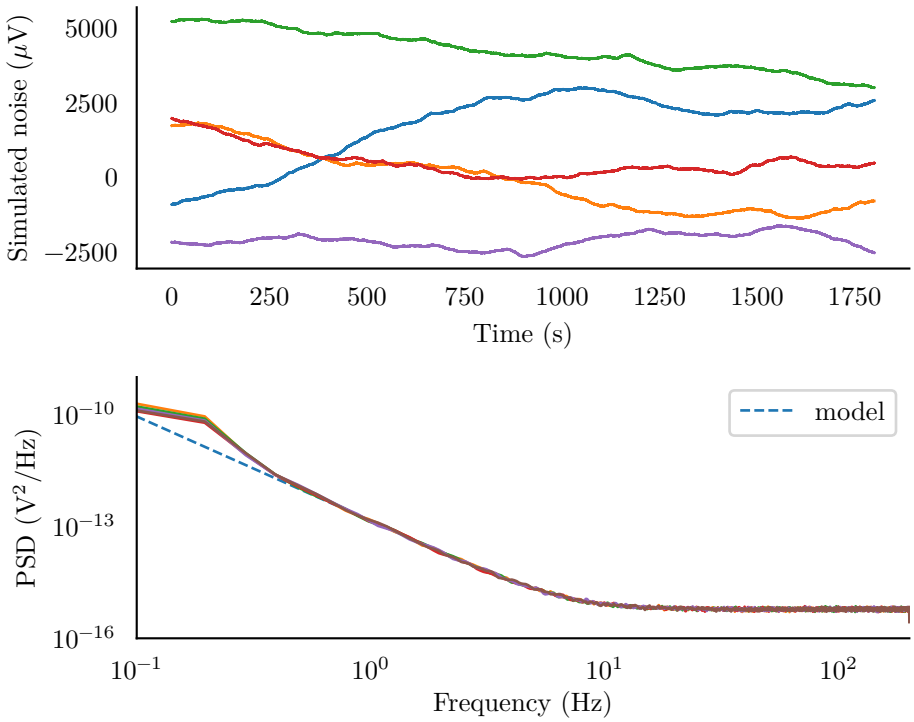

Figure 3.23 Plot of simulated noise signals from system model. These show possible realisations of the system noise present in the experimental system. These show a large random walk over the 30 min period. Note that all the generated signals have the same PSD which matches the model from Figure 3.4.

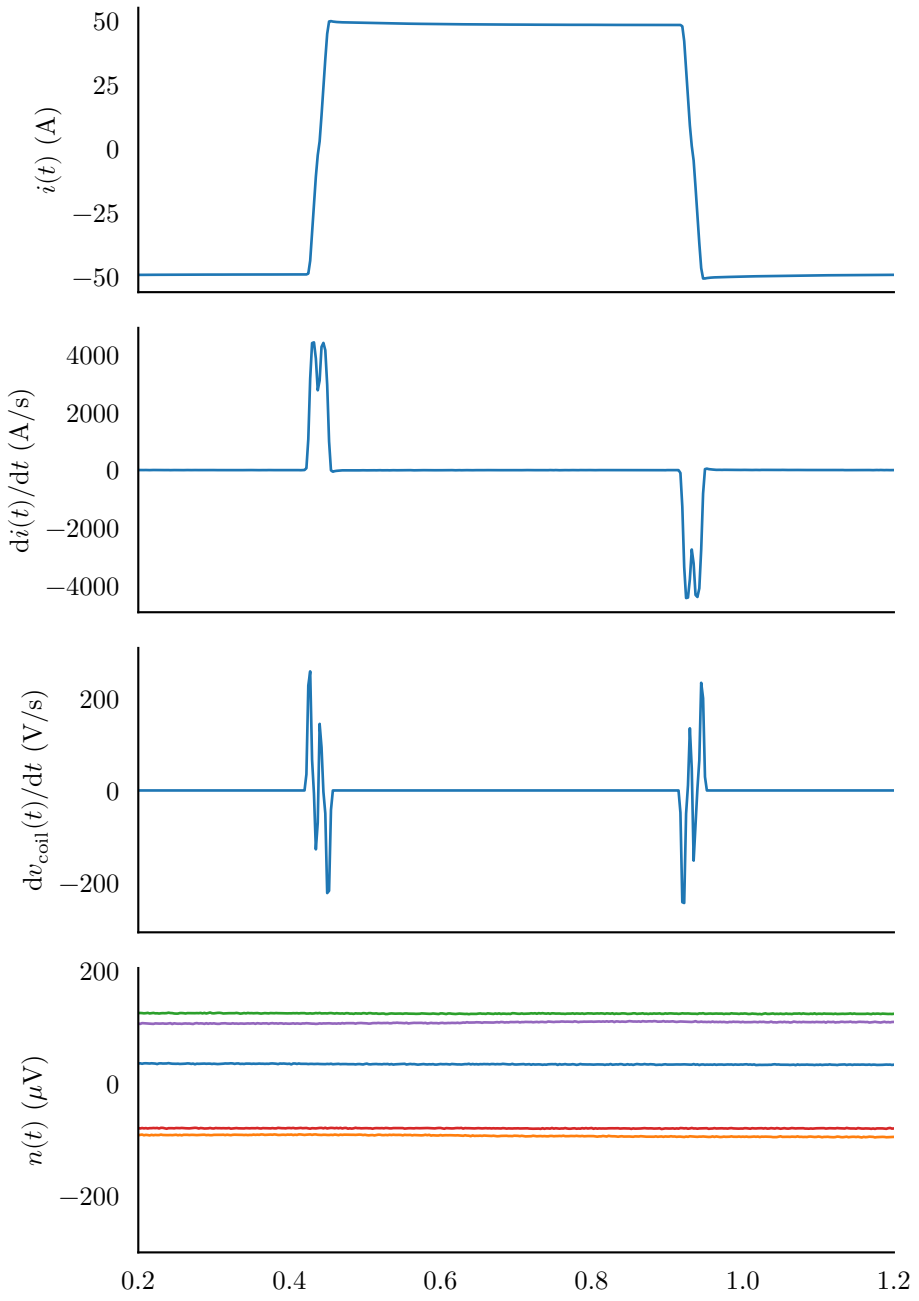

Figure 3.24 Plot of the basis functions used in signal processing simulations. They show the coil current, coil current derivative, coil voltage derivative, and system noise respectively. These are linearly combined to generate a simulated measured signal for testing.

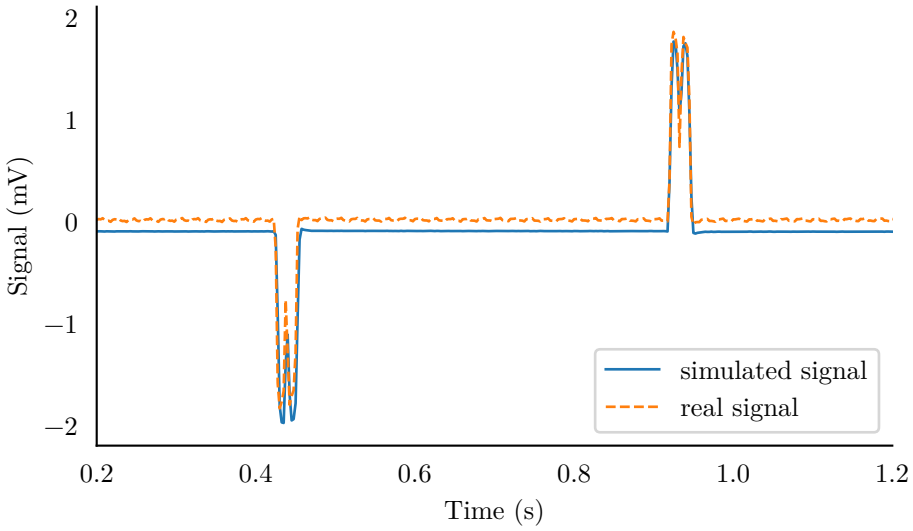

Figure 3.25 Plot of the simulated signal compared with real experimental data.

filtering and a pre-whitening filter respectively. No offset error is present in either result but the standard deviation is reduced by a factor of 10%–20%.

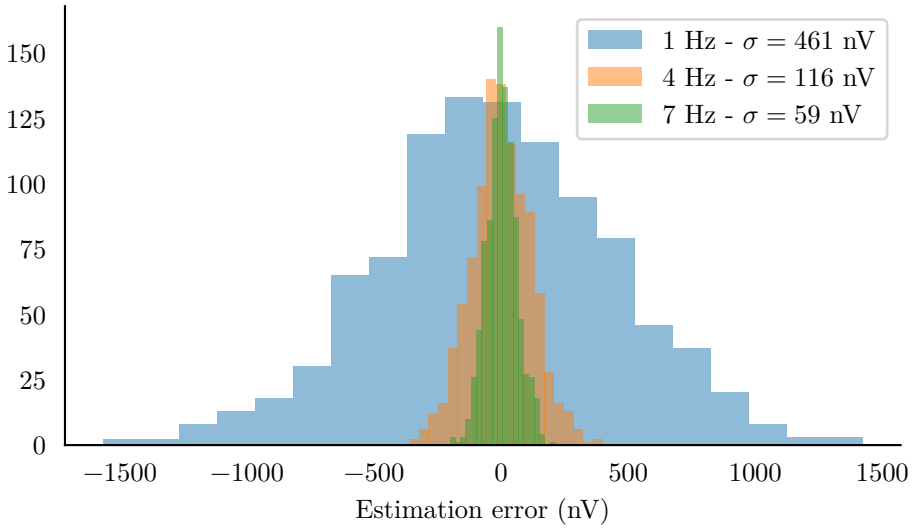

Figure 3.26 Comparison of the estimation errors using different frequencies and a perfect model.

All the previous simulations make use of the same forward and inverse model. A better representation of the real world is to introduce a small error, such as a time shift in the measured signals. Figures 3.28 to 3.31 show the results from applying a 500 µs (0.2 samples) delay between the measured signal and the current and voltage basis functions. Figure 3.28 shows the results without applying any whitening of gating filters. The standard deviation of the output is unaffected, however a large frequency dependant offset is introduced to the error. Figure 3.29 shows the results with the

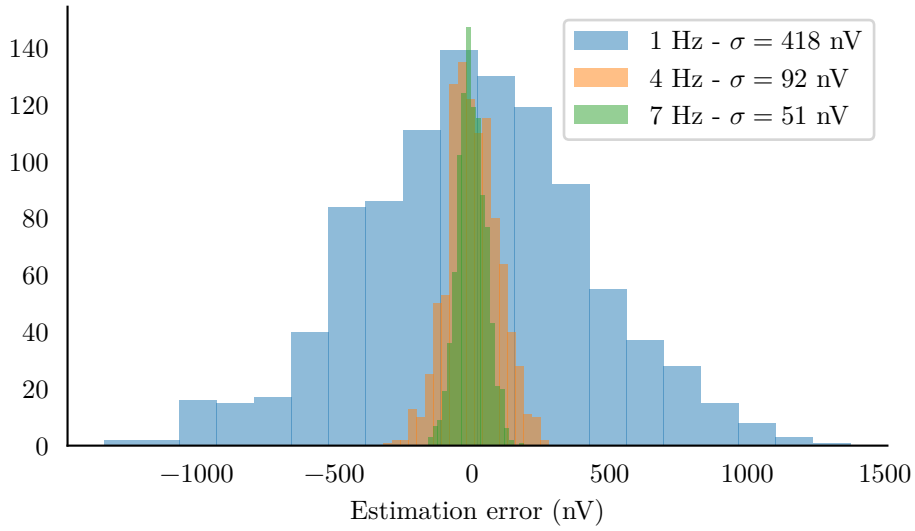

Figure 3.27 Comparison of the estimation errors using different frequencies and a perfect model with pre-whitening. The standard deviation of the errors has been slightly reduced compared to Figure 3.26.

gating algorithm applied. The scale of the errors is increased, however the zero offset is comparatively reduced (or removed in the 1 Hz case). Figure 3.30 shows the results with the pre-whitening applied. As in Figure 3.27, the standard deviation is reduced, however the offset error is increased for all frequencies. Finally, Figure 3.31 shows the results with both the whitening and gating filters applied. In this case the offset is greatly reduced for both 1 Hz and 4 Hz with only a small increase in the standard deviation. Figure 3.32 shows the error standard deviation for sample sizes of varying lengths.

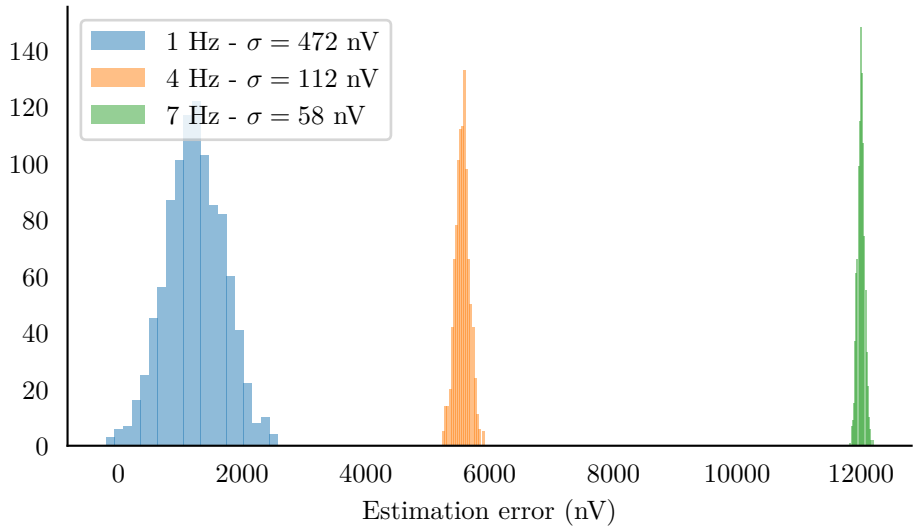

Figure 3.28 Estimation errors fitting a time shifted signal with no filtering. The estimator returns consistent results, however there is a large offset present in the error.

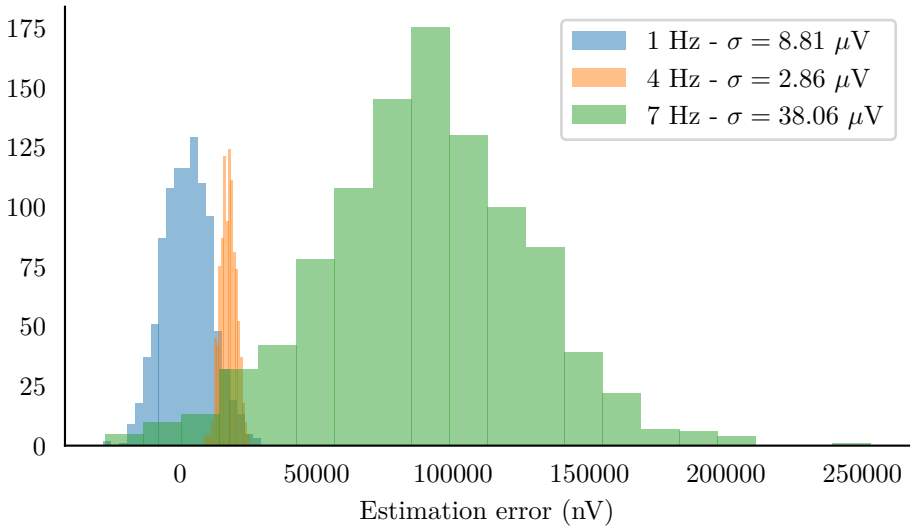

Figure 3.29 Estimation errors fitting a time shifted signal with gating applied. The errors are much larger, however, the offset for 1 Hz is removed.

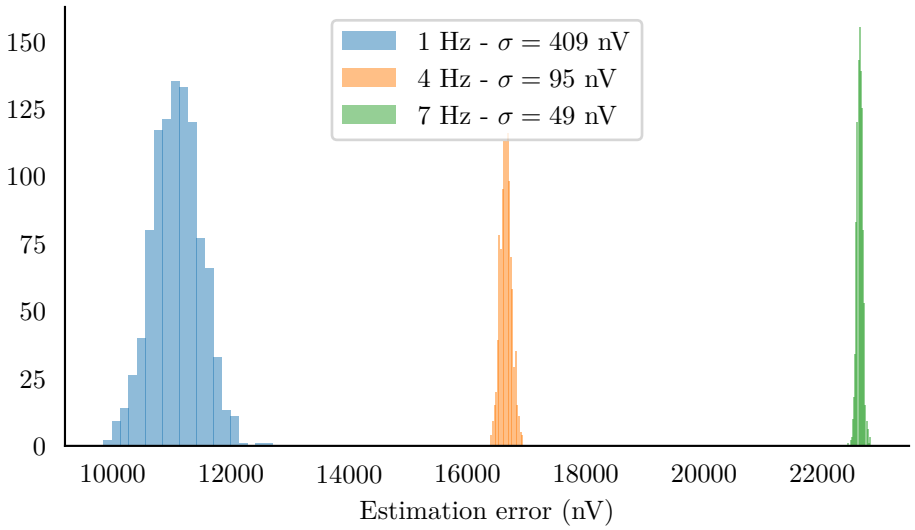

Figure 3.30 Estimation errors fitting a time shifted signal with pre-whitening applied. The mean error values are reduced, however, a large offset value is present with all frequencies.

3.12 SUMMARY

The signals measured from the real world are more complex than the simple voltages suggested in Chapter 2. Multiple sources of interference can be identified. However, a model of these signals can be built and the flow signal can be accurately estimated. Two additional filtering methods are described which can be used to mitigate the estimation error introduced by real world instrumentation and interference. A combination of the gating and whitening algorithms can be used to reduce the large offset errors with only

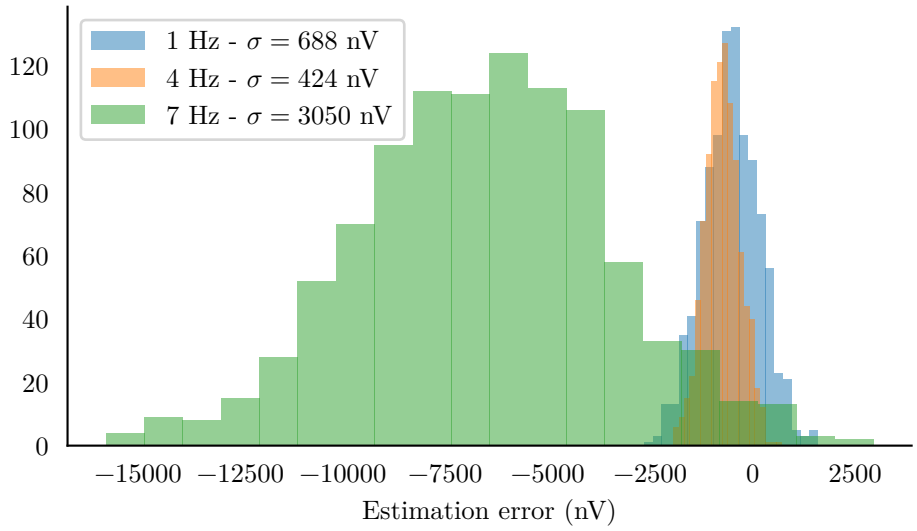

Figure 3.31 Estimation errors fitting a time shifted signal with pre-whitening and gating applied. The mean offset is largely reduced (removed in the case of 1 Hz). The estimation error is slightly increased.

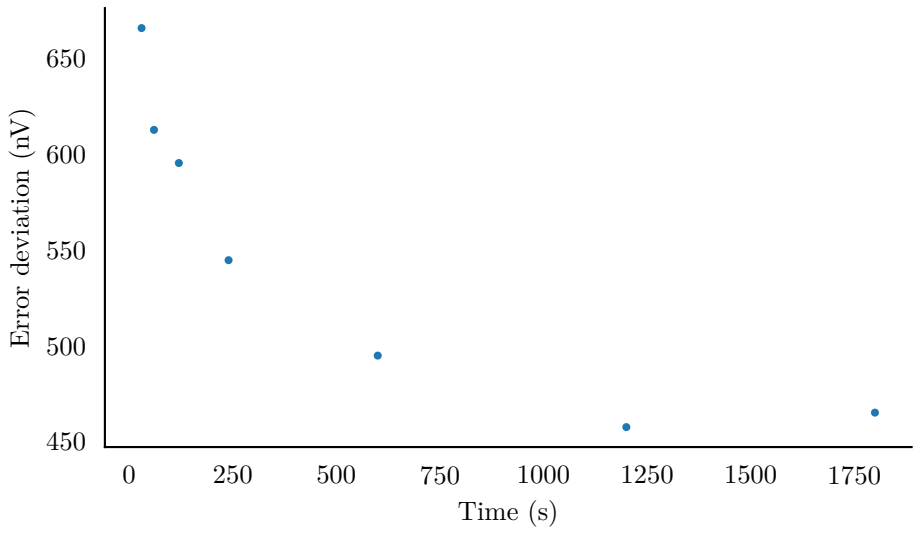

Figure 3.32 Standard deviation of the estimation errors over experiment lengths with a constant excitation frequency of 1 Hz.

a small increase in the output variance.

Chapter 4

INSTRUMENTATION AND EXCITATION

In order to measure the water velocity, the excitation coil must first be powered and the resulting voltages must be measured. This chapter details the instrumentation used, the electrode interface, as well as the desired magnetic excitation and the power supply used to generate the coil current.

4.1 INSTRUMENTATION

The instrumentation for the laboratory is a set of custom built equipment designed specifically for the task [Bonnett et al. 2019]. Figure 4.1 shows a system diagram of the measurement and excitation control systems. The analogue front-end is an AD8421 instrumentation amplifier with an input impedance of 2 MΩ. The analogue to digital conversion is then performed by an ADS1262, shown in Figure 4.2. Four channels are grouped together onto an instrumentation printed circuit board (PCB) shown in Figure 4.3. Up to 16 of these boards can be synchronised to simultaneously sample a fully differential signal with 32-bit precision .[1] Typically, the measurements are taken from a search coil co-located with the primary excitation coil, a pair of silver/silver chloride electrodes measuring voltages in the tank, the mains voltage supply, the excitation coil's current/voltage signals, a magnetic field hall-effect sensor, and a displacement current sensor. The instrumentation PCBs are designed to be clock synchronised from a single master. Alongside the signals used in the signal processing, the instrumentation also monitors a series of thermocouple temperature probes attached to the excitation coil through an optical link for safety and functional isolation. All of the measurement data is collated by the instrumentation boards and then streamed to a laboratory computer and saved to a network drive for offline processing. The excitation coil measurements have an associated noise PSD as shown in Figure 4.4.

[1] Sampling at 400 Hz, the effective number of noise-free bits is 23. The INL of the ADC is 3 ppm.

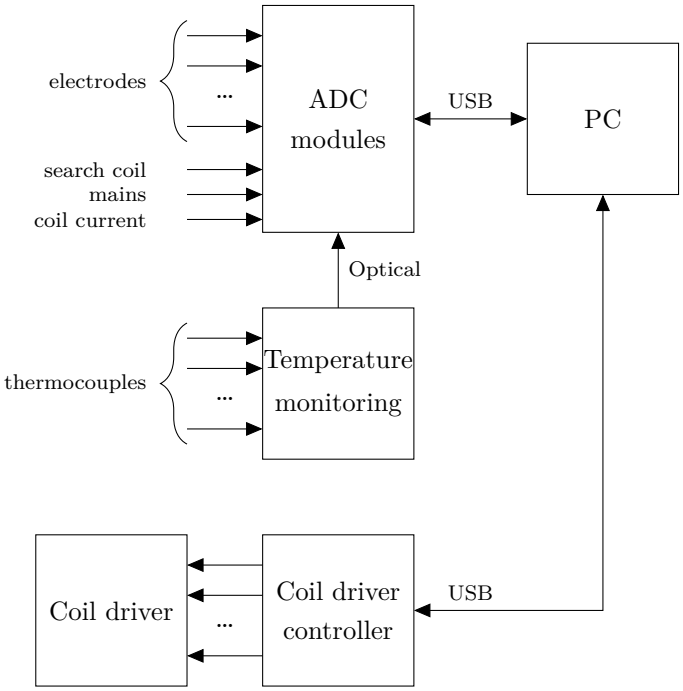

Figure 4.1 System level diagram of the instrumentation. Each analogue-to-digital converter input has its own analogue front-end and signal converter shown in Figure 4.2. All of the cabling used to connect to the analogue-to-digital converter inputs is shielded twisted pair to reduce environmental interference.

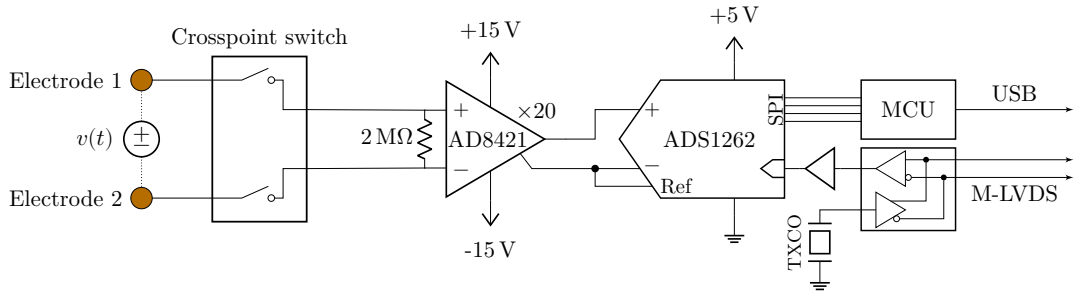

Figure 4.2 Schematic diagram of an input channel measuring the voltage $v(t)$ induced between two electrodes. The electrodes are connected through a crosspoint switch to an instrumentation amplifier (AD8421) with a fixed gain of twenty. The electrode cabling is electrically shielded where possible. The amplifier biases its output around the mid-rail (2.5 V) reference provided by the analogue-to-digital converter (ASD1262). The sampled data recorded by the analogue-to-digital converter are transferred to a microcontroller (MCU) via an serial peripheral interface bus. The analogue-to-digital converter clock is generated from a temperature-compensated crystal oscillator, and synchronised between multiple PCBs via a low-voltage differential signalling serial link. Fanout buffers are used to distribute the clock to each channel on a PCB.

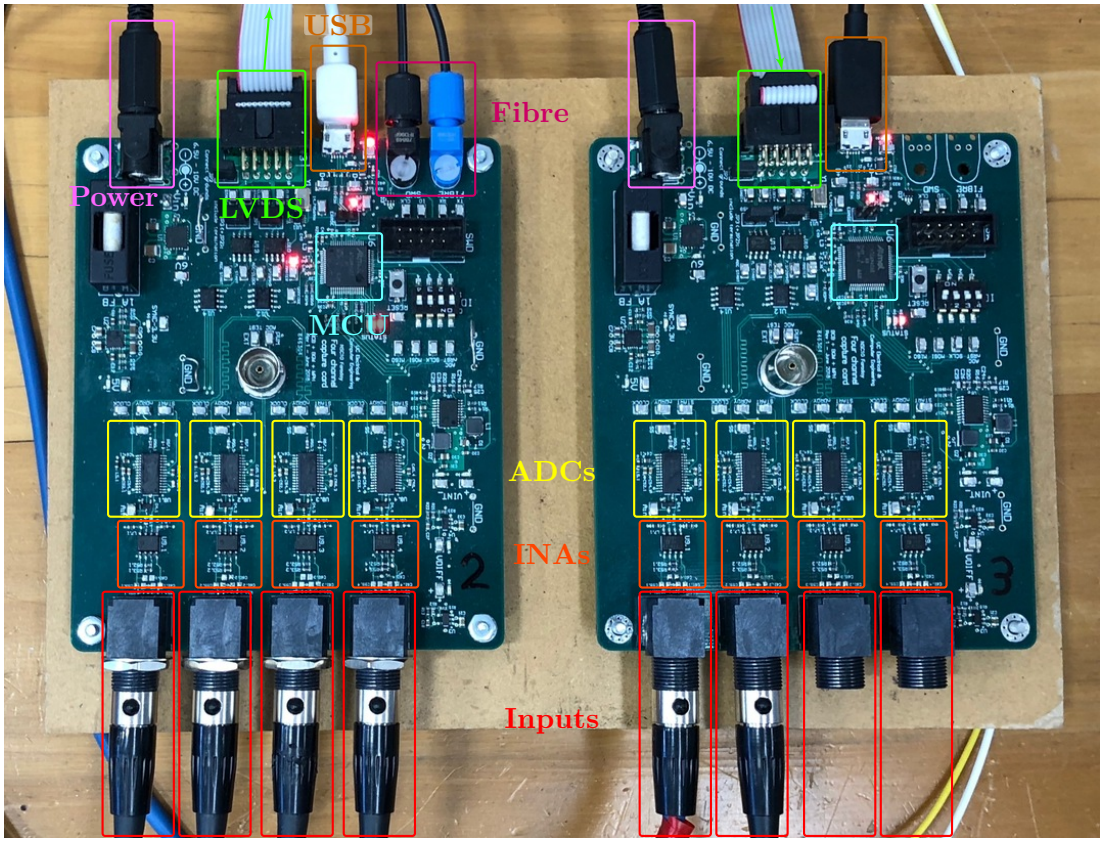

Figure 4.3 Two capture card PCBs with the major blocks labelled. The input cables are shielded twisted pairs.

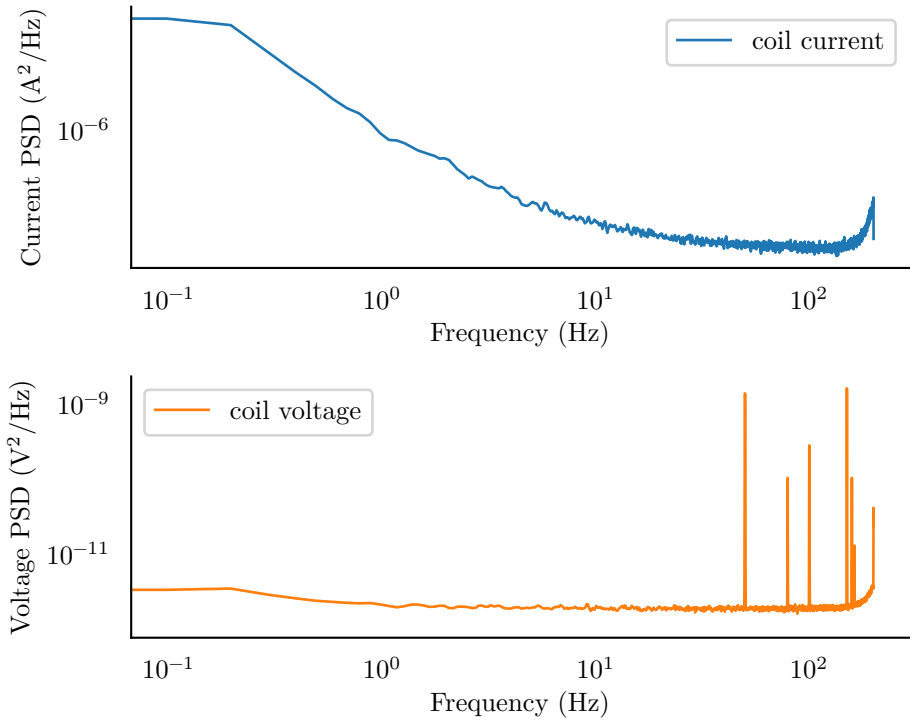

Figure 4.4 PSD of the noise for the coil current and voltage sensors. The spikes in the voltage spectrum are due to 50 Hz mains interference and an 80 Hz signal of unknown origin.

4.2 ELECTRODE AND SOURCE MODELLING

The instrumentation measures the voltage across a pair of electrodes embedded in the flowmeter. In a typical industrial pipe flowmeter these are embedded in the walls perpendicular to the magnetic field. In the cases of both the mini-aquifer and rolling gantry experiment rigs, the electrodes are positioned above/below the coil in the middle of the measurement volume and separated horizontally by 800 mm. Scott and Single [2014] and Jones and Scott [2015] have shown that a mesh of resistances is a suitable model for the bulk electrolyte with a complex electrode-electrolyte interface model, usually containing a constant-phase element (CPE), for the electrode connections. Figure 4.5 shows a circuit diagram of this model with the addition of some source terms representing the generated flow signal as the water moves through the magnetic field. The mesh of source/resistance terms can be reduced to the Thévenin equivalent shown in Figure 4.6. For the mini-aquifer rig, impedance measurements across the electrodes *and* the source are shown in Figure 4.8 for Ag/AgCl and Cu electrodes respectively.

A common model for electrode interfaces, the electrode tissue interface (ETI), is described by Magin and Ovadia [2008] using a CPE. The model is shown in Figure 4.7a. Luo et al. [2020] have modelled their bespoke Ag/AgCl electrodes using a combination of resistors and CPEs as shown in Figure 4.7b. The copper electrodes shown in Figure 4.8a

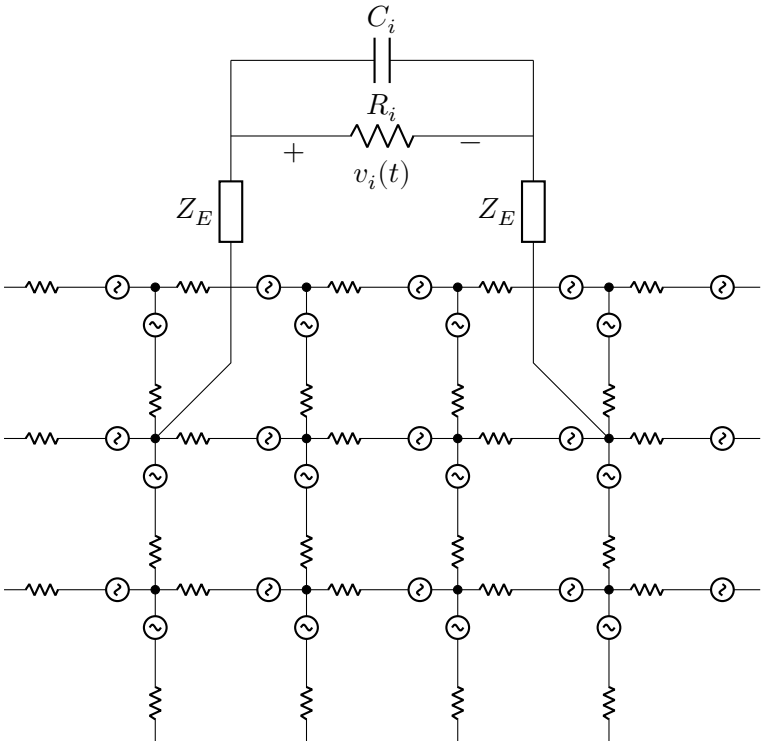

Figure 4.5 Source model for the instrumentation input. The water is modelled as a large mesh of small resistive paths with sources. Each source is a function of position and is proportional to the local magnetic field flux and water velocity, $v_s(x) \propto \nabla(\mathbf{u} \times \mathbf{B})$. The two electrodes are modelled by the complex impedance, Z_E. R_i is the input resistance of the instrumentation which is set to 2 MΩ and C_i is the capacitance of the instrumentation and input cabling.

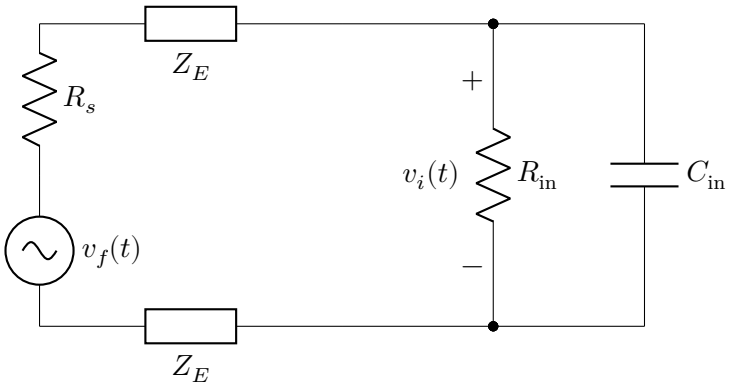

Figure 4.6 Simplified source model for the instrumentation input. The mesh of source resistances and voltages has been condensed to a single resistance, R_s, and voltage, $v_f(t)$, representing the effective source resistance between the electrodes as well as the flow signal generated by the moving water.

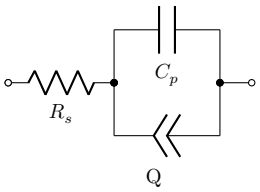

(a) ETI model as presented by Magin and Ovadia [2008].

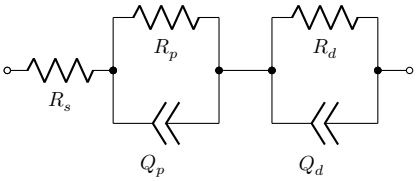

(b) Model reported by Luo et al. [2020].

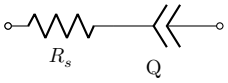

(c) Model for the copper electrodes.

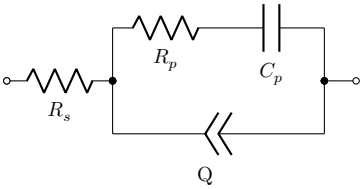

(d) Model for the silver-silver chloride electrodes.

Figure 4.7 Collection of various electrode electrolyte interface circuit models.

are best fit using a simplified version of the ETI model, shown in Figure 4.7c with $R_s = 2.1\,\text{k}\Omega$, and $Z_Q = 9.3 \times 10^3 \times (\text{j}\omega)^{-0.63}$. The closest fit for the silver/silver chloride electrodes, shown in Figure 4.8b, is a modified version of the ETI model shown in Figure 4.7d with $R_s = -2.2\,\text{k}\Omega$, $Z_Q = 17.2 \times 10^3 \times (\text{j}\omega)^{-0.012}$, $R_p = -626\,\text{k}\Omega$, and $C_p = -14.2\,\text{nF}$.

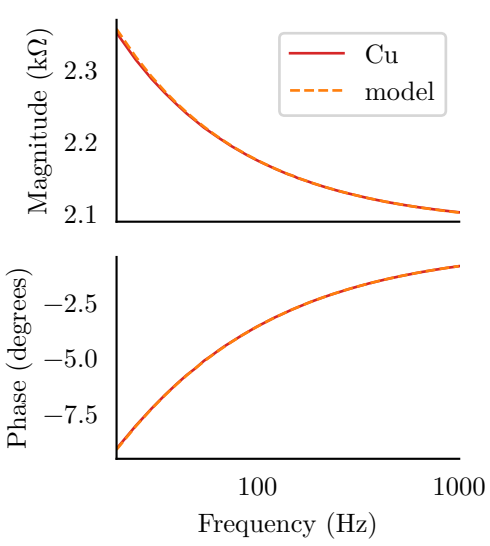

(a) Copper (Cu) electrodes.

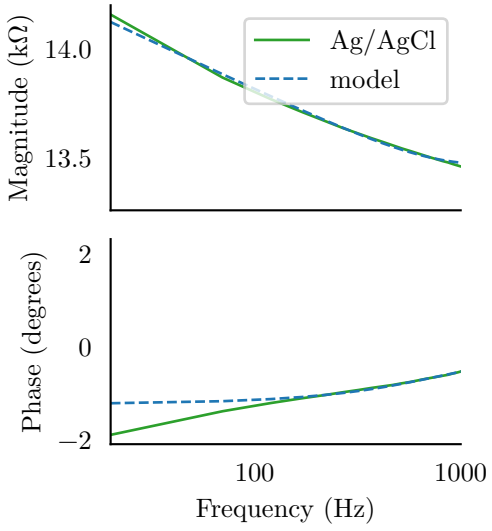

(b) Sintered silver-silver chloride (Ag/AgCl) electrodes.

Figure 4.8 Source impedance of the aquifer tank with common electrode types from 20 Hz to 1 kHz.

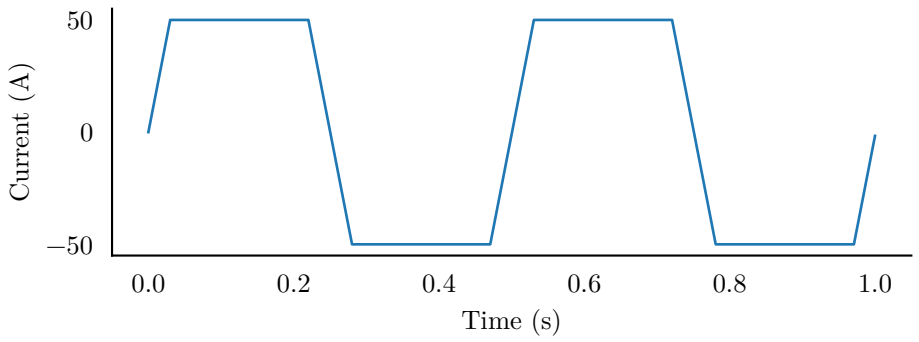

Figure 4.9 Plot of an idealised 50 A trapezoidal current waveform. A constant steady state current ensures no capacitively or inductively coupled interference. Assuming the current transition time from one polarity to the other is a constant, the frequency can be varied by reducing the steady state time.

4.3 MAGNETIC EXCITATION

A key component of the electromagnetic flowmeter is the magnetic field, as it enables the induction of the measurable flow signal. Typically the flowmeter system is designed so that the electrodes, the water flow (**u**), and the magnetic field (**B**) are all orthogonal. Ideally the magnetic field magnitude is a square wave to remove any interference as discussed in Chapter 3. However, the best real-world approximation is a trapezoid such as that shown in Figure 4.9. This is due to the two conflicting requirements in that a steady magnetic field allows the flow signal to be measured with no interference, but an alternating signal is required to to cancel out the baseline drift offset. The magnetic field should be designed to produce a constant weight vector, **W**, over the volume of the flow measurement so that the resulting measurement is independent of the water's velocity profile [Bevir 1970]. However, in practice, this is difficult to achieve.

Powering the excitation coil described in Section 2.1 is the bespoke bipolar DC power supply shown in Figure 4.10. This supply is designed to generate ±50 A trapezoidal current waveforms through the pancake coil [Heffernan et al. 2020]. The power supply makes use of two separate DC supplies running at approximately 40 V and 4 V to provide fast switching magnetisation and then to hold the current steady respectively. Figure 4.11 shows the typical current waveform during an experiment. Figure 4.12 also shows a closer view of the steady state peaks from Figure 4.11. The power supply is controlled through a combination of an field programmable gate array (FPGA) and a microcontroller (MCU), shown in Figure 4.13, allowing for precise timings, control systems, and safety monitoring. The time constant of the coil, combined with the 44 V excitation voltage, determines the total switching time per cycle of 60 ms giving a maximum operating frequency (with no steady state time) of 16.7 Hz.

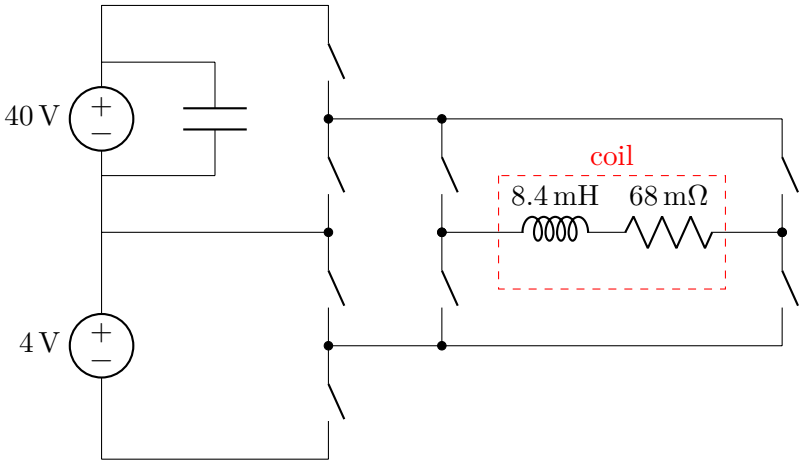

Figure 4.10 Simplified circuit diagram of the DC bipolar power supply from Heffernan et al. [2020]. The applied voltage can be switched between, 4 V, 40 V, and 44 V to energise the coil in either direction through the H-bridge. The 4 V supply is chosen to maintain the coil in a steady state of 50 A. The 44 V across both supplies is used to quickly magnetise the coil during a transition. When switching from positive to negative, the energy in the coil is dumped into the capacitor so it can be recycled for the next magnetisation. The coil is approximately modelled as an inductance of 8.4 mH in series with a resistance of 68 mΩ. However, due to the proximity effect, the impedance of the coil is more complicated resulting in a current overshoot and a slower settling time to steady state.

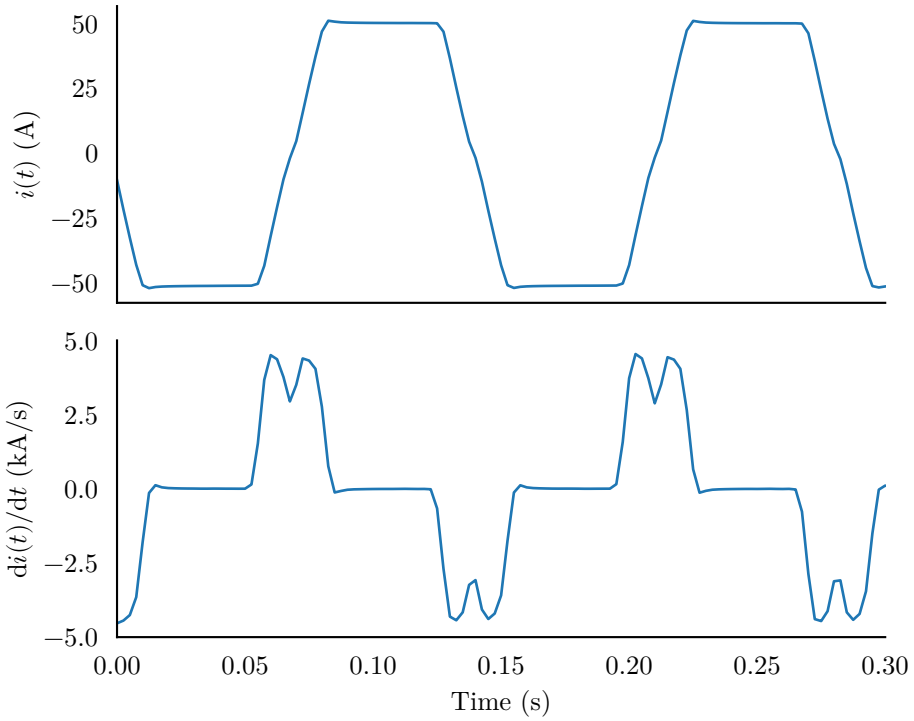

Figure 4.11 Typical current waveform from the bipolar DC power supply and its derivative. As a square wave would require infinite voltage spikes for the transitions, a trapezoid allows for a practical solution with controlled steady state and transition times.

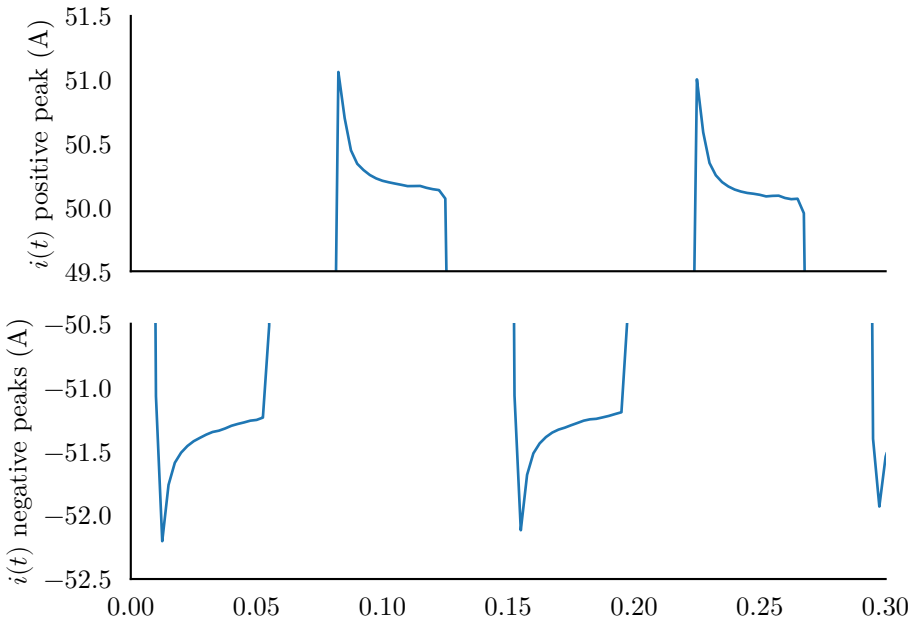

Figure 4.12 Steady state periods in the typical current waveform. The overshoot is caused by the complexities of the coils impedance. This is mostly due to the proximity effect and cannot be avoided. The current threshold for the transition can be adjusted, however, allowing for the tuning of the second half of the steady state period.

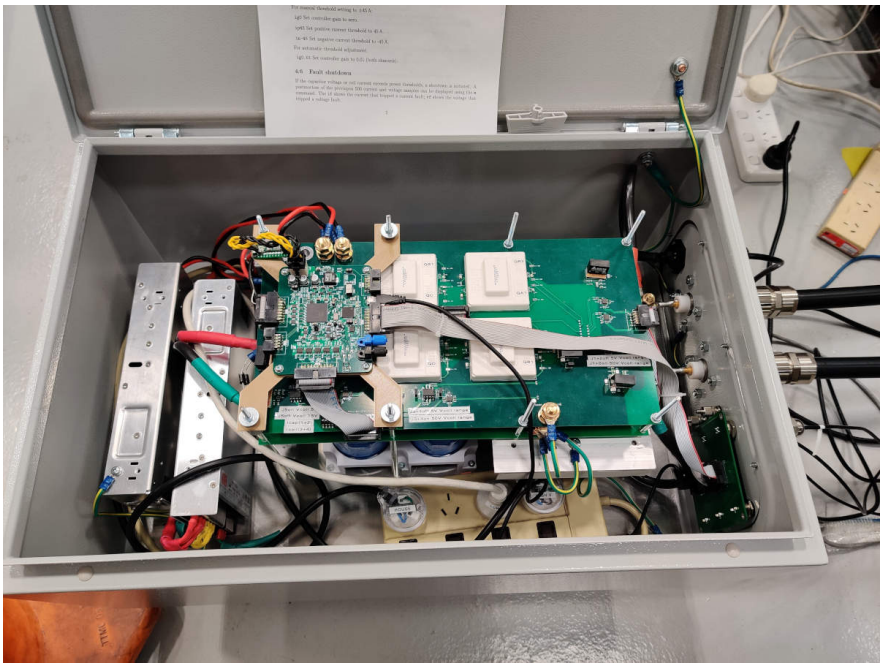

Figure 4.13 Photo of the custom power supply control hardware. On the left are the off-the-shelf DC power supplies, in the centre is the stack of PCBs which contain the power electronics, and the MCU and FPGA electronics on top. The (obscured) MOSFETs are bonded to the heatsink visible under the PCBs on the right side of the box.

4.4 MEASUREMENT LOOP TRANSFORMER TUNING

Due to the geometry of a measurement loop, required in every form of EMFM, there is an interference effect caused by the alternating magnetic flux passing through the measurement loop. This effect has been noted in all forms of EMFM that employ alternating magnetic fields. This interference is well understood and is modelled using Faraday's law,

$$v_{\text{transformer}}(t) = \frac{\mathrm{d}\Phi(t)}{\mathrm{d}t}\,, \tag{4.1}$$

where $\Phi(t)$ is the magnetic flux through the loop. With a constant measurement loop area, A, as is usually the case, (4.1) becomes

$$v_{\text{transformer}}(t) = A\frac{\mathrm{d}B(t)}{\mathrm{d}t}\,, \tag{4.2}$$

where $B(t)$ is the average magnetic field strength through the loop.

The amplitude of this interference depends on the excitation method. For AC flowmeters the amplitude varies with excitation frequency, whereas, for switched (or pulsed) DC flowmeters the amplitude varies with the slew rate of the excitation current. In both cases this transformer interference can easily exceed 1 V and either saturate the analogue instrumentation front-end or simply swamp the flow signal during signal processing. Using switched DC excitation allows for the measured signal to be sampled during relatively steady state regions of the waveform and effectively ignore the interference at the cost of a reduced sample count.

An alternative solution is to attempt cancellation of the interference signal. The introduction of a controllable loop area into the measurement loop effectively allows for the interference to be cancelled. This second loop can be modelled as

$$v'_{\text{transformer}}(t) = A\frac{\mathrm{d}B(t)}{\mathrm{d}t} - C\frac{\mathrm{d}B(t)}{\mathrm{d}t}\,, \tag{4.3}$$

$$= (A-C)\frac{\mathrm{d}B(t)}{\mathrm{d}t}\,, \tag{4.4}$$

where C is the loop area of a second nulling coil in series with the main measurement loop. This nulling coil could be implemented a number of ways such as: expanding or contracting the circumference of a loop, rotating a loop such as to increase or decrease its sectional area as seen by the magnetic field, or changing the number of loops in a stationary coil using switches.

Figures 4.14a and 4.14b show photos of an implementation of the nulling method using a changing number of loops. Two coil formers, both with 1024 turns of wire, are split up into coils with powers-of-2 turns. These loops, through a series of switches, can be connected in series or bypassed allowing the turns-area product to be changed

(a) Photo of the nulling box with lid on. The two knobs allows the operating mode to be changed and the nulling amount to be manually dialled in.

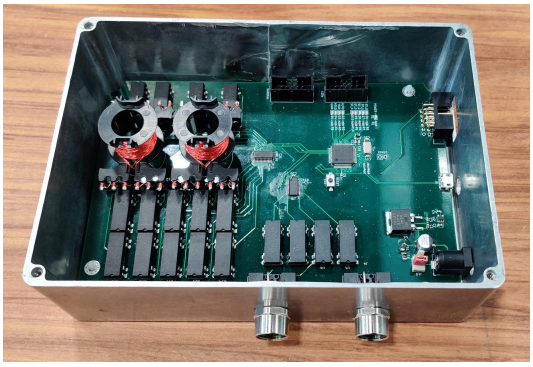

(b) Internals of the nulling box. The two coil formers on the left hold the complement of loop. Around the coils are reed relays that allow each individual coil to be connected in series or bypassed.

Figure 4.14 Photos of the flux nulling box.

dynamically. A further pair of switches allows the polarity of the entire setup to be reversed allowing for a series or series-opposition connection. The switches are driven by a microcontroller and can be manually controlled or automatically stepped through. Figure 4.15 shows the level of magnetic interference changing with time as the nulling circuit steps through its full range. The interference decreases over time until the optimal point is reached, at which point the magnitude starts to increase again but with a reversed polarity. Figures 4.16 and 4.17 show the difference in the measured signal when the transformer interference is present from when it has been removed using the nulling box. These results show it is possible to reduce the transformer interference using a nulling method.

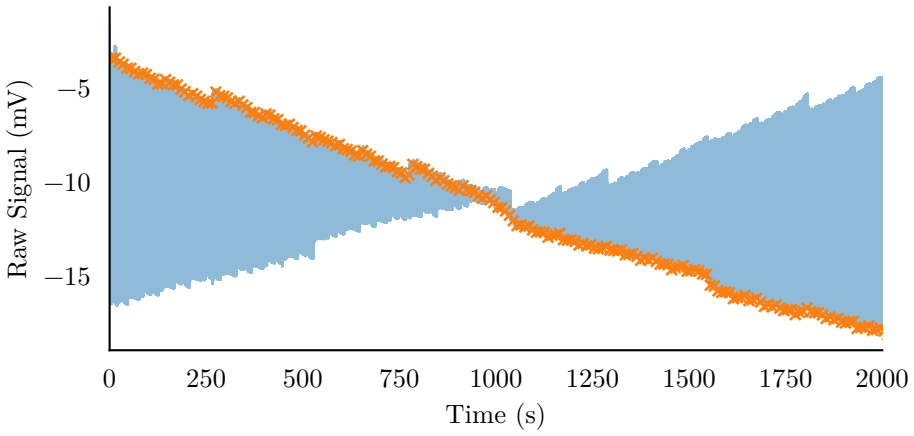

Figure 4.15 Plot of an interference scanning experiment. The nulling box was set to automatically cycle through its range in 10 s steps. Over the course of the experiment the amplitude of the magnetic interference reduced until the optimal nulling point where the amplitude increased again. The orange crosses indicate the amplitude of the interference fit and show how the signal reverses polarity after the optimal point.

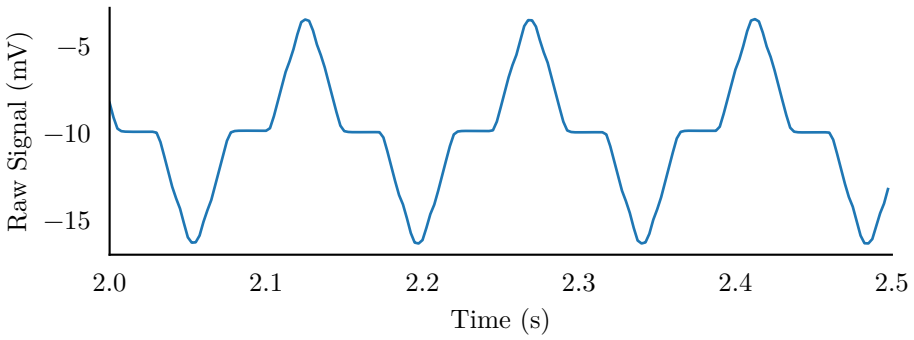

Figure 4.16 Section of the interference scan experiment with poor nulling. The spikes indicate the excitation current is switching from positive to negative or otherwise.

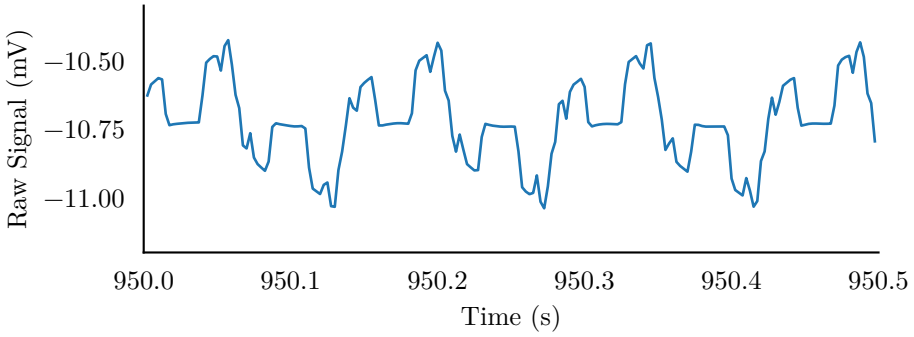

Figure 4.17 Section of the interference scan experiment with good nulling. The signal no longer contains the distinctive magnetic interference. Note the change in peak-to-peak amplitude compared to Figure 4.16 from 12 mV down to 0.6 mV.

Chapter 5

MINI-AQUIFER EXPERIMENTS

The first experimental setup used to verify the flowmeter operation was designed to mimic the flow of water through the ground. This chapter details the mini-aquifer rig, the experiments performed, and the results acquired.

5.1 TANK

The experiment tank, pictured in Figure 5.2, is 1.2 m × 2.1 m × 0.6 m and made from 23 mm thick acrylic. Appendix C.1 shows a plan view of the tank. It is separated into five sections: two opposed reservoirs, two main water tanks, and a baffle full of resistive sand separating them. Water can be pumped from one reservoir to the other using the Prisma 0280 stepper motor driven dosing pump shown in Figure 5.3. This pumping induces a head difference between the two reservoirs which drives a flow through the central baffle where the electrodes are located. The electromagnetic coil is positioned beneath the tank and projects a vertical magnetic field through the baffle.

5.1.1 Water levels

Darcy's law, (1.38), defines the flowrate through the system. Darcy's law relates the steady state head difference between the two tanks to the flow rate through the baffle, which is generated by the pumping equipment, as shown in Figure 5.4. In the lab setup, the permeability, k, viscosity, μ, and pressure gradient, ∇p are all constants (after the initial setup). The superficial water velocity, q, is given by

$$q = -\frac{k}{\mu}\nabla p\,, \tag{5.1}$$

where $\nabla p = \rho g \Delta h / L$ is the pressure gradient. The velocity of the individual water molecules is related to the superficial velocity by

$$u = \frac{q}{\varphi}\,, \tag{5.2}$$

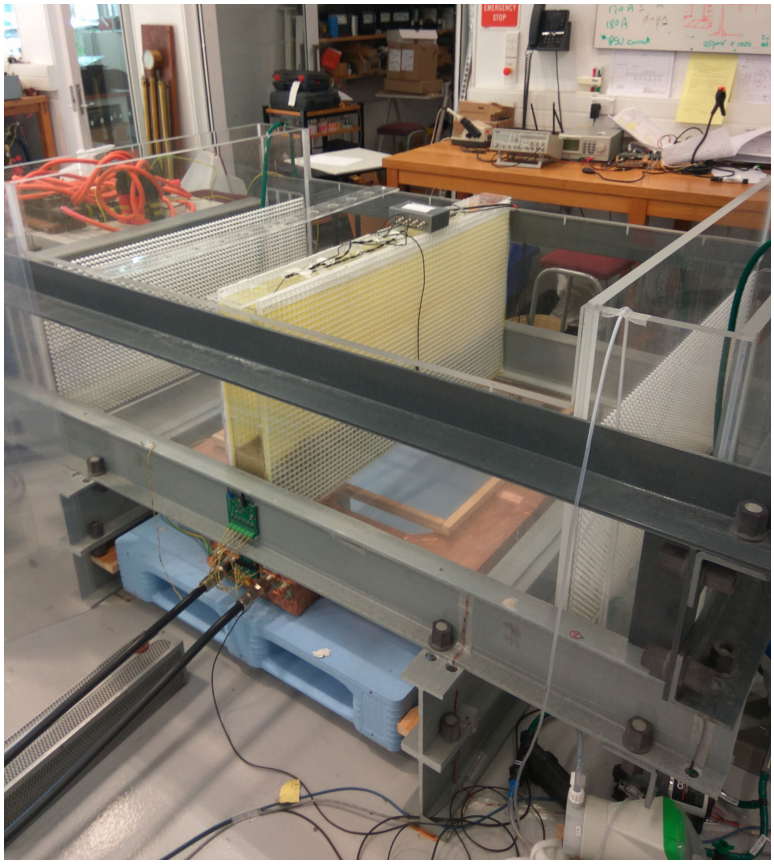

Figure 5.1 Photo of the test aquifer showing the lab setup. The yellow baffle in the centre is filled with a fine sand. The reservoirs at either end of the tank are filled with water and have their levels set to generate a flow through the baffle. Holes in the reservoir walls connect through to the main tank allowing the water to pass through. The water is then pumped from the low end back into the other reservoir by a pump shown in the bottom right of the photo. The coil is located underneath the the centre of the tank with the feed lines visible to the lower left. An 800 mm × 800 mm search coil is positions on top of the coil, visible as the wooden frame. The tank itself is made from acrylic and supported by a frame made from pulltruded fibreglass.

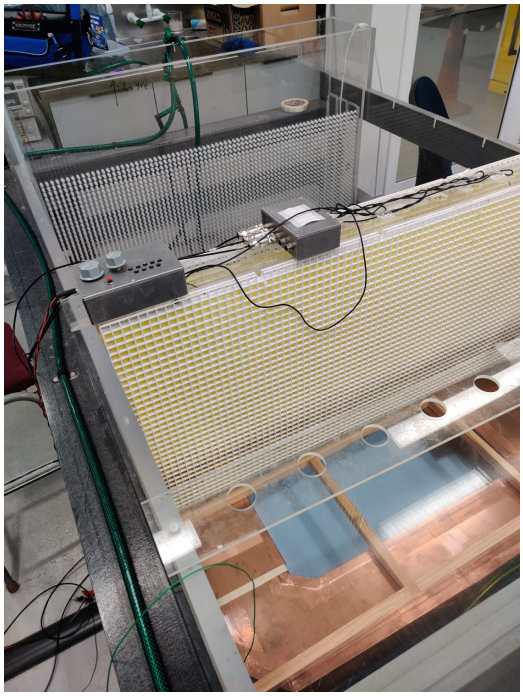

Figure 5.2 Photo of the experiment tank, showing the two main tanks, the baffle, and one of the end reservoirs in the top left. On top of the baffle are the variable turn coil on the left, and the electrode junction box in the centre.

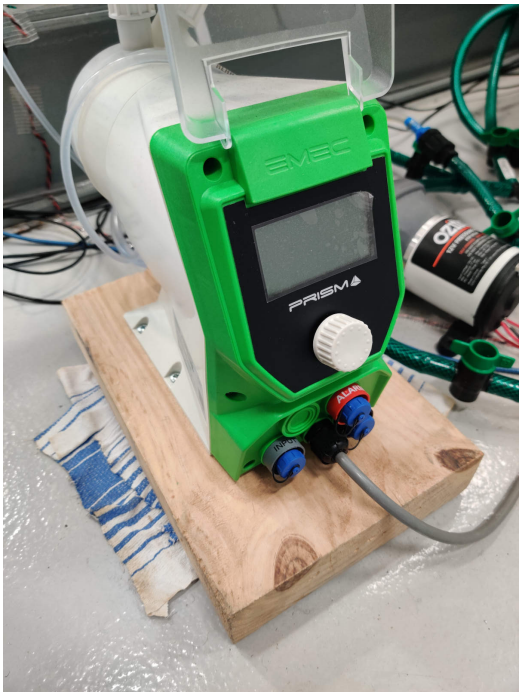

Figure 5.3 Photo of the Prisma 0280 dosing pump used to generate the head pressure. In the background the network of hoses can be seen that allow the water to be moved from either end of the tank to the other.

where u is the water velocity and φ is the porosity of the baffle material. The difference between the superficial velocity, q, and the velocity, u, is due to the presence of the baffle material. For the moving fluid to achieve the same discharge rate, it must travel faster through the smaller spaces than it would if there were no sand present.

The electromagnetic flowmeter method measures the water velocity, u, which is controlled by the head difference, Δh. An important aspect to consider is that it takes time for a pump to build up to the steady state head difference, which is to say, the flow rate through the pump and the flow rate through the baffle are not always equal. Figure 5.5 shows how long it can take for the water levels, and thus the flow speed, to stabilise to the steady-state values. It is critical that the head difference is controlled over the course of an experiment. An equivalent electrical circuit of the aquifer tank is shown in Figure 5.6. The two reservoirs act like large capacitors for the water while the baffle between them acts as a resistor. The resistance of the baffle is inversely proportional to its wetted area which is a function of water height.

5.1.2 Baffle materials

The selection of baffle filler material directly affects the expected flow measurement, as well as the distribution of water velocity through the baffle. Ideally, the filler material

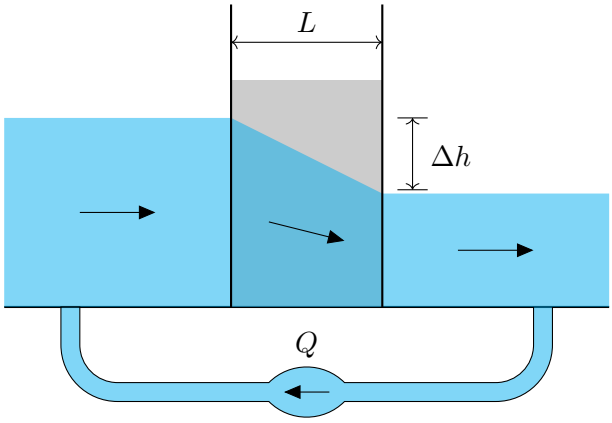

Figure 5.4 Diagram of the water levels during a flow experiment. The water is pumped from the right tank to the left and allowed to filter through the baffle to complete the loop. The head difference, Δh, is proportional to the flowrate generated by the pump and the hydraulic conductivity of the baffle medium.

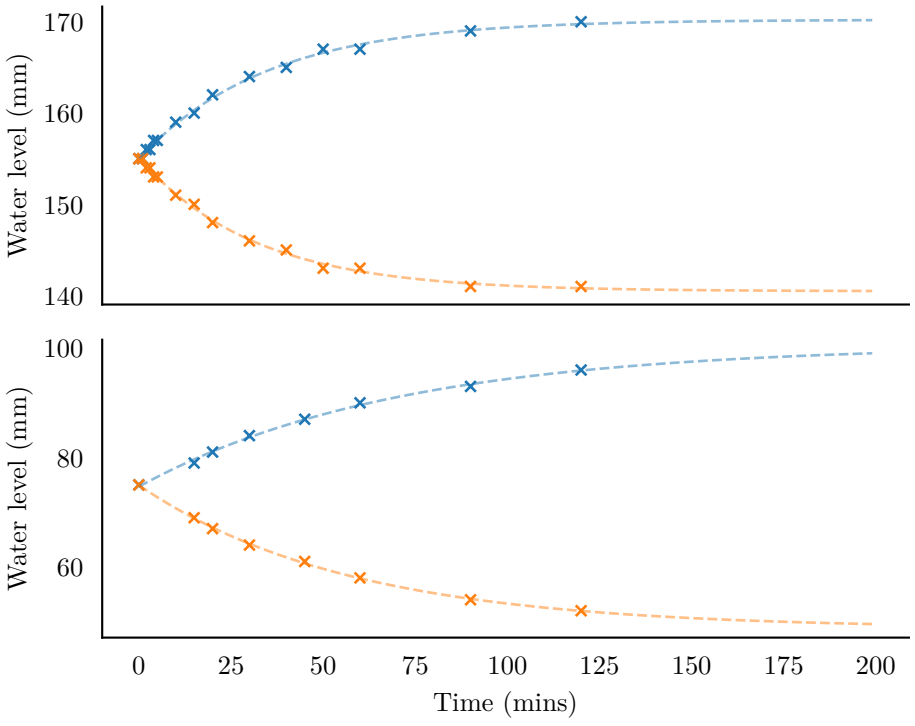

Figure 5.5 Plot of two experiments showing the water levels in the two tanks over time after the pump is activated. The top plot starts at 155 mm depth and the pump is set to 500 ml/ min. The bottom plot starts at 75 mm depth with the pump set at 250 ml/ min. The blue series track the water level for the filling tank while the orange series track the draining tank. The difference between the blue and orange is the head difference. The fitted models are of the form $A \pm Be^{-t/\tau}$ where τ is a function of hydraulic conductivity and wetted area, and have time constants of ≈ 33 and ≈ 62 minutes respectively.

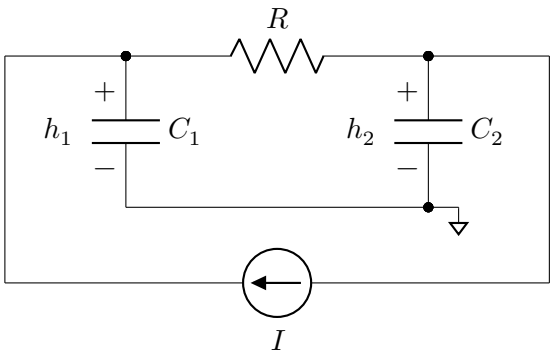

Figure 5.6 Equivalent electrical circuit for the aquifer tank water flow. The baffle is modelled as a resistor between the two capacitive tanks where the resistance is inversely proportional to the water level. The pump acts as a constant current source moving water from one tank to the other.

should be homogeneous in terms of permeability and porosity. For the experiments detailed in this thesis, filtered foundry sand with a grain size of 300 µm was used, with a hydraulic permeability of $2 \times 10^{-6}\,\mathrm{m}^2$ and a porosity of 0.068 (6.8%). In real world scenarios, the ground will likely be heterogeneous with possible unknown formations of clay, rock, shale, gravel, sand, buried tractors, and other geological features.

5.2 EXPERIMENTS

A number of experiments were performed using the aquifer tank rig at 1 Hz and 7 Hz excitation.[1] The water flow induced in the tank has a maximum velocity of $0.71\,\mathrm{mm\,s^{-1}}$ for which the simulations in Chapter 2 predict a flow signal of 1.1 µV. Prior to each measurement, the magnetic field nulling (as described in Section 4.4) was tuned manually to reduce the interference as much as possible. All of the results were processed in the following manner:

1. Apply a mains filter to the input signals.
2. Calculate the basis functions for fitting.
3. Apply pre-whitening to the input and basis functions (if used).
4. Split the recorded signal into 30 s chunks.
5. For each 30 s chunk:
   (a) Gate out the interference (if used).
   (b) Estimate the model parameters.
   (c) Estimate the flow signal from the model.

[1]The experiments performed at 7 Hz were designed to reduce the $1/f$ interference and improve the SNR prior to understanding the frequency dependence demonstrated in Section 3.11 and Section 6.3.

Figure 5.7 shows the results of a 1 Hz experiment performed at three flow speeds. The time average of the gated results does follow the input velocity, however, the deviation of these results is larger than the difference from one flow to another. There is also a DC offset present causing an incorrect zero flow measurement.

Figures 5.8 and 5.9 show results from two five speed experiments performed with 7 Hz excitation. These results show an abundance of noise swamping any plausible signal. Removing the gating filter reduces the noise of the estimates as there are now more samples to average, however, these results still show no correlation with the input velocity.

Figures 5.10 and 5.11 show results without using the magnetic field nulling equipment. These show a strong correlation with the flow speed, producing signals 140× greater than predicted. This is due to the presence of the large magnetic interference signals, shown in Figure 5.12, which are caused by the changing measurement loop area which is a function of the head difference across the baffle and thus also the flow velocity. The parameter estimation is unable to exclude all of the interference signal and a small portion manifests in the flow signal estimate. This would make for a good flowmeter, except, there is a zero offset present due to the alignment of the measurement loop as shown in Figure 5.11. Removal of the gating filter reduces the estimate amplitudes to physically plausible levels for the flow signal and in the case of Figure 5.11, producing consistent estimates. However, these results, like Figures 5.8 and 5.9, still show little correlation with the input velocity.

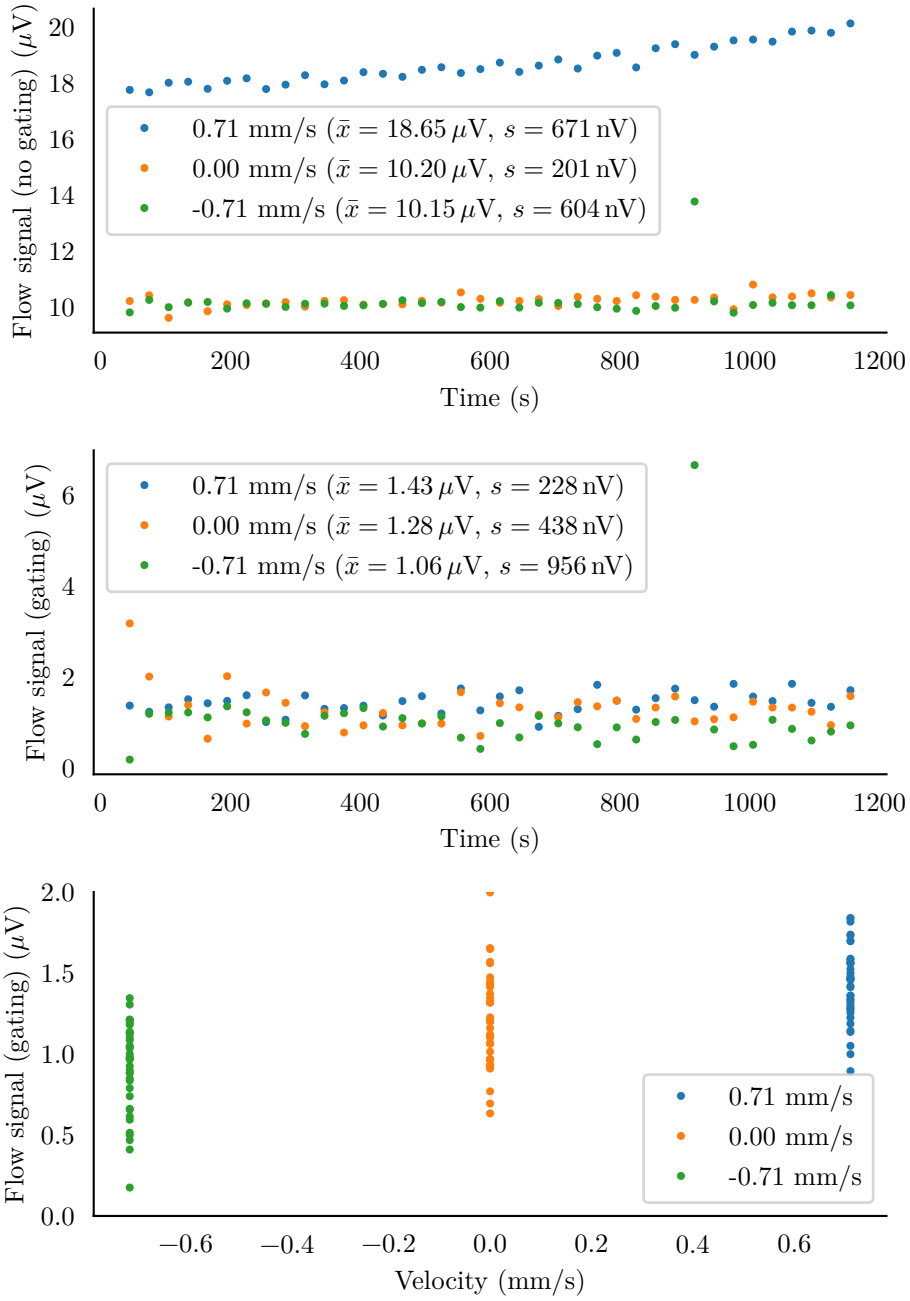

Figure 5.7 Results from a three speed, aquifer tank experiments at 1 Hz. Prewhitening is applied to all results. The expected flow signal for this experiment is 1.1 µV for 0.71 mm s^{-1}.

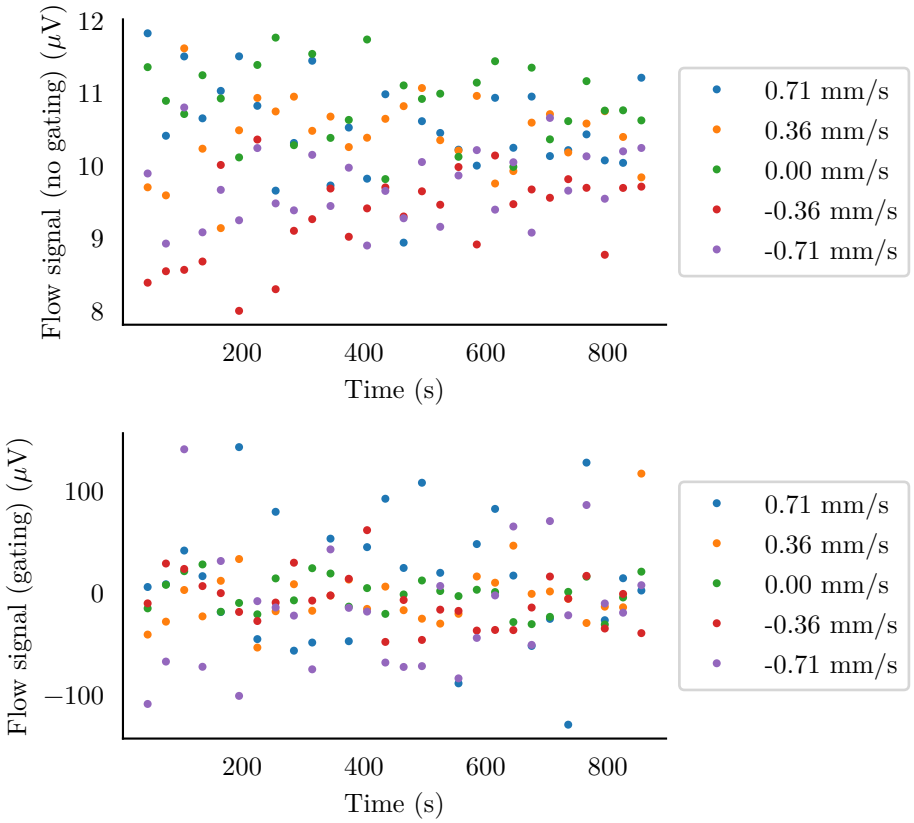

Figure 5.8 Results from a five speed, aquifer tank experiment at 7 Hz. The results show only random noise.

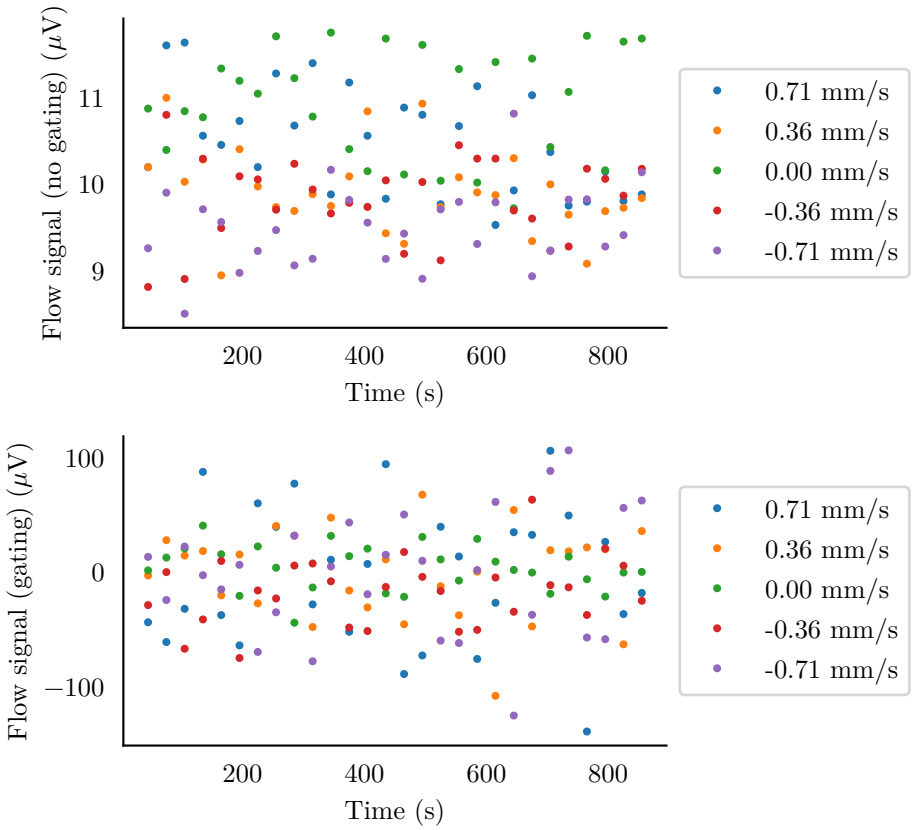

Figure 5.9 Results from a second five speed, aquifer tank experiment at 7 Hz. These results are similar to Figure 5.8 in that they only show random noise.

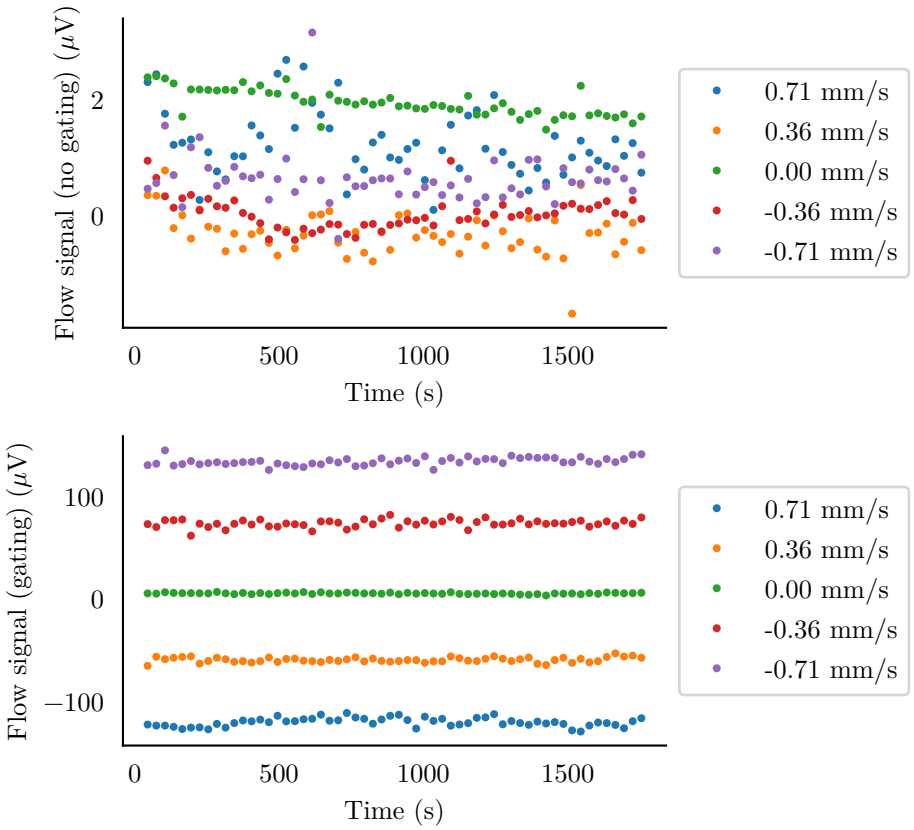

Figure 5.10 Results from a five speed, aquifer tank experiment at 7 Hz without magnetic field nulling. Note the magnitude is approximately 100–150× the expected value.

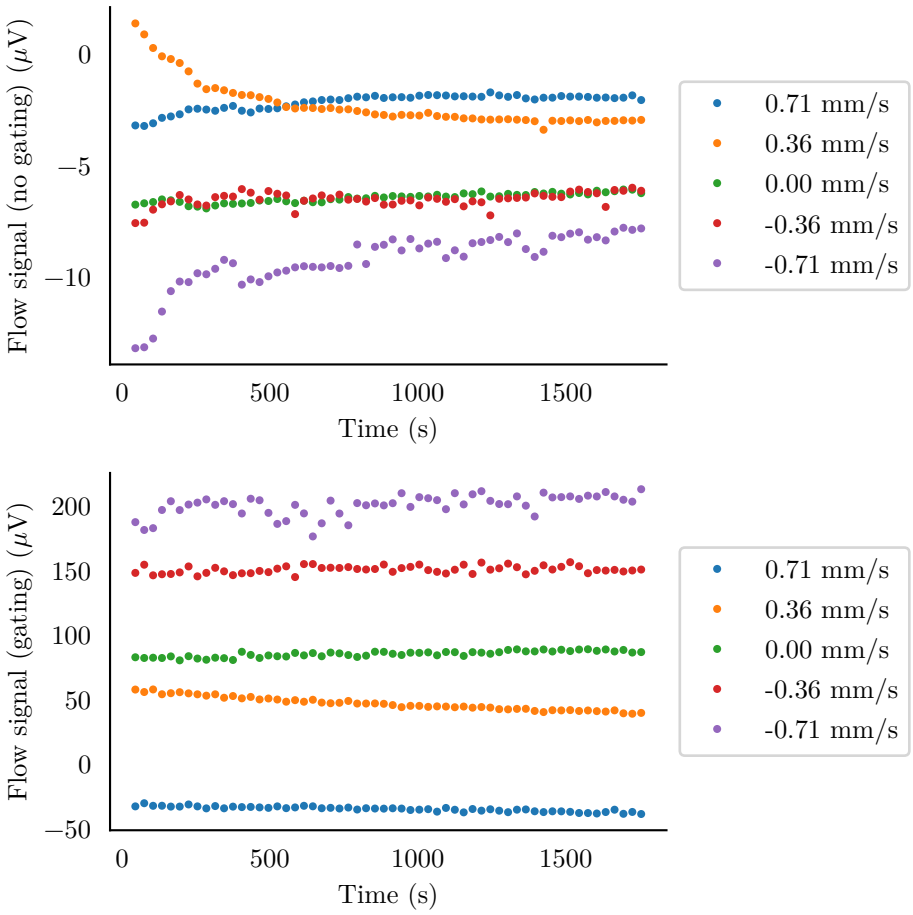

Figure 5.11 Results from a second five speed, aquifer tank experiment at 7 Hz without magnetic field nulling. Note the magnitude is again approximately 140× the expected value and there is a large zero offset value. The moving trace, especially in the orange case, is due to the water levels stabilising over the course of the experiment causing the velocity and thus magnetic interference to change with time.

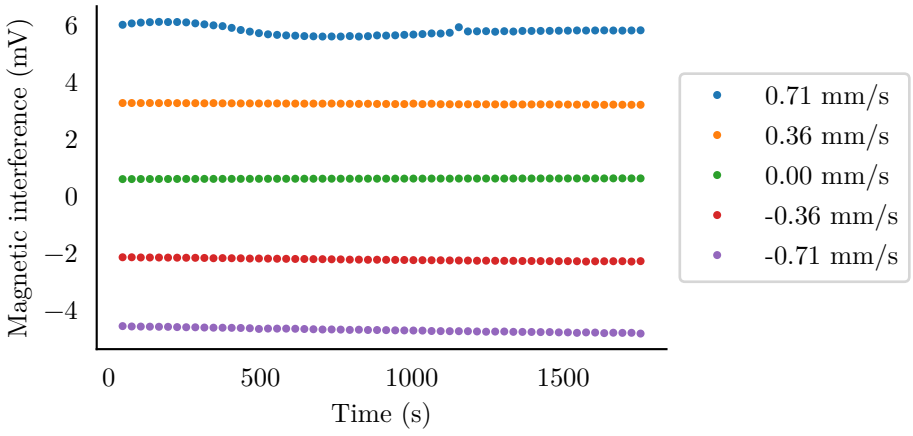

Figure 5.12 Amplitude of the magnetic interference during the 7 Hz experiment shown in Figure 5.10.

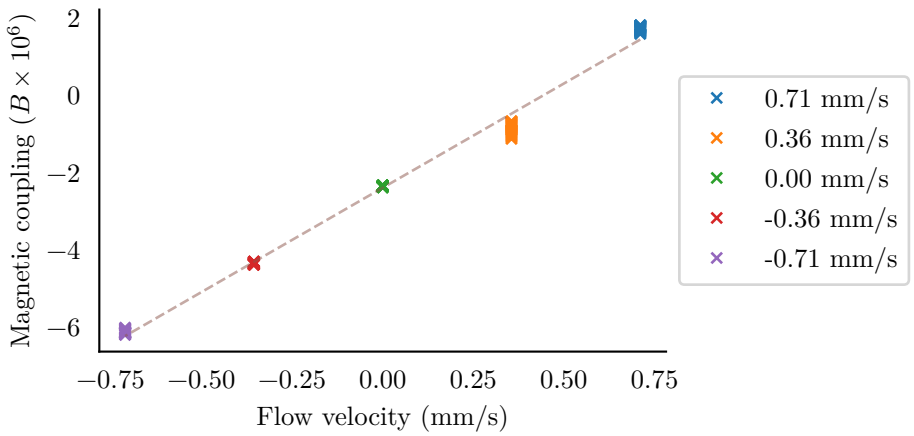

Figure 5.13 Magnitude of the magnetic interference during a 7 Hz flow experiment over different velocities. The results fit a linear trend except for 0.36 mm s^{-1} which is attributed to the head difference equilibriating during the experiment.

5.3 MEASUREMENT LOOP BENDING

A further complication for the aquifer rig is that the geometry of the measurement loop must remain constant to keep the magnetic interference constant. However, measurements in the mini-aquifer rig, Figure 5.13, show that the magnetic interference changes as a function of water velocity. Given the consistent magnetic excitation used between the experiments, there must be a change in the measurement loop area. For the mechanical components of the loop: the electrodes, wiring, and connections to the instrumentation, this is a relatively simple problem as they can be fixed in place and use twisted pair wiring to reduce excess loop area.

The remaining section of the measurement loop is composed of a myriad of conductive paths through the water. Ordinarily this would have no effect, except when the relative conductivity of the water changes. An example of this is when the head difference between the two flow reservoirs is non-zero, as pitcured in Figure 5.14. In the diagram, the tank on the left has a larger volume of water, and is a lower impedance path between the electrodes than the tank on the right. This results in the average current path between the electrodes 'bending' to the left. With an experimental rig configured in this way, the magnetic interference component will be a function of the flow speed as is the case in Figure 5.13.

5.3.1 Experiment

An experiment was designed to further test this hypothetical relationship: set up the aquifer tank with completely stationary water (no head difference), and then introduce an electrical insulator to restrict the current paths on one side of the tank. Figure 5.15 shows a diagram of this experiment. A plastic panel is introduced and moved through

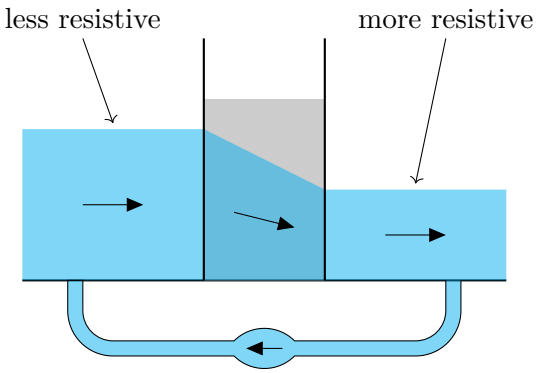

Figure 5.14 Diagram of the head difference between the two halves of the experiment tank. For current flowing between two electrodes embedded in the sand, the left tank has more conductive material and thus a lower resistance than the right tank. This results in the current path between the electrodes bending and thus the magnetic interference being a function of the flow speed.

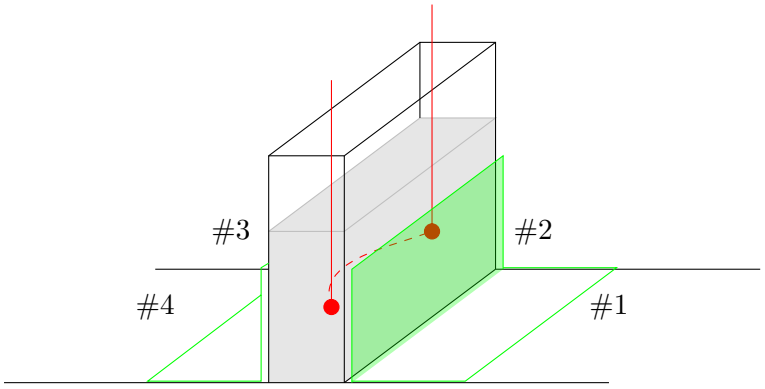

Figure 5.15 Diagram of the bending measurement loop experiment. The tank is filled with stationary water. The excitation coil is running and the magnetic interference is measured. A panel of insulating plastic is then moved through positions #1 – #4.

positions #1 to #4. The panel, in positions #2 and #3, should restrict the current paths on one side of the tank, making the other side more conductive as if there were a head difference. Positions #1 and #4 are included to ensure that the presence of the panel is not a factor in the results, as they should have no effect on the current paths. A further test is performed with no panel present for control.

5.3.2 Results and implications

The results from the experiment are shown in Figure 5.16. The constant readings indicate a consistent estimation of the interference signal. The three tests which should have no impact on the interference, #0, #1, and #4, are clustered at -2.5×10^{-6}. The two tests which should affect the interference, #2 and #3, are equally displaced around the centre with values of 9×10^{-6} and -14.5×10^{-6}. These results show that bending the average current path will change the magnetic interference coupling parameter by changing the cross-sectional loop area.

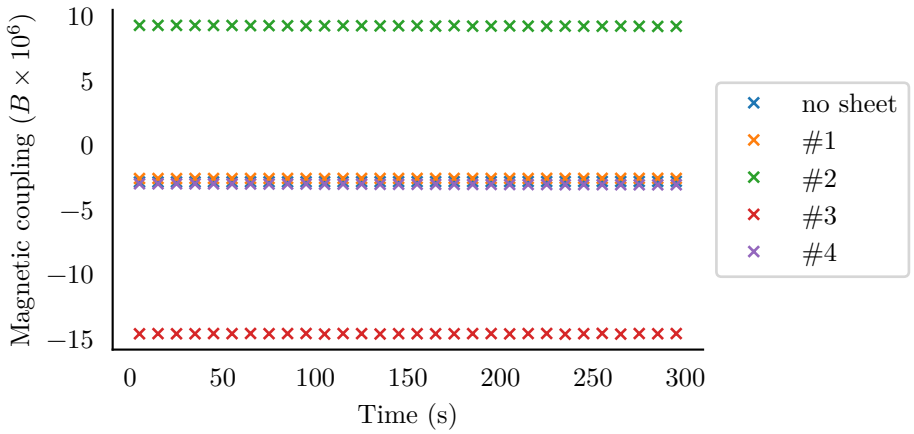

Figure 5.16 Plot of the magnetic field coupling estimation over time for each of the different positions. Positions #1, #4, and no sheet all show a minimal amount of interference indicating the measurement loop is almost properly aligned. Positions #2, and #3 are spaced evenly apart from the central reading with opposite magnitudes.

The implications of this bending are apparent when taking the signal processing into account. In perfect conditions, the signal processing can accurately filter out the magnetic interference and determine the flow signal. However, in practice it is never that simple. Due to noise, or incomplete modelling, the magnetic interference cannot be perfectly accounted for by the estimator. Any errors from fitting the interference are essentially included with the flow signals estimation. Given the magnitude of the interference signal, in the order of 10 mV, any small error in fitting can result in a significant 'pollution' the flow signal estimate which is in the order of 1 µV. As the magnitude of the interference is also a function of velocity, the flow signal and this crossover pollution become indistinguishable. The poor quality results shown in Section 5.2 are attributed to this effect.

Chapter 6

ROLLING GANTRY EXPERIMENTS

A second experiment rig was designed to mitigate the issues presented by the measurement loop bending described in Section 5.3. This alternative rig was set up with the excitation coil and electrodes mounted to a rolling gantry that can move horizontally above a water tank. The gantry rig, pictured in Figure 6.1, is designed to ensure there is no head difference across the electrodes and that the water flow is homogeneous by moving the coil and electrodes instead of water.

6.1 GANTRY RIG

The gantry rig is designed such that the excitation coil and electrodes are moved instead of the water. This has the advantage of allowing all of the water to remain in a constant steady state while the gantry (with the coil and electrodes) can be moved in a precisely controlled manner. Figure 6.1 shows the rig as a whole and Figure 6.2 shows a close up of an electrode in the water. The pool of water measures $0.9\,\mathrm{m} \times 2.3\,\mathrm{m}$ with a depth of $0.2\,\mathrm{m}$. The gantry can travel a maximum distance of $1\,\mathrm{m}$ along the length of the pool. Appendix C.2 shows a plan view of the gantry rig. Figure 6.3 shows the AC motor which is geared down through a 100:1 reduction gearbox and the worm gear which has a thread pitch of $2.54\,\mathrm{mm}$. The AC motor is driven by a variable frequency inverter allowing motor speed control. The gantry has a maximum speed of $36\,\mathrm{mm\,min^{-1}}$ ($600\,\mu\mathrm{m\,s^{-1}}$) and a minimum speed of $120\,\mathrm{mm\,h^{-1}}$ ($34.7\,\mu\mathrm{m\,s^{-1}}$).

6.2 MEASUREMENT LOOP BENDING

The measurement loop bending discussed in Section 5.3 also applies to the gantry rig, albiet in a different manner. Instead of the magnetic interference amplitude being a function of velocity as in the aquifer rig, it is a function of position for the gantry rig. This is because the volume of water on either side of the measurement loop is a function of where the loop is in the tank, shown in Figure 6.4, rather than how fast the coil is moving. The measured magnetic interference is demonstrated in the results shown in Figures 6.5 and 6.6.

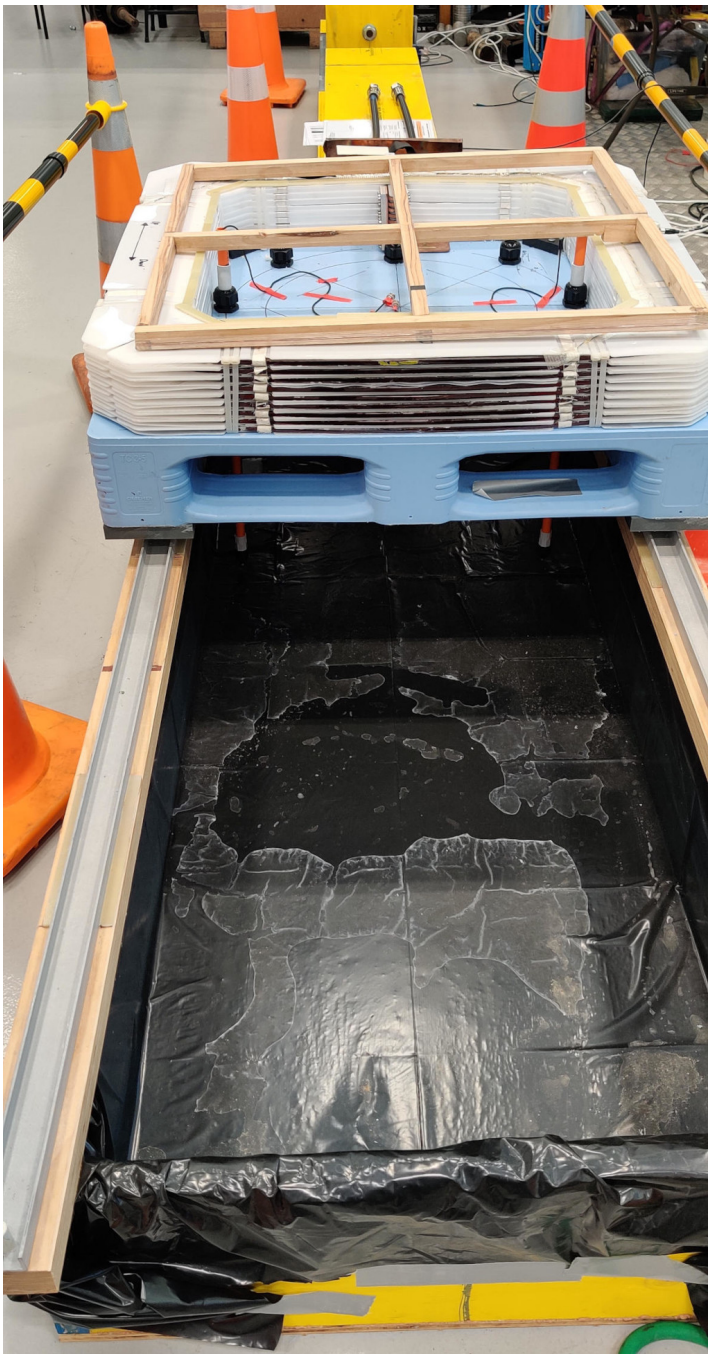

Figure 6.1 Photo of the gantry equipment. The pancake coil and electrodes are mounted on roller bearings and can travel 1 m along the length of the pool inside the pool. The power supply is mounted to the far end of the rolling gantry with the feed lines extending along the direction of travel. The tips of the electrodes are visibly suspended beneath the pallet. The linear drive machinery is hidden behind the yellow panel at the top of the photo. The wooden frame resting on the pancake coil is a search coil used to measure the changing flux during experiments.

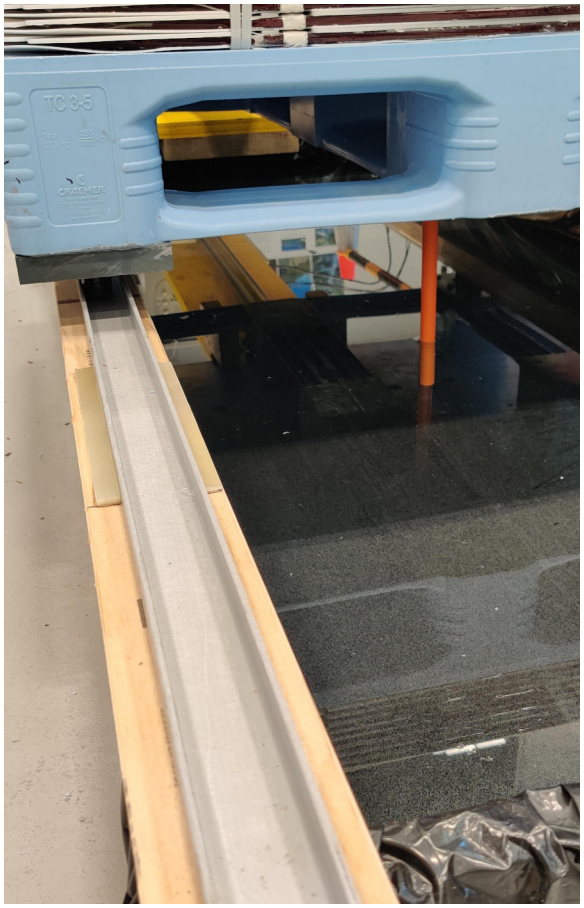

Figure 6.2 Close-up photo of the gantry rig showing an electrode holder suspended in water. At the tip is a Greentek D08H04 Ag/AgCl electrode.

Figure 6.3 Photo of the gantry drive equipment. The AC motor, shown here on the left, is coupled through a right angle, 100:1, reduction gearbox to a 1 m long worm gear with a thread pitch of 2.54 mm. The fibreglass tube, shown on the right, is coupled to the rolling gantry.

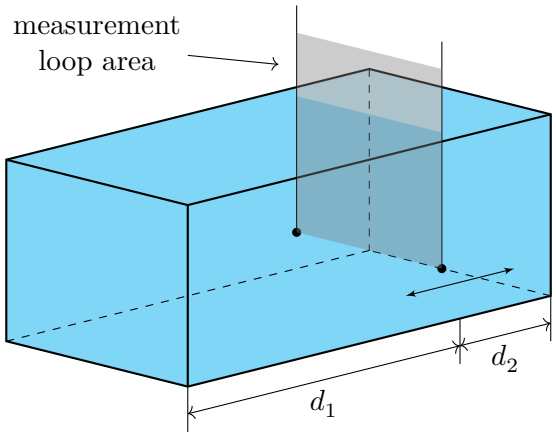

Figure 6.4 Diagram of the loop area in the moving gantry experiment. The electrodes are free to move up and down the length of the tank. In the scenario shown, $d_1 > d_2$ therefore there is a larger volume of water on the left side of the loop. As there is more conductivity, the measurement loop area will bend to the left side. This results in the magnetic interference amplitude being a function of d_1 and d_2.

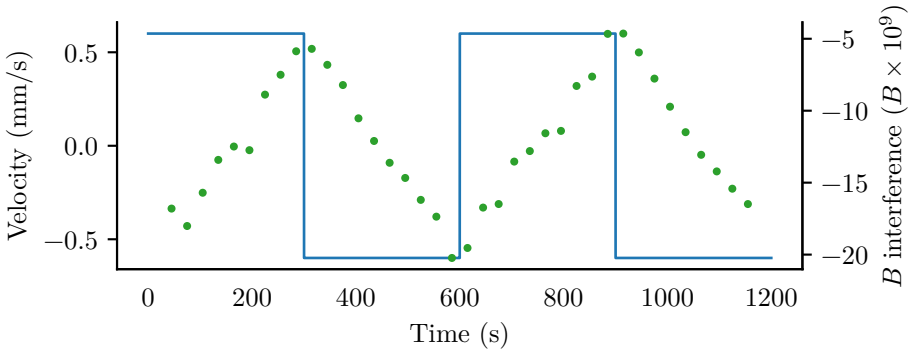

Figure 6.5 Plot of the magnetic interference component estimated using whitening and gating as the measurement loop moves through the tank. The interference appears to be an integral of the coil velocity. Note that in this experiment, the coil travel is only 180 mm and the interference coupling is non-linear further from the centre of the tank.

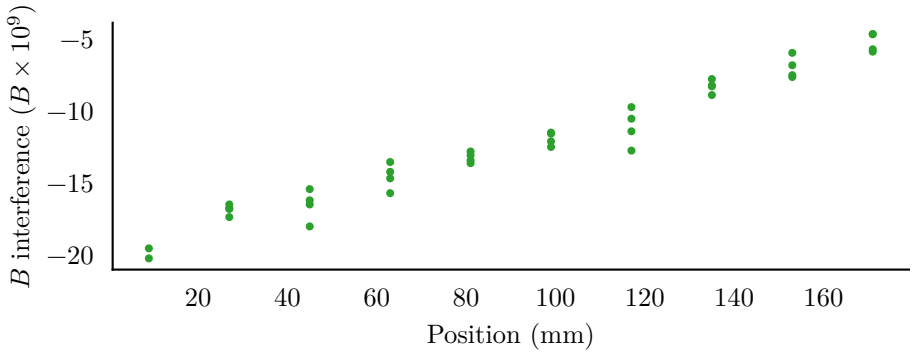

Figure 6.6 Plot of the magnetic interference component estimate as a function of the coil position.

6.3 ROLLING GANTRY EXPERIMENTS

Experiments were performed using the rolling gantry rig with excitation frequencies of 1 Hz, 4 Hz, and 7 Hz. These use the same processing procedure as the aquifer rig. The only difference between the two rigs is that the velocity can be easily modified during an experiment for the gantry rig. The simulations from Chapter 2 give these experiments an expected flow signal of 750 nV at the maximum speed of the gantry ($0.6\,\mathrm{mm\,s^{-1}}$).

Figures 6.7 and 6.8 show results from moving the gantry backwards and forwards over the pool of water at $0.6\,\mathrm{mm\,s^{-1}}$. The raw OLS fits from these experiments show a correlation with the input velocity, with a standard deviation of approximately 0.5 µV. The gating filter, which removes the transients from fitting, gives an increase in estimation deviation due to the fewer number of samples for averaging. The application of the whitening filter (changing to GLS instead of OLS) reduces the deviation of the estimates to the order of 0.05 µV. However, a DC offset is introduced, specifically in Figure 6.7 where the mean is approximately 0.5 µV. The estimated flow signal has a linear trend; the gradient of which correlates with the input velocity. Finally, the application of both the gating *and* whitening filters together removes the DC offset while maintaining the reduced standard deviation. The resultant signal shows a strong correlation with the input velocity.

Figures 6.9 to 6.11 show the results from experiments performed at 1 Hz, 4 Hz, and 7 Hz respectively. These experiments use a return-to-zero velocity profile with four different velocities to check the zero offset and linearity throughout the run. Figure 6.9, with excitation at 1 Hz, shows a strong correlation with the input velocity. The use of both the gating and whitening filters results in zero offset with a clear velocity signal. Figure 6.10 with excitation at 4 Hz shows a resemblance to the input velocity in the raw and whitened results, however, application of gating removes this. This is likely due to the reduced number of samples available for averaging. Figure 6.11 shows results similar to that of Figure 6.10. Use of the gating filter reduces the number of samples such that the Gaussian noise cannot be adequately reduced by averaging. The raw and whitened results from both Figures 6.10 and 6.11 show a similar trend. They both start with a large bias voltage of approximately 1 µV which reduces until 750 s into the experiment when the gantry has stopped. The bias starts to increase again as the gantry moves back to its original position. The bias also appears to remain constant when the gantry velocity is zero from 300 s to 400 s, 750 s to 1000 s, and 1300 s to 1400 s. This suggests that the bias is due to the bending of the measurement loop and is a manifestation of the magnetic interference.

Figure 6.12 shows the results from the 1 Hz experiments, Figures 6.7 to 6.9, against the input velocity. The plot shows a linear response as a function of velocity. However, experiments 1 and 2 do show an increased deviation at $0.6\,\mathrm{mm\,s^{-1}}$ for an unknown reason. The trendline indicates a flow sensitivity of 680 nV/(mm/s) compared to the

simulation of this geometry which predicts a sensitivity of 1.1 µV/(mm/s). This factor of 0.6 could be accounted for by dimensional discrepancies between the modelled geometry and the real world experiment. A second factor which the simulations did not take into account is the reduced water velocity around the electrodes. As the electrodes move through the water, the no-slip condition implies the electrodes will *pull* the adjacent water along with them. This effectively reduces the water velocity around the electrode where they are most sensitive which could account for the lost 40% sensitivity.

Figure 6.13 shows results from an early experiment designed to test the linearity of the flowmeter. The results from this experiment show a large variance compared to the results from later experiments. The excess noise was found to be introduced due to poor grounding between the coil's power supply and the instrumentation. This was a recurring common-mode problem during experiments as the voltages on the coil switch between 0 V, 4 V, and 44 V instead of ±2 V and ±22 V. This was fixed in future experiments by ensuring the instrumentation, and the water in the aquifer tank and pool, were both referenced to the centre of the coil.

6.4 SUMMARY

The results shown here in Section 6.3, particularly Figure 6.12, show that it is possible to estimate the flow velocity, with 1 Hz excitation, in the rolling gantry rig using the methods described in this thesis. The application of the prewhitening and gating filters allow for the velocity to be estimated, independent of the magnetic interference, with a standard deviation as low as 40 nV. This suggests a measurement as slow as 60 µm s^{-1} (210 mm h^{-1}) is possible. Longer averaging per measurement could further improve this limit.

At higher frequencies, the lack of steady state samples available for the estimate results in large variances when using the gating filter. Without the gating filter, there are more samples but the estimation is susceptible to the magnetic interference as evidenced in Figures 6.7 and 6.9 to 6.11. This could be improved with a more accurate model of the signals during the transition periods as well as the use of an improved power supply.

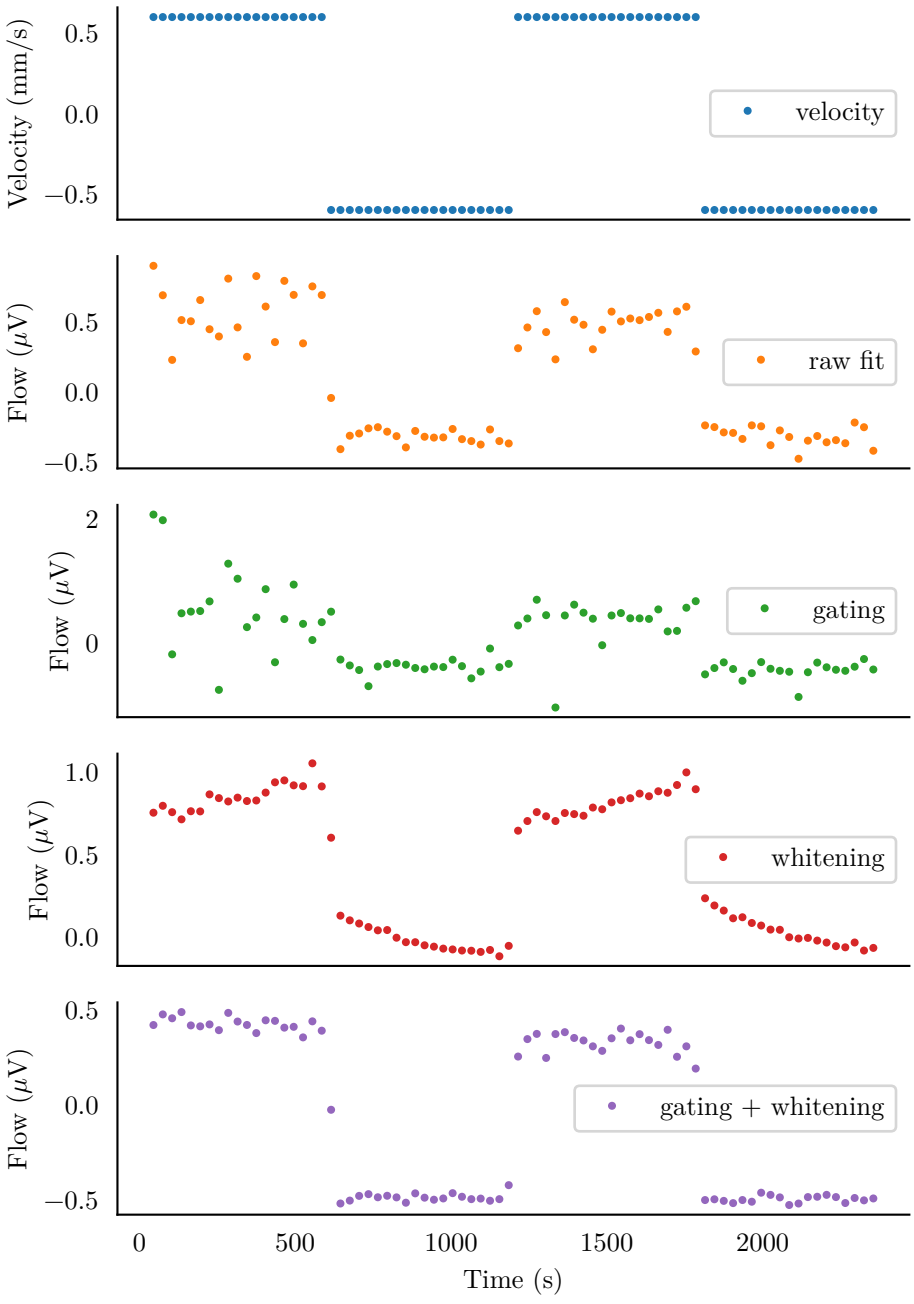

Figure 6.7 Moving gantry experiment with 1 Hz excitation. The direction of movement was reversed every 10 min. The use of gating and whitening provides the clearest results.

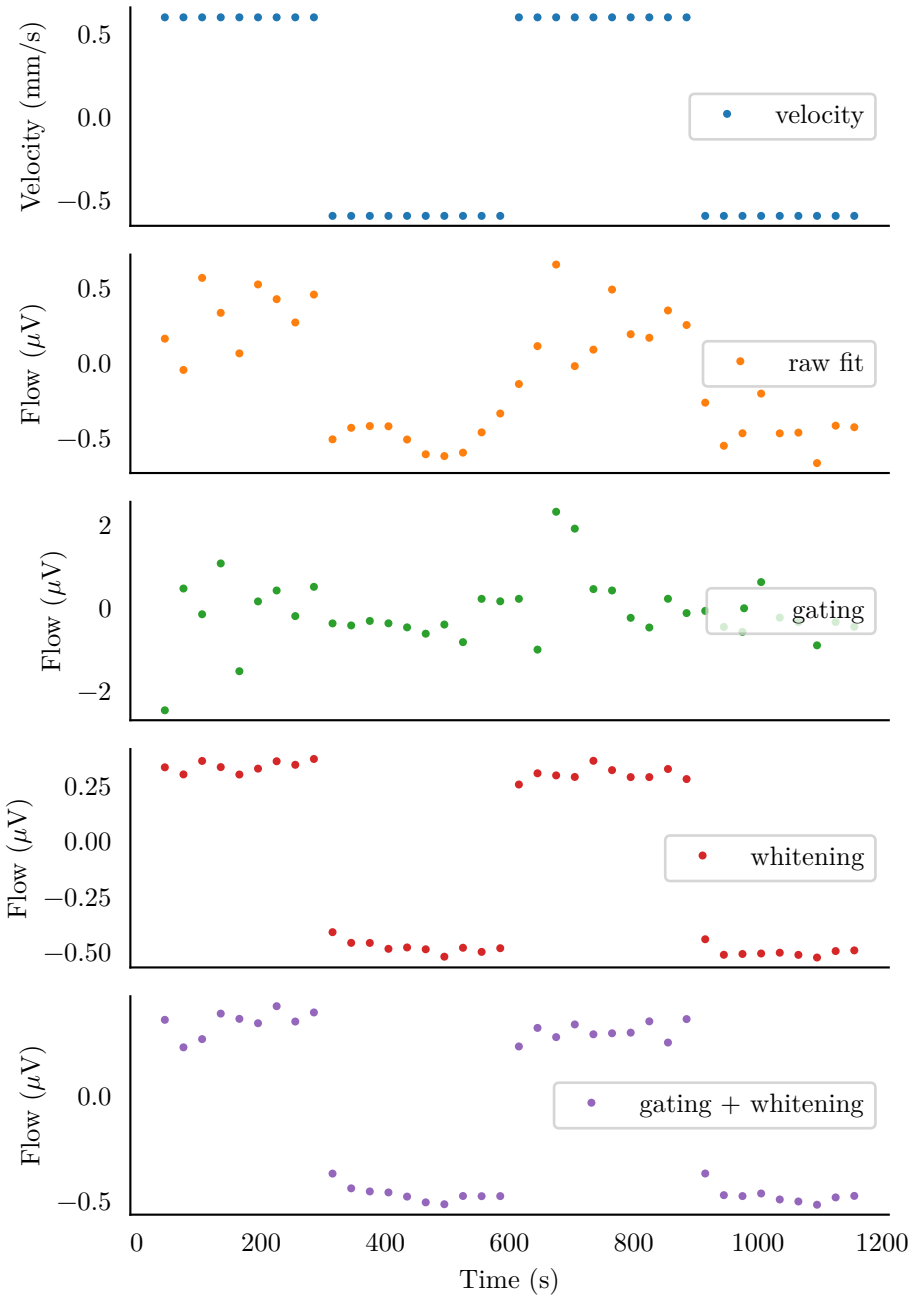

Figure 6.8 Moving gantry experiment with 1 Hz excitation. The direction of movement was reversed every 5 min. The use of gating and whitening provides the clearest results.

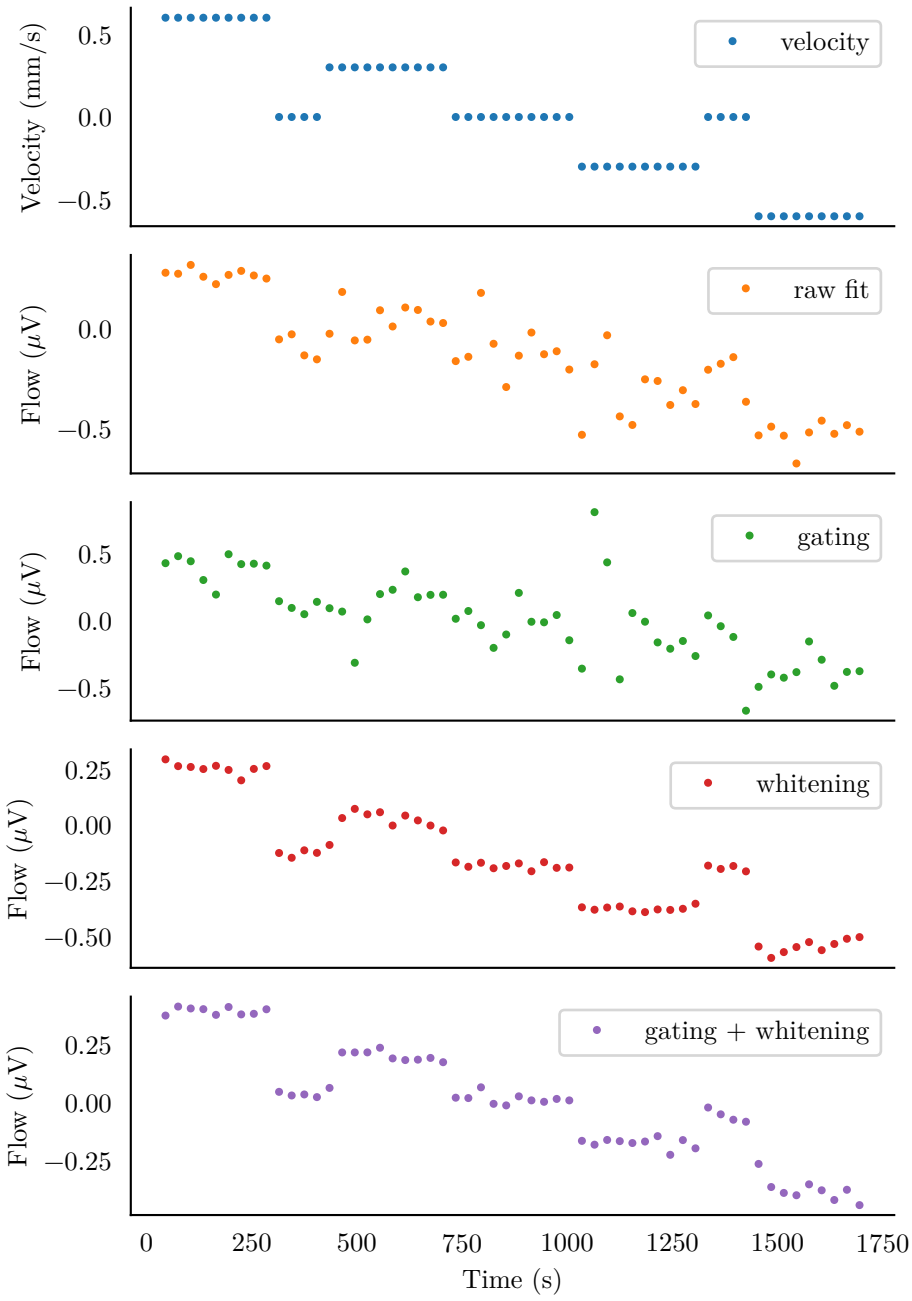

Figure 6.9 Moving gantry experiment with 1 Hz excitation with a return-to-zero velocity profile. The use of gating and whitening gives an output signal that very closely matches the input velocity, with zero DC offset. This result shows the output to be linear and repeatable over the velocity range.

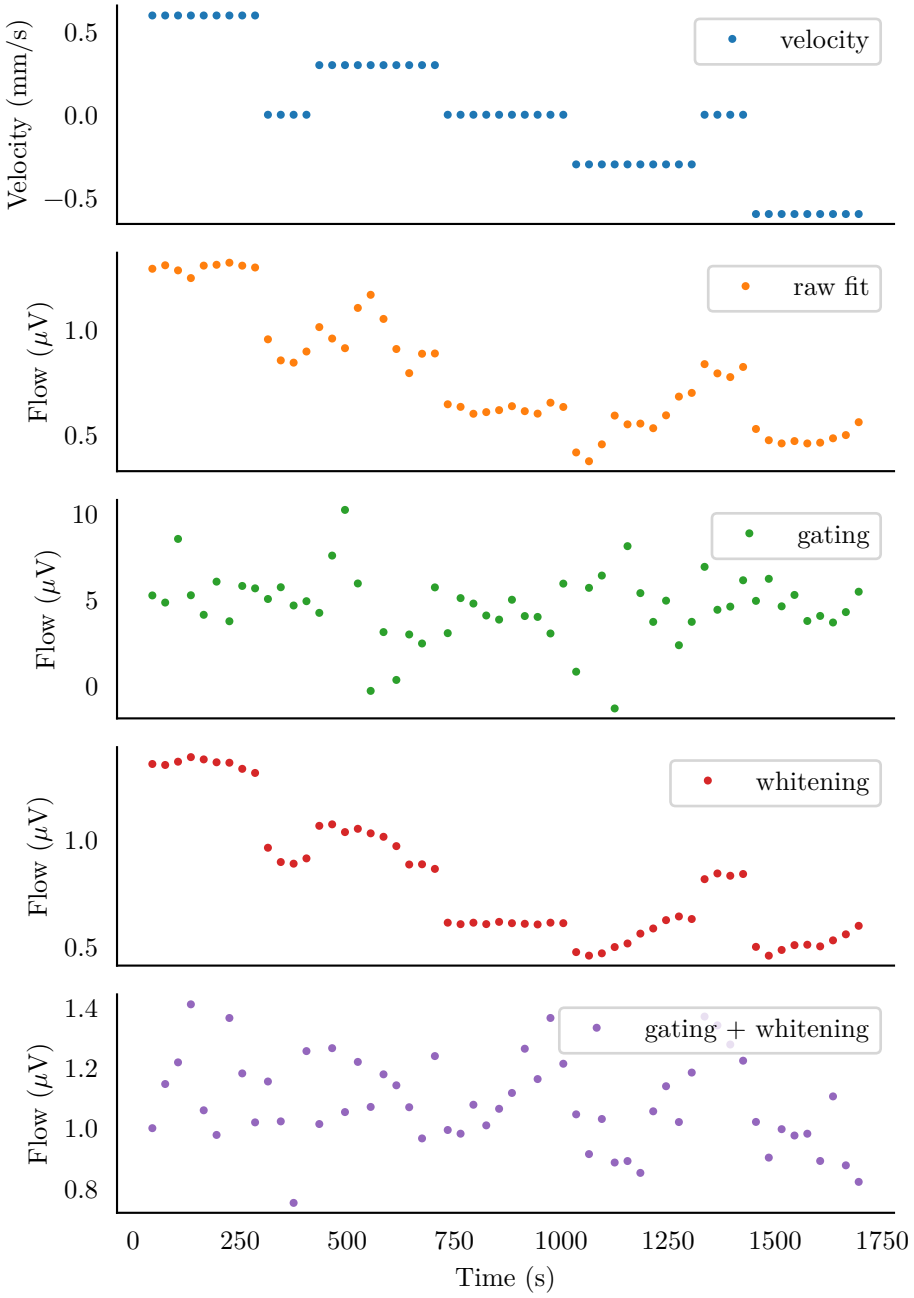

Figure 6.10 Moving gantry experiment with 4 Hz excitation with a return-to-zero velocity profile. This result shows a poor estimation of the input velocity. The non-gated outputs show a resemblance to the gantry velocity, combined with a random walk. The gated outputs show no obvious correlation. Due to the higher excitation frequency, the gating algorithm is reduced to excluding only the 5 leading and trailing samples.

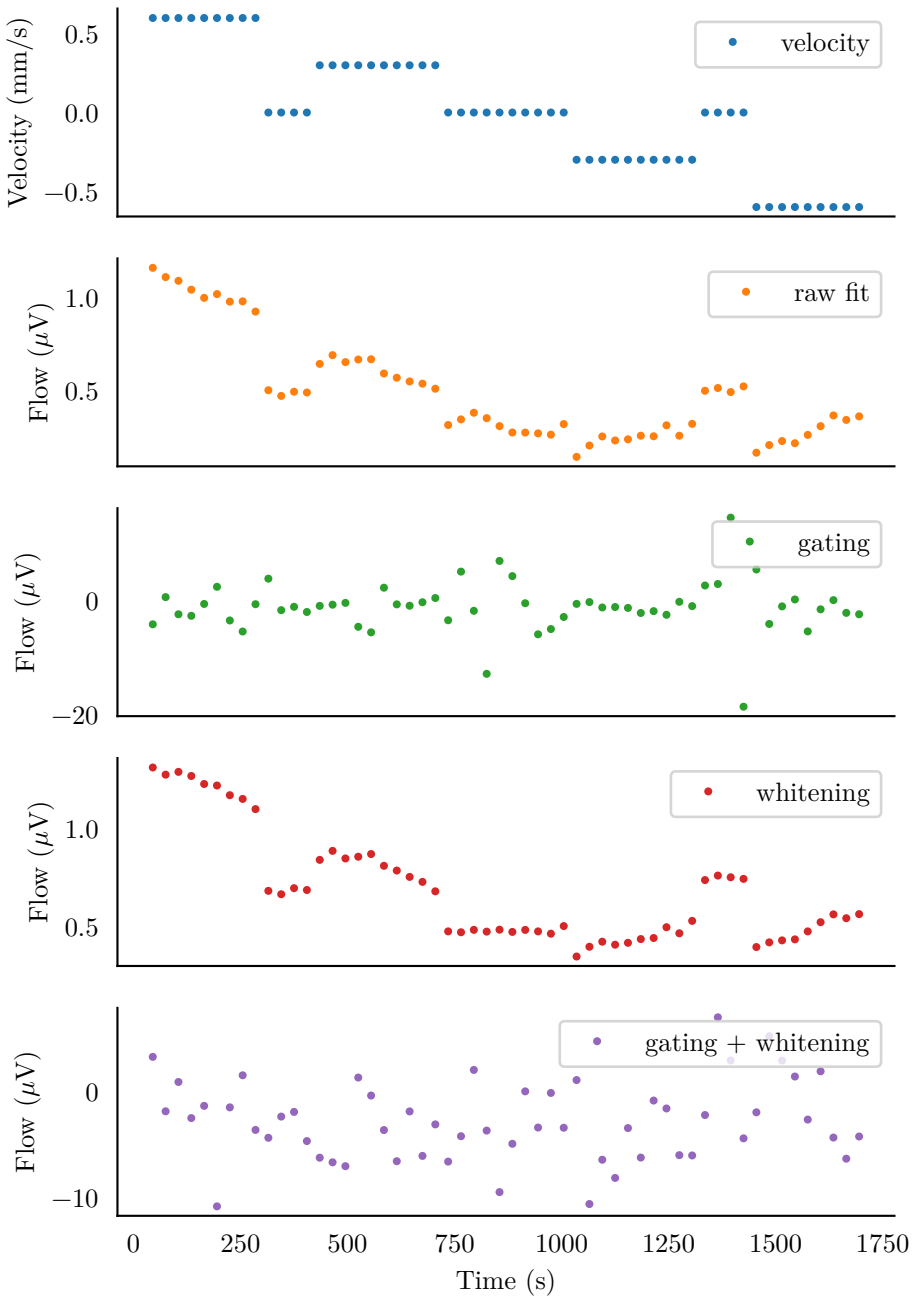

Figure 6.11 Moving gantry experiment with 7 Hz excitation with a varying velocity profile. This result shows a poor estimation of the input velocity. The non-gated outputs show a resemblance to the gantry velocity, combined with a random walk. The gated outputs show no obvious correlation. Due to the higher excitation frequency, the gating algorithm is reduced to excluding only the 5 leading and trailing samples.

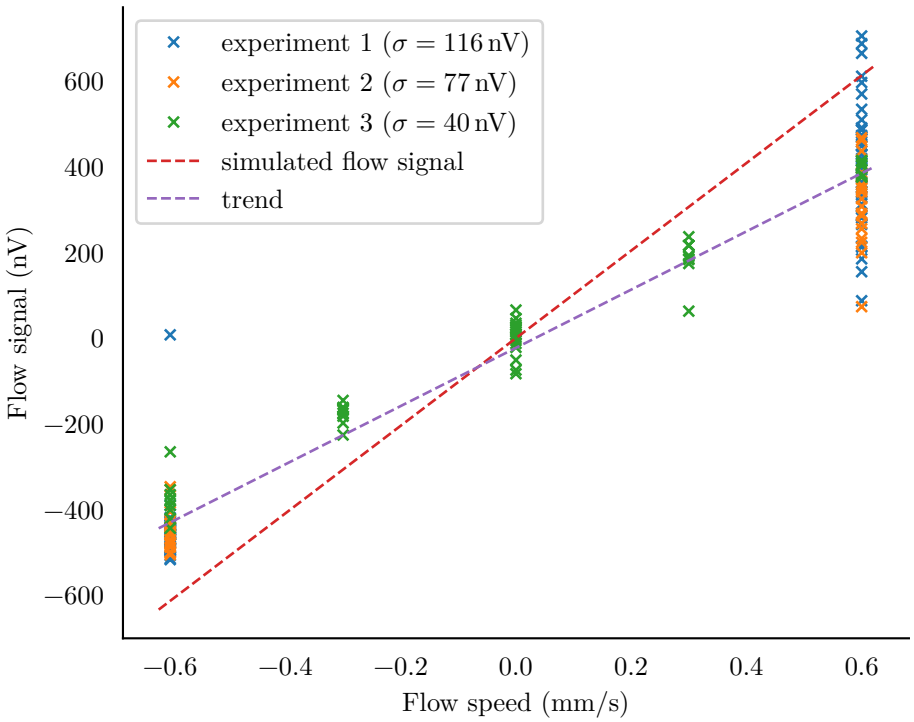

Figure 6.12 Plot of the estimated flow signal against the input velocity from Figures 6.7 to 6.9. The expected output derived from the simulations is shown to compare with the trend line. The trendline has an equation of $V = 680\,\mathrm{nV/(mm/s)}u - 20\,\mathrm{nV}$. The simulated flow signal has a gradient of $1.1\,\mu\mathrm{V/(mm/s)}$.

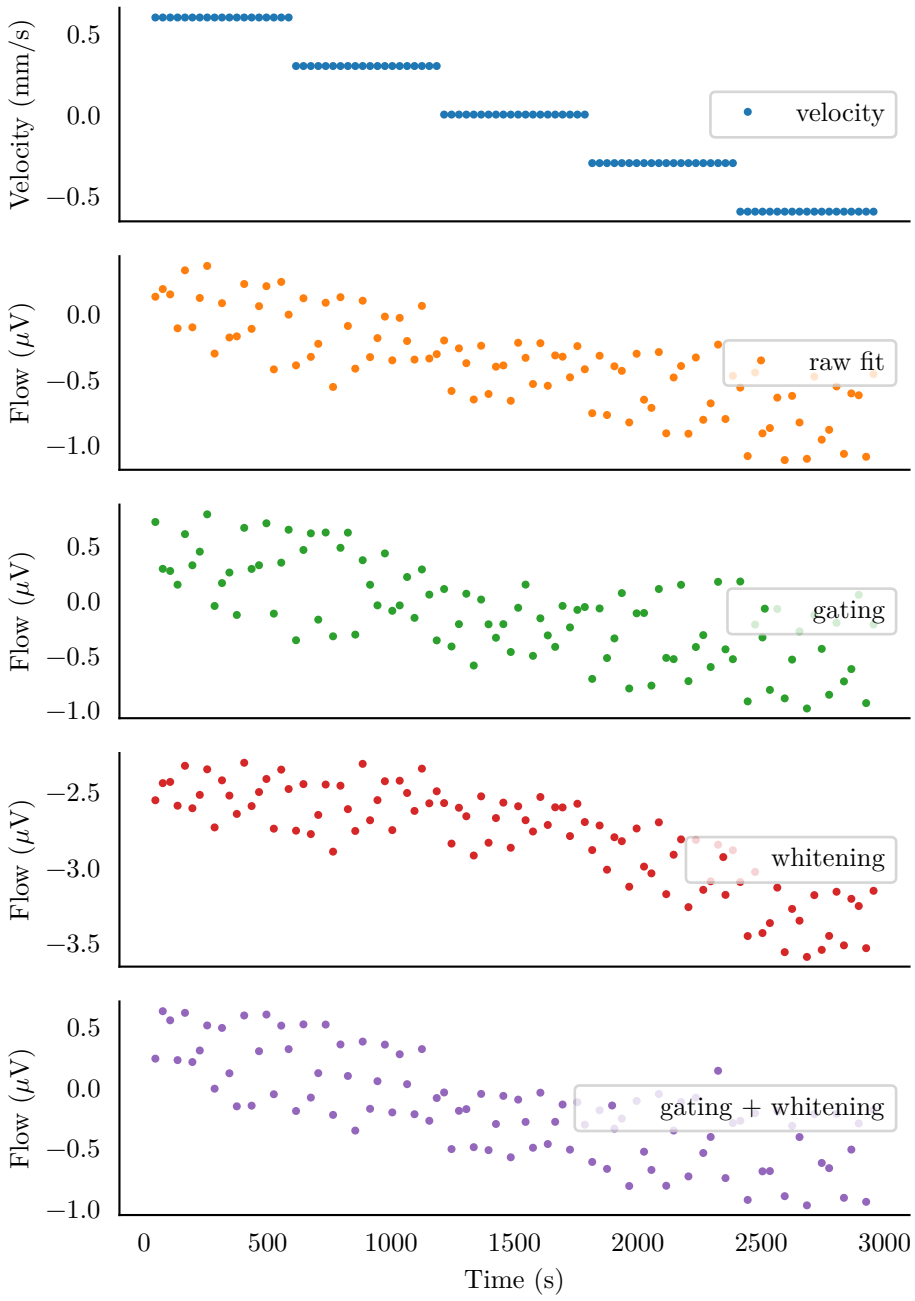

Figure 6.13 Moving gantry experiment with 1 Hz excitation with a stepped velocity profile. The velocity was reduced every 10 min. These results exhibit a much larger output variance than those of Figures 6.7 to 6.11.

Chapter 7

CONCLUSIONS AND RECOMMENDATIONS

The aim of this work was to prove the concept of an electromagnetic groundwater flowmeter. The results collected and presented here have shown that the flow speed can be measured at magnetic field excitation frequencies of 1 Hz in certain geometries using a combination of signal processing methods. Further, the flowmeter sensitivity agrees with those determined using numerical simulations of Bevir's weight vector method, within a range of error.

The simulations described in Chapter 2 have a wider impact on the field as they can be applied to all flowmeter geometries. This allows the prediction of output signals, as well as the optimisation of geometries to maximise sensitivities. The simulations can also provide a better understanding of how the electrode geometries can affect the spatial sensitivity of the EMFM.

7.1 DISCUSSION

The results presented in Chapter 6 show that the groundwater flowmeter concept is physically possible. The results shown in Figure 6.12, were able to produce linear estimates for the flow signal such as $(680 \pm 40)\,\mathrm{nV}$ for a velocity of $0.6\,\mathrm{mm\,s^{-1}}$. This estimate was also immune to the magnetic interference present in the experiment because of the application of the gating filters. At higher frequencies, the lack of steady state samples necessitated the removal of the gating filter. This allows more samples to be averaged for each estimate, however, the linear model used is an approximation during the switching periods. This results in the magnetic interference 'leaking' into the flow signal estimate as shown in the 4 Hz and 7 Hz experiments shown in Figures 6.10 and 6.11. The mini-aquifer experiments run at 7 Hz also show this interference effect with the gating filter removed. It should be noted that $\mathrm{d}i/\mathrm{d}t$ is expected to be orthogonal to $i(t)$ and not cause leakage. The magnetic interference leakage can be attributed to an incomplete model of the transformer effect.

The experiments performed in the mini-aquifer rig proved inconclusive. It would have been better to use 1 Hz excitation with the current power supply and average

the data for longer. There is also a lack of a ground truth regarding the water flow velocity. The bulk transfer model provided by Darcy's Law does not give enough spatial understanding of the flow, particularly around the baffle interfaces. The simulations developed in Section 3.11 indicate a large bias is introduced to the results when using an excitation frequency above 1 Hz. The results from Figures 5.8 to 5.11 do, however, show a susceptibility to the magnetic interference.

The magnetic interference encountered in the experiments presented here is potentially the source of the 'zero drift' phenomenon reported in literature [Hemp and Youngs 2003]. If the measurement loop geometry in a pipe flowmeter cannot be held constant for any reason (say due to a change of head or a movement due to thermal expansion), the magnitude of the magnetic interference present will change. Many flowmeter designs [Cushing 1973, Jakubowski and Michalski 2008, Mannherz et al. 1974, Michalski et al. 2013] make measurements when the magnetic excitation field is still changing and as such will pick up some of the magnetic interference signal. Any change in this interference signal can potentially result in a change in the estimated flow speed. The interference can also be modulated by the relative conductivity of the water around the electrodes as described in Section 5.3. A time varying interference coupling coefficient like this would give rise to the zero drift reported in literature.

There are two potential solutions to the magnetic interference described in this thesis: accurate modelling of the interference and all possible causes, or gating measurements such that only steady state samples are considered. This can be further improved by making use of a bipolar power supply designed to give fast transitions while providing an exact steady state current. However, this may be difficult due to the coil impedance.

Theoretically, operating at a higher frequency also allows the measurements to occur above the $1/f$ noise cut-off frequency measured in the system. This would reduce the noise present in the estimate, potentially by an order of magnitude. However, simulations and results have concluded that with the experimental setup described here, that it is more important to reduce the interference and simply average for longer.

The simulations developed as a part of this research are of particular use in the field of EMFM research. The results from Section 6.3 show the simulations can predict the output signal for a given geometry within an error of 60%. This scaling factor is also likely due to the impediment of the the water flow by the electrodes. The simulations could be applied as a 'dry' calibration for a flowmeter design of any geometry, or as part of a feedback loop for an optimisation algorithm. They have also shown that the flowmeter sensitivity is independent of the electrode design, unless the flow velocity is spatially varying. In cases such as those, the use of a large plate electrode, or approximating a plate electrode with a collection of electrically bonded electrodes, is the best choice to achieve near uniform spatial sensitivity.

The significant change in interference levels from 1 Hz to 4 Hz or 7 Hz cannot be

explained by the decrease in sample count alone. Figure 3.20 shows that at worst, a $2\times$ increase in the standard deviation can be expected by measuring at 10 Hz, however, this would be offset to a degree by the reduction in the $1/f$ noise. The increase in the interference is presumed to be a side effect of the magnetic interference. The electromagnetic excitation coil used is not a simple LR model as one might expect. The proximity effect inside the coil causes the model to appear more like an infinite series of LR models, all of which are in parallel with each other. The transient response of the coil, visible in Figure 3.19b, has a time constant in the order of 1 s. As the excitation frequency is increased, the average $\mathrm{d}i/\mathrm{d}t$ during a steady state will increase leading to larger magnetic interference on balance.

7.2 FUTURE WORK

The results presented in Chapter 6 verify that the rolling gantry geometry works. More experimentation with the mini-aquifer and field geometries at 1 Hz are required to fully validate the theory and simulations of previous chapters. Additional experiments should be performed with alternative electrode geometries to demonstrate that the flowmeter sensitivity is not directly related to the electrode shapes.

This work would benefit from additional research in a number of areas. A faster, and more accurate, power supply would allow for more steady state samples with less magnetic interference resulting in a reduced variance after parameter estimation. The power supply was initially designed for a simple LR type load, however, due to the proximity effect, the excitation coil exhibits more complex behaviour which leads to a significantly longer transient response. Additionally, improving the tunable coil described in Section 4.4 to have closed loop feedback such that it automatically tracks and minimises the magnetic interference has the potential to greatly reduce the magnitude of the interference signal.

The modelling presented in Chapter 3 is correct in the steady state case but is an approximation during the switching periods. A better model for the input signal will allow further rejection of the magnetic interference, potentially requiring a less strict gating filter. This could allow more samples per estimate and produce a better SNR. Further understanding the frequency dependency of the parameter estimation could also allow the estimation to occur at a higher frequency and reduce the effect of the $1/f$ flicker noise, further increasing the SNR. It is also understood that the electrode interface with the water can introduce nonlinearities to the source measurements. These nonlinearities result in the introduction of harmonics [Richardot and McAdams 2002] requiring a non-linear model to properly capture.

The GLS method for parameter estimation does not take into account any errors present in the measurement of the independent variables. The coil current and voltage measurements both have an associated noise spectrum, shown in Figure 4.4. Further

work should be applied to the parameter estimation methods to account for this error-in-variables problem [Wald 1940] in an effort to increase the flow signal SNR.

The flowmeter simulations presented in Chapter 2 make assumptions such as uniformity of the water velocity. Modelling of the input fluid using the Navier-Stokes equations, especially for the no-slip condition around the electrodes, will further increase the accuracy of the simulations. However, this is particularly difficult when the water is flowing through a sand baffle as described in Chapter 5. The water directly adjacent to the electrode is of particular concern due to its exaggerated weighting as indicated by the simulations in Chapter 2. Point electrodes in particular will suffer the most from these effects.

Finally, there is the potential to use the magnetic interference as a source of more flow information. The magnetic interference has a significantly larger SNR than the flow signal as shown in Figure 5.12. This interference signal is proportional to the difference in conductivity on opposite sides of the loops. For a homogeneous fluid, this corresponds to head difference which is proportional to the flow velocity through a baffle material. This signal could be used as an additional input to an adaptive model such as a Kalman filter if the result can be reliably zeroed using information from the flow signal. This could prove useful for high resolution and long term measurements.

Appendix A

NUMERICAL SOLVER FOR POISSON'S FUNCTION

Poisson's equation appears in a number of physical scenarios such as calculating the potential distribution around a source charge. It is defined as

$$\nabla^2\varphi(\mathbf{x}) = f(\mathbf{x})\,, \tag{A.1}$$

where ϕ and f are real or complex-valued functions, and ∇^2 is the Laplacian operator. This equation belongs to a class of problems called bounding value problems (BVPs). These are so named because the value at a position is governed by a differential equation and is not explicitly set. The only positions with a known value are on the boundary of the problem such as in Figure A.1.

A.1 BOUNDARY CONDITIONS

The boundary effects commonly appear in two forms: Dirichlet and Neumann conditions. These control the boundaries of the solution by either setting the result to be a constant, or setting the derivative of the result (with respect to the boundary) to be a constant respectively. A Dirichlet condition is usually written as

$$\varphi(\mathbf{x}) = f(\mathbf{x})\,, \quad \mathbf{x} \in \partial\Omega\,, \tag{A.2}$$

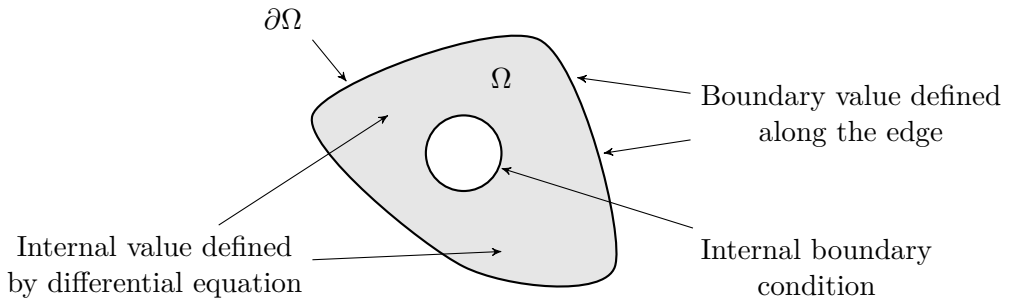

Figure A.1 Example region governed by a BVP with an external and internal boundary condition. The internal value is only governed by the differential equation defining its shape. The results are thus dependent on the specific boundary values.

and a Neumann condition as

$$\frac{\partial\varphi(\mathbf{x})}{\partial\mathbf{n}} = \nabla_{\mathbf{n}}\varphi(\mathbf{x}) = f'(\mathbf{x})\,, \quad \mathbf{x} \in \partial\Omega\,. \tag{A.3}$$

In terms of electrostatics, a volume that is enclosed in Dirichlet boundaries can be considered to be inside a metal box held at a given potential. The implication of this being that since the boundary has no potential differences, it has effectively infinite conductivity. On the other hand, a volume enclosed in Neumann boundaries is the equivalent of having an insulating box. The boundary is defined such that the potential difference through the surface is constant. Typically this is set to zero so there can be no current flow out of the volume.

A.2 FINITE DIFFERENCE METHOD

With three dimensional Cartesian coordinates, $\mathbf{x} \in \mathbb{R}^3$, (A.1) can be written as

$$\frac{\partial^2\varphi}{\partial x^2} + \frac{\partial^2\varphi}{\partial y^2} + \frac{\partial^2\varphi}{\partial z^2} = f(x,y,z). \tag{A.4}$$

The solution to this equation can be found using several methods. An iterative numerical approach (Jacobi relaxation), such as that described by Nagel and Org [2011], can be found by converting (A.4) to use discrete, second order, central differences,

$$\begin{aligned} \frac{\varphi_{x-1,y,z} + \varphi_{x+1,y,z} + \varphi_{x,y-1,z} + \varphi_{x,y+1,z} + \varphi_{x,y,z-1} + \varphi_{x,y,z+1} - 6\varphi_{x,y,z}}{h^2} &= f_{x,y,z} \\ \varphi_{x,y,z} = \frac{\varphi_{x-1,y,z} + \varphi_{x+1,y,z} + \varphi_{x,y-1,z} + \varphi_{x,y+1,z} + \varphi_{x,y,z-1} + \varphi_{x,y,z+1} - h^2 f_{x,y,z}}{6}&, \end{aligned} \tag{A.5}$$

where h is the grid spacing of the discretisation.[1] (A.5) can then be evaluated for each cell in the volume. The values from the previous iteration are sampled in a star pattern around the point being considered, as shown in Figure A.2. This allows the previous iteration terms in (A.5) to be combined into a single convolution term

$$C_{x,y,z} = \varphi_{x,y,z} * K_{i,j,k}\,, \tag{A.6}$$

where $*$ is the convolution operator, and K is the convolution kernel shown in Figure A.3. Substituting (A.6) into (A.5) gives

$$\varphi_{x,y,z} = C_{x,y,z} - \frac{h^2}{6} f_{x,y,z}\,. \tag{A.7}$$

This result is a standard FDM solver for Poisson's equation often used in literature.

[1] A derivation exists where h_x, h_y, and h_z can have different values, but for simplicity, here they are defined equal such that $h = h_x = h_y = h_z$.

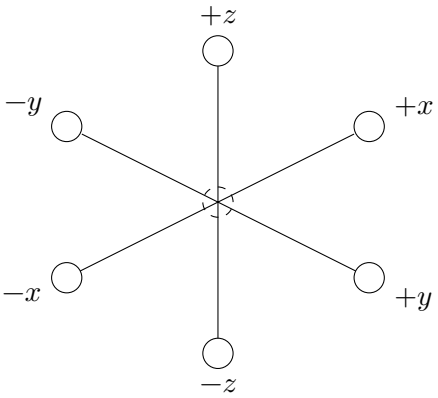

Figure A.2 Diagram of the sample points being averaged around a sample point being considered.

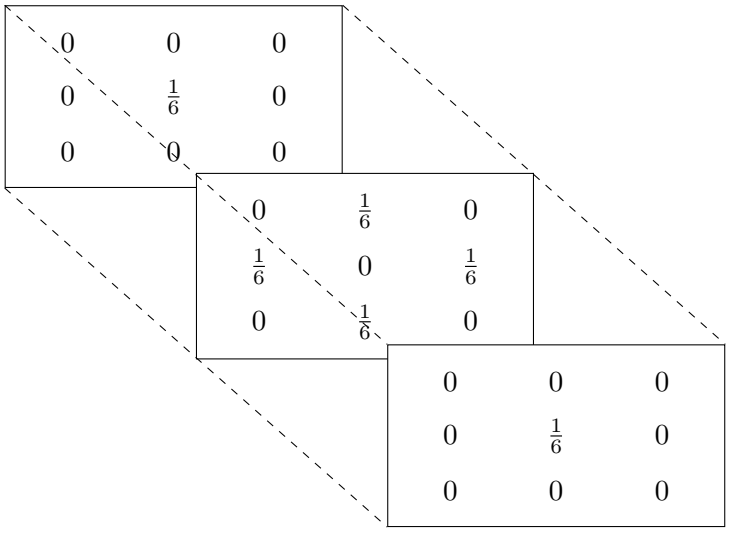

Figure A.3 Sample kernel used to simplify iteration.

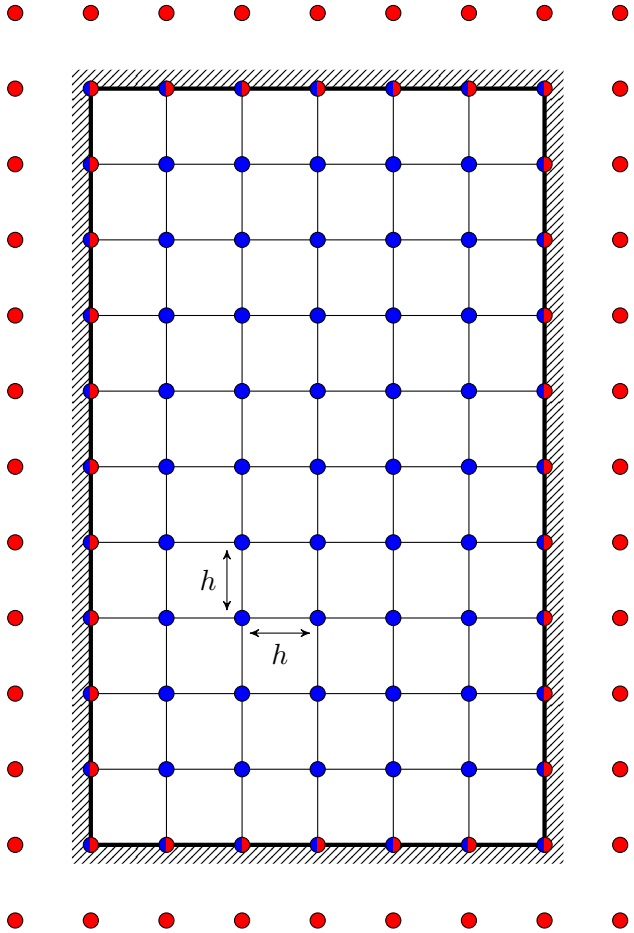

Figure A.4 Grid showing the location of the sampling points and the boundaries. The blue samples are normal points inside the boundaries controlled by Poisson's equation. The red samples outside the boundaries are held at specific values during the FDM iterations to get the correct boundary behaviour. The behaviour of values that lie on the boundary are determined by the specific boundary condition applied.

The geometry must also be defined in terms of a regular grid. Figure A.4 shows the locations of the sampling points and how they are defined. The blue internal points are governed purely by the differential equations and are equally spaced inside the volume. The blue/red boundary points represent the values of the function on the inner face of the boundary. They are controlled by either a Dirichlet condition or by the differential equation in the case of a Neumann boundary. The red external samples, sometimes referred to as 'ghost' points in literature, are defined outside the boundary to control the gradient of boundary points in the case of a Neumann condition. Figure A.5 shows how the value of a sample is set in the case of a Dirichlet boundary, and Figure A.6 shows how the gradient is set for a Neumann boundary.

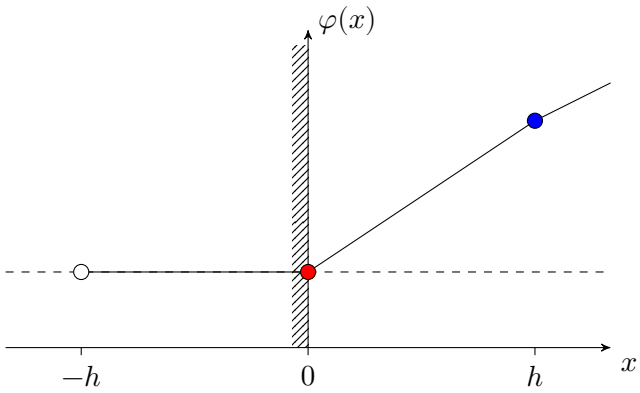

Figure A.5 Diagram of a Dirichlet boundary. The value at the boundary is held at a constant value during FDM iteration. The value outside the boundary can be ignored as it has no bearing on the FDM result (unless used to set a Neumann condition).

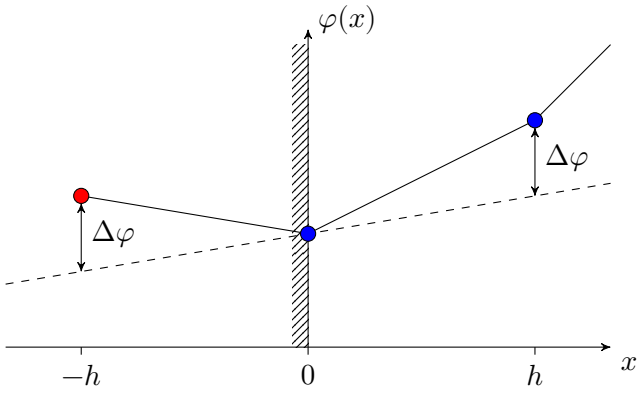

Figure A.6 Diagram of a Neumann boundary. The value outside the boundary is set such that the gradient at the boundary is held at a constant value during FDM iteration. This is done by setting the red samples value such that the two distances indicated are equal. If the Neumann condition is zero, then the value of the red sample is equal to the value of the inner blue sample.

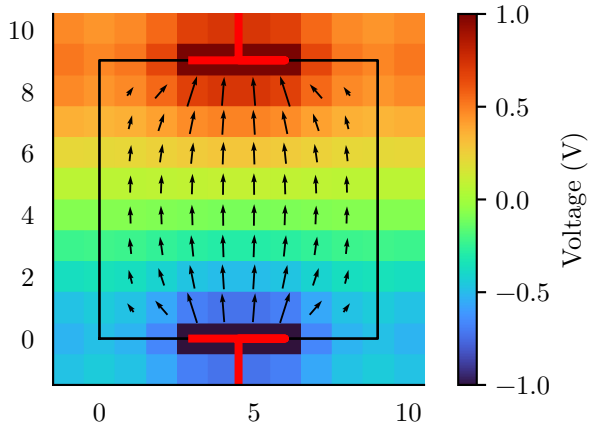

Figure A.7 Simulation of a parallel plate capacitor. The boundary, shown as the black line, is a Neumann condition simulating an insulating box. The plates themselves are held at $\pm 1\,\mathrm{V}$ creating an electric field gradient between them. The arrows show the electric field strength between the plates. Note that the samples are located in the centre of each cell in the image.

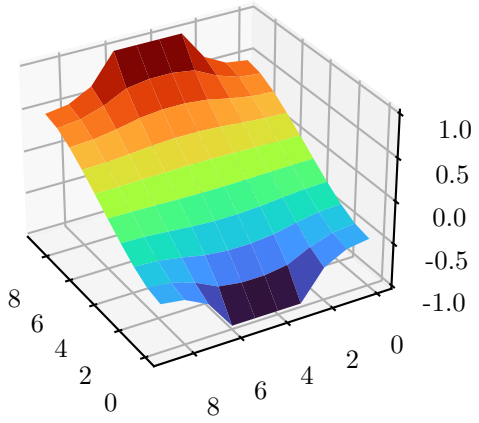

Figure A.8 3D surface plot of the potentials inside the capacitor box in Figure A.7.

A.3 2D CAPACITOR EXAMPLE

A simplified 2-dimensional example of a parallel plate capacitor is simulated in Figure A.7. The two plates are defined as Dirichlet conditions with $\pm 1\,\mathrm{V}$ applied. The remainder of the boundary is defined as a Neumann condition such that no current can flow through the box walls. The resultant potentials in the box show a smooth gradient, visible in Figure A.8. Also visible is the flat gradient of the surface around the outer edge of the surface.

Appendix B

5 Hz INTERFERENCE

Early in the aquifer experimental stage, a 5 Hz signal was noticed in the measured data. Figure B.1 shows this during a background noise measurement. None of the equipment used during experimentation operated at 5 Hz and so eventually, we believed it to be a higher frequency signal being demodulated through the electrode-electrolyte interface in the flowmeter. This signal remained a mystery until an investigation using an improvised electromagnetic interference (EMI) detector was performed. The software defined radio (SDR) allowed a chunk of the high frequency spectrum, i.e., 13 MHz to 13.01 MHz, to be shifted down to baseband and converted to audio. Cycling through all signals found one at 13.56 MHz which when demodulated produced an exact 5 Hz beeping tone. This led to the discovery shown in Figure B.2 where we were able to determine that the university's door card access system was the source of the signal. These card readers are located at all laboratory and external doorways. These card readers appear to pulse a 13.56 MHz sinusoidal search tone every 200 ms. This high frequency signal has a wavelength of 22.11 m. The power supply used at the time was mounted in a steel chassis, with a total length of 3 m. This acted as a poor antenna, which coupled the signal into the experiment tank where it was envelope demodulated into our instrumentation.

This is an unusual problem to have but there are several solutions. First a smaller power supply can be used to stop the card reader signal from coupling in. Proper shielding of the laboratory is another option. A last resort solution is to change the geometry of the 'antenna' such that the signal coupling into the tank is cancelled out.

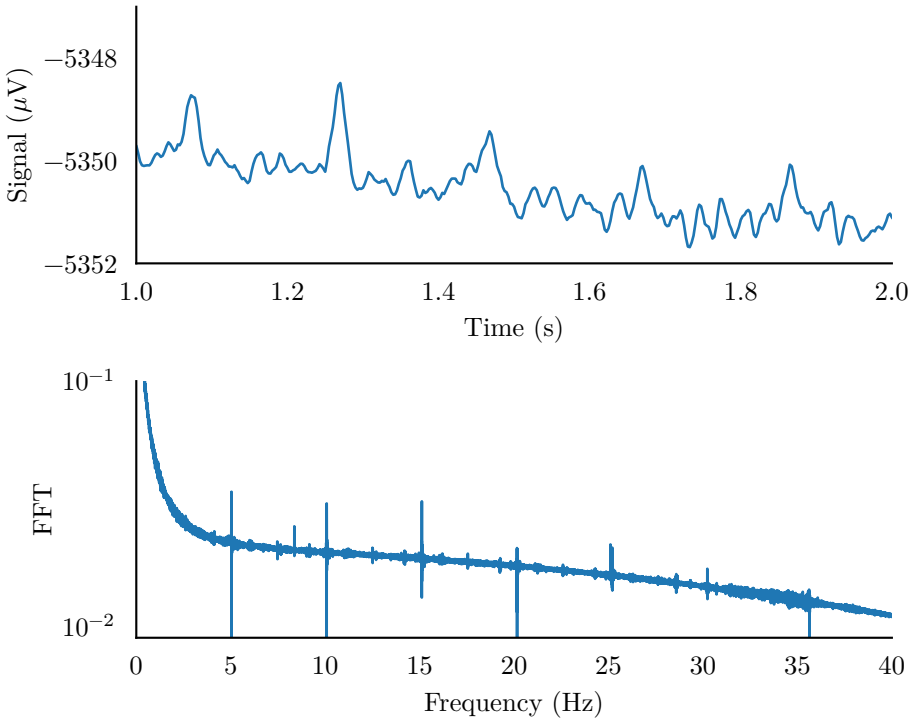

Figure B.1 Background noise capture showing a 5 Hz signal and its harmonics.

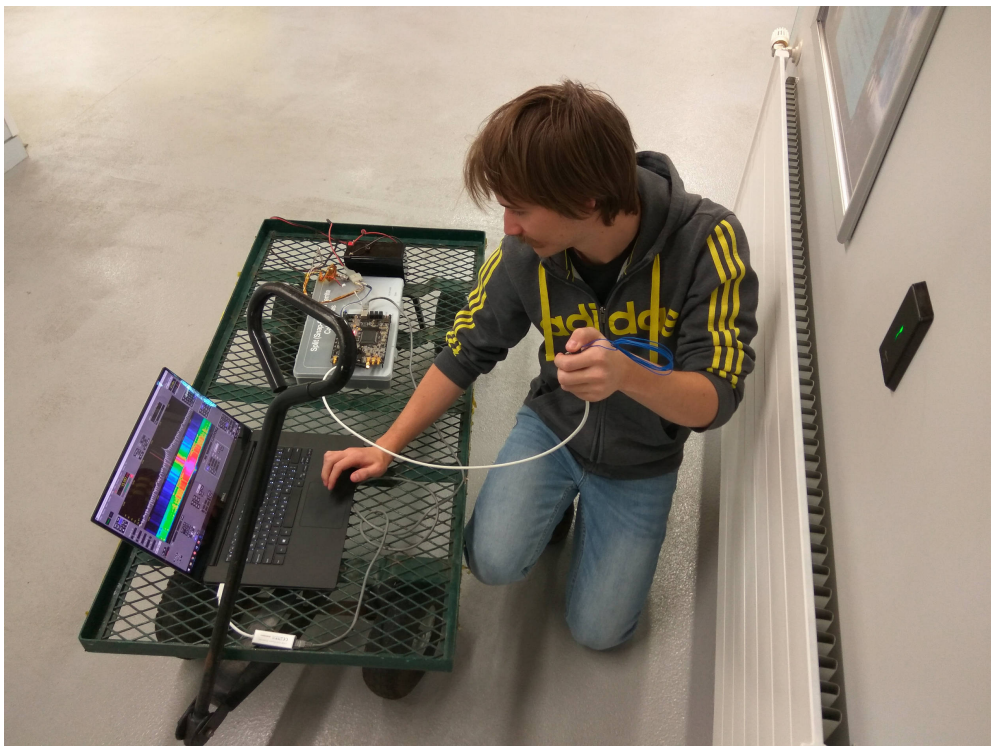

Figure B.2 Photo of an improvised EMI detector using a laptop, a software defined radio, and a coil of wire. Note the waterfall plot visible on the laptop screen showing a large increase in signal intensity as the antenna is moved closer to the security card reader.

Appendix C

EXPERIMENTAL GEOMETRIES

C.1 MINI-AQUIFER

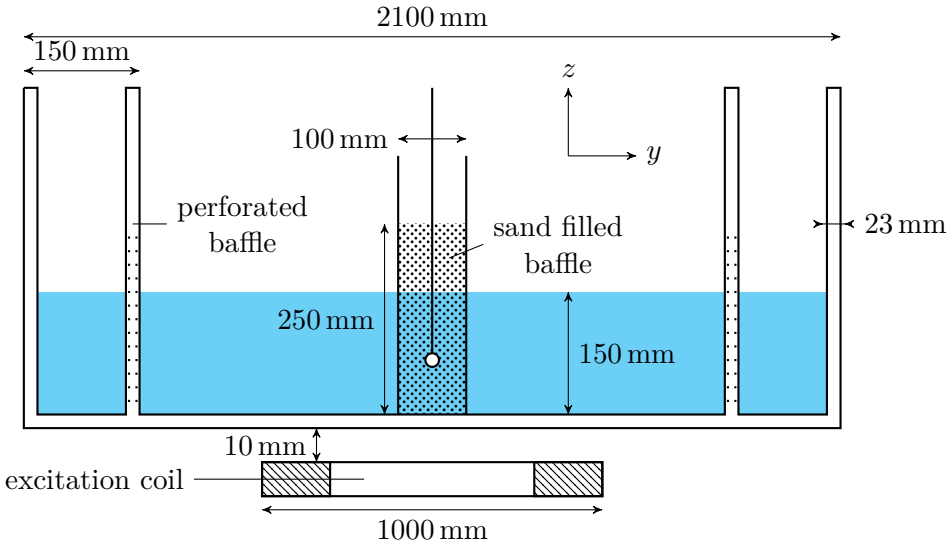

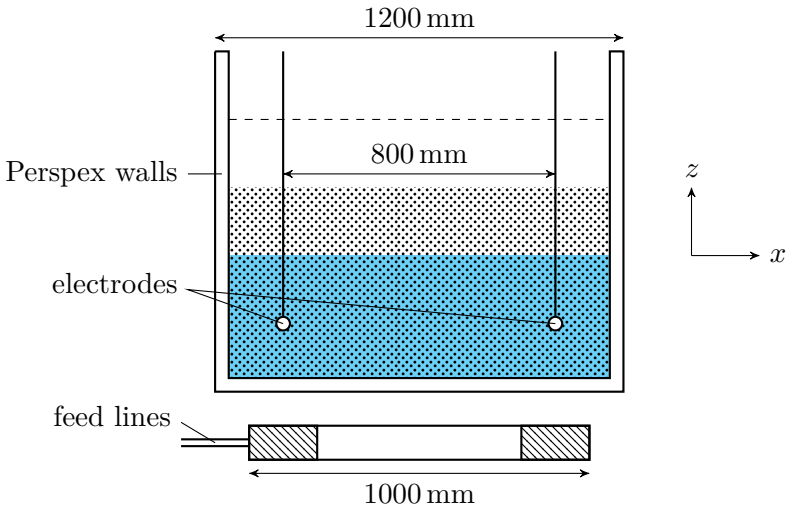

C.2 ROLLING GANTRY

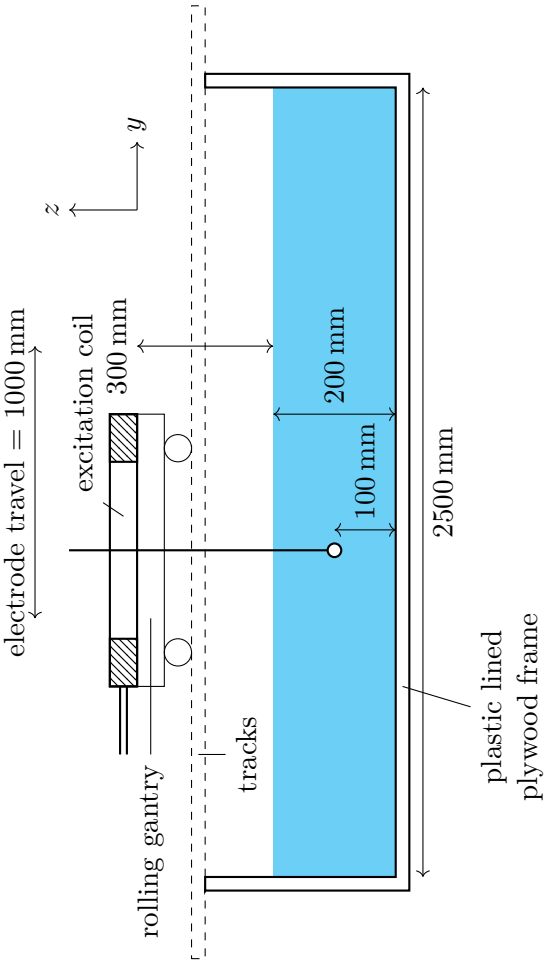

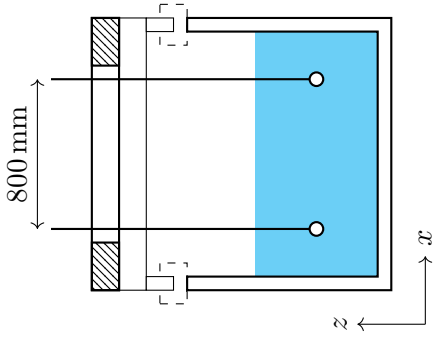

REFERENCES

Al-Rabeh, R., Baker, R.C. and Hemp, J. (1978), "Induction Flow-Measurement Theory for Poorly Conducting Fluids", *Proceedings of the Royal Society of London. Series A, Mathematical and Physical Sciences*, Vol. 361, No. 1704, pp. 93–107.

Alexander, K. (1939), "Apparatus for measuring fluid flow", US2149847A, United States Patent and Trademark Office.

Alley, W.M., Reilly, T.E. and Franke, O.L. (1999), *Sustainability of Ground-Water Resources*, Vol. 1186, US Department of the Interior, US Geological Survey.

Amare, T. (1999), "Design of an electromagnetic flowmeter for insulating liquids", *Measurement Science and Technology*, Vol. 10, No. 8, pp. 755–758.

Appel, E., Geisler, G., Kiene, W. and Seebode, A. (1976), "Electromagnetic flowmeter with shielded electrodes", US3999443A, United States Patent and Trademark Office.

Baker, R.C. (2011), "On the concept of virtual current as a means to enhance verification of electromagnetic flowmeters", *Measurement Science and Technology*, Vol. 22, No. 10, p. 105403.

Bevir, M.K. (1970), "The theory of induced voltage electromagnetic flowmeters", *Journal of Fluid Mechanics*, Vol. 43, No. 03, p. 577.

Bevir, M.K. (1969), *Induced Voltage Electromagnetic Flowmeters*, Ph.D., University of Warwick.

Billah, K.Y.R. and Shinozuka, M. (1990), "Numerical method for colored-noise generation and its application to a bistable system", *Physical Review A*, Vol. 42, No. 12, pp. 7492–7495.

Bonnett, B., Mitchell, B., Frampton, M. and Hayes, M. (2019), "Low-noise instrumentation for electromagnetic groundwater flow measurement", In *2019 IEEE International Instrumentation and Measurement Technology Conference (I2MTC)*, IEEE.

Bouwer, H. and Rice, R.C. (1976), "A slug test for determining hydraulic conductivity of unconfined aquifers with completely or partially penetrating wells", *Water Resources Research*, Vol. 12, No. 3, pp. 423–428.

Bowden, K.F. and Hughes, P. (1961), "The flow of water through the Irish Sea and its relation to wind", *Geophysical Journal International*, Vol. 5, No. 4, pp. 265–291.

Bowden, K.F. (1956), "The flow of water through the Straits of Dover, related to wind and differences in sea level", *Philosophical Transactions of the Royal Society of London. Series A, Mathematical and Physical Sciences*, Vol. 248, No. 953, pp. 517–551.

Cha, J.E., Ahn, Y.C. and Kim, M.H. (2002), "Flow measurement with an electromagnetic flowmeter in two-phase bubbly and slug flow regimes", *Flow Measurement and Instrumentation*, Vol. 12, No. 5, pp. 329–339.

Colton, D.L., Kress, R. and Kress, R. (1998), *Inverse Acoustic and Electromagnetic Scattering Theory*, Vol. 93, Springer.

Cordell, A.R. and Spencer, M.P. (1959), "Electromagnetic Blood Flow Measurements in Extracorporeal Circuits", *IRE Transactions on Medical Electronics*, Vol. ME-6, No. 4, pp. 228–231.

Cox, T.J. and Wyatt, D.G. (1984), "An electromagnetic flowmeter with insulated electrodes of large surface area", *Journal of Physics E: Scientific Instruments*, Vol. 17, No. 6, pp. 488–503.

Cushing, V. (1973), "Electromagnetic water current meter", US3759097A, United States Patent and Trademark Office.

Cushing, V. (1965), "Electromagnetic Flowmeter", *Review of Scientific Instruments*, Vol. 36, No. 8, pp. 1142–1148.

Denison, A.B., Spencer, M.P. and Green, H.D. (1955), "A Square Wave Electromagnetic Flowmeter for Application to Intact Blood Vessels", *Circulation Research*, Vol. 3, No. 1, pp. 39–46.

Faraday, M. (1832), "The Bakerian lecture. - Experimental researches in electricity.", *Philosophical Transactions of the Royal Society of London*, Vol. 122, pp. 163–194.

Fetter, C.W. (2001), *Applied Hydrogeology*, Prentice Hall, 4th ed.

Filloux, J.H. (1973), "Tidal Patterns and Energy Balance in the Gulf of California", *Nature*, Vol. 243, No. 5404, pp. 217–221.

Gleick, P. (1996), "Water resources", *Encyclopedia of climate, weather*, pp. 817–823.

Heffernan, B., Mitchell, B. and Hayes, M. (2020), "Trapezoidal Current Generator for an Electromagnetic Groundwater Flowmeter", In *2020 IEEE International Instrumentation and Measurement Technology Conference (I2MTC)*, IEEE.

Hemp, J. and Sanderson, M.L. (1981), "Electromagnetic flowmeters: A state of the art review", In *BHRA Fluid Eng. Int. Adv. In Flow Meas. Techniques*, .

Hemp, J. and Youngs, I. (2003), "Problems in the theory and design of electromagnetic flowmeters for dielectric liquids. Part 3a. Modelling of zero drift due to flux linkage between coil and electrode cables", *Flow Measurement and Instrumentation*, Vol. 14, No. 3, pp. 65–78.

Hemp, J., Sanderson, M.L., Koptioug, A.V., Liang, B., Sweetland, D.J. and Al Rabeh, R.H. (2002), "Problems in the theory and design of electromagnetic flowmeters for dielectric liquids: Part 1: Experimental assessment of static charge noise levels and signal-to-noise ratios", *Flow Measurement and Instrumentation*, Vol. 13, No. 4, pp. 143–153.

Horowitz, P. and Hill, W. (2015), *The Art of Electronics*, Cambridge Univ. Press, 3rd ed.

Hughes, P. (1969), "Submarine cable measurements of tidal currents in the Irish Sea", *Limnology and Oceanography*, Vol. 14, No. 2, pp. 269–278.

Igor, S. (1993), "World fresh water resources", *Water in crisis: a guide to the world's. Oxford University Press, Inc, Oxford*.

Jakubowski, J. and Michalski, A. (2005), "Some New Aspects of Bipolar Excitation in the Field of Electromagnetic Flow Measurement for Open Channels", In *2005 IEEE Instrumentationand Measurement Technology Conference Proceedings*, Vol. 1, pp. 431–436.

Jakubowski, J. and Michalski, A. (2006), "A new approach to the estimation of basic flow parameters within the electromagnetic measuring method for open channels", *IEEE Instrumentation Measurement Magazine*, Vol. 9, No. 3, pp. 60–75.

Jakubowski, J. and Michalski, A. (2008), "Application of Selected Linear Algebra Processing Methods in the Electromagnetic Flow Measurement for Open Channels", *IEEE Transactions on Instrumentation and Measurement*, Vol. 57, No. 8, pp. 1678–1684.

Jakubowski, J. and Michalski, A. (2009), "Combined measurement of flow velocity and filling within fully electromagnetic flowmeter open channels", In *Fundamental and Applied Metrology*, .

Jones, M.H. and Scott, J. (2015), "Scaling of Electrode-Electrolyte Interface Model Parameters In Phosphate Buffered Saline", *IEEE Transactions on Biomedical Circuits and Systems*, Vol. 9, No. 3, pp. 441–448.

Keshner, M.S. (1982), "1/f noise", *Proceedings of the IEEE*, Vol. 70, No. 3, pp. 212–218.

Kirchner, J.W. (2005), "Aliasing in 1/fα noise spectra: Origins, consequences, and remedies", *Physical Review E*, Vol. 71, No. 6, p. 066110.

Kolin, A. (1945), "An Alternating Field Induction Flow Meter of High Sensitivity", *Review of Scientific Instruments*, Vol. 16, No. 5, pp. 109–116.

Levkov, C., Mihov, G., Ivanov, R., Daskalov, I., Christov, I. and Dotsinsky, I. (2005), "Removal of power-line interference from the ECG: A review of the subtraction procedure", *BioMedical Engineering OnLine*, Vol. 4, No. 1, p. 50.

Linnert, M.A., Mariager, S.O., Rupitsch, S.J. and Lerch, R. (2018), "Dynamic offset correction of electromagnetic flowmeters", *IEEE Transactions on Instrumentation and Measurement*, Vol. 68, No. 5, pp. 1284–1293.

Longuet-Higgins, M.S. (1949), "The Electrical and Magnetic Effects of Tidal Streams", *Geophysical Supplements to the Monthly Notices of the Royal Astronomical Society*, Vol. 5, No. 8, pp. 285–307.

Lovett, A. and Cameron, S. (2015), *Development of a National Groundwater Atlas for New Zealand*, GNS Science, Te Pū Ao.

Luo, W., Dong, H., Xu, J., Ge, J., Liu, H. and Zhang, C. (2020), "Development and characterization of high-stability all-solid-state porous electrodes for marine electric field sensors", *Sensors and Actuators A: Physical*, Vol. 301, p. 111730.

Mack, C.A. (2013), "Systematic errors in the measurement of power spectral density", *Journal of Micro/Nanolithography, MEMS, and MOEMS*, Vol. 12, No. 3, p. 033016.

Magin, R.L. and Ovadia, M. (2008), "Modeling the cardiac tissue electrode interface using fractional calculus", *Journal of Vibration and Control*, Vol. 14, No. 9-10, pp. 1431–1442.

Mannherz, E., Riester, H., Schmoock, R. and Yard, J. (1974), "Electromagnetic flowmeter with square-wave excitation", US3783687A, United States Patent and Trademark Office.

Michalski, A., Sikora, J. and Wincenciak, S. (1988), "Optimal shape design of an electromagnetic flow gauge", *IEEE Transactions on Magnetics*, Vol. 24, No. 1, pp. 565–568.

Michalski, A., Starzynski, J. and Wincenciak, S. (1998), "Optimal design of the coils of an electromagnetic flow meter", *IEEE Transactions on Magnetics*, Vol. 34, No. 5, pp. 2563–2566.

Michalski, A., Jakubowski, J. and Watral, Z. (2013), "The problems of pulse excitation in electromagnetic flowmeters", *IEEE Instrumentation Measurement Magazine*, Vol. 16, No. 5, pp. 47–52.

Molz, F.J., Boman, G.K., Young, S.C. and Waldrop, W.R. (1994), "Borehole flowmeters: Field application and data analysis", *Journal of Hydrology*, Vol. 163, No. 3, pp. 347–371.

Molz, F. and Young, S. (1993), "Development And Application Of Borehole Flowmeters For Environmental Assessment", *The Log Analyst*, Vol. 34, No. 01.

Muskat, M. (1937), "The Flow of Fluids Through Porous Media", *Journal of Applied Physics*, Vol. 8, No. 4, pp. 274–282.

Nagel, J. and Org, N. (2011), "Solving the Generalized Poisson Equation Using the Finite-Difference Method (FDM)", Feb.

Nguyen, H.L., Sibille, P. and Garnier, H. (1993), "A new bias-compensating least-squares method for identification of stochastic linear systems in presence of coloured noise", In *Proceedings of 32nd IEEE Conference on Decision and Control*, pp. 2038–2043 vol.3.

Nuttall, A. (1981), "Some windows with very good sidelobe behavior", *IEEE Transactions on Acoustics, Speech, and Signal Processing*, Vol. 29, No. 1, pp. 84–91.

Okaniwa, H., Mitsutake, I. and Koshimizu, A. (1995), "Electromagnetic flowmeter", US5388465A, United States Patent and Trademark Office.

Paillet, F.L. (2004), "Borehole flowmeter applications in irregular and large-diameter boreholes", *Journal of Applied Geophysics*, Vol. 55, No. 1, pp. 39–59.

Polo, J., Pallas-Areny, R. and Martin-Vide, J. (2001), "Analog signal processing in an AC electromagnetic flowmeter", In *IMTC 2001. Proceedings of the 18th IEEE Instrumentation and Measurement Technology Conference. Rediscovering Measurement in the Age of Informatics (Cat. No.01CH 37188)*, Vol. 3, IEEE, Budapest, Hungary, pp. 2136–2139.

Rajan, K.K. and Vijayakumar, G. (2014), "Stabilization of magnet assemblies of permanent magnet sodium flowmeters used in fast breeder reactors", *Nuclear Engineering and Design*, Vol. 275, pp. 368–374.

Richardot, A. and McAdams, E.T. (2002), "Harmonic analysis of low-frequency bioelectrode behavior", *IEEE Transactions on Medical Imaging*, Vol. 21, No. 6, pp. 604–612.

Robinson, I.S. and Deacon, G.E.R. (1976), "A theoretical analysis of the use of submarine cables as electromagnetic oceanographic flowmeters", *Philosophical Transactions of the Royal Society of London. Series A, Mathematical and Physical Sciences*, Vol. 280, No. 1297, pp. 355–396.

Rosales, C., Sanderson, M.L. and Hemp, J. (2002a), "Problems in the theory and design of electromagnetic flowmeters for dielectric liquids. Part 2a: Theory of noise generation by turbulence modulation of the diffuse ionic charge layer near the pipe wall", *Flow Measurement and Instrumentation*, Vol. 13, No. 4, pp. 155–163.

Rosales, C., Sanderson, M.L. and Hemp, J. (2002b), "Problems in the theory and design of electromagnetic flowmeters for dielectric liquids. Part 2b: Theory of noise generation by charged particles", *Flow Measurement and Instrumentation*, Vol. 13, No. 4, pp. 165–171.

Rosen, M.R., White, P.A. and Society, N.Z.H. (editors) (2001), *Groundwaters of New Zealand*, New Zealand Hydrological Society, Wellington, N.Z.

Sai, Y. and Kubota, Y. (1999), "Electromagnetic flowmeter", US5880376A, United States Patent and Trademark Office.

Saito, K., Sakurai, Y. and Okayama, T. (1994), "Study on stabilized zero-point of electromagnetic flowmeter with rapid excitation", In *Conference Proceedings. 10th Anniversary. IMTC/94. Advanced Technologies in I M. 1994 IEEE Instrumentation and Measurement Technolgy Conference (Cat. No.94CH3424-9)*, pp. 829–832 vol.2.

Scott, J. and Single, P. (2014), "Compact Nonlinear Model of an Implantable Electrode Array for Spinal Cord Stimulation (SCS)", *IEEE Transactions on Biomedical Circuits and Systems*, Vol. 8, No. 3, pp. 382–390.

Shercliff, J.A. (1962), *The Theory of Electro-Magnetic Flow-Measurement*, Book, Whole, C.U.P, Cambridge.

Spencer, M.P. and Denison, A.B. (1959), "The Square-Wave Electromagnetic Flowmeter: Theory of Operation and Design of Magnetic Probes for Clinical and Experimental Applications", *IRE Transactions on Medical Electronics*, Vol. ME-6, No. 4, pp. 220–228.

Strejc, V. (1980), "Least squares parameter estimation", *Automatica*, Vol. 16, No. 5, pp. 535–550.

Tarabad, M. and Baker, R.C. (1982), "Integrating electromagnetic flowmeter for high magnetic Reynolds numbers", *Journal of Physics D: Applied Physics*, Vol. 15, No. 5, pp. 739–745.

Teshima, T., Honda, S. and Tomita, Y. (1994), "Electromagnetic flowmeter with multiple poles and electrodes", In *Conference Proceedings. 10th Anniversary. IMTC/94. Advanced Technologies in I M. 1994 IEEE Instrumentation and Measurement Technolgy Conference (Cat. No.94CH3424-9)*, pp. 1221–1224 vol.3.

Teshima, T., Honda, S. and Tomita, Y. (1995), "Flow Velocity Tomography with Magnetic Flowmeter", *Proceedings of the Society of Instrument and Control Engineers*, Vol. 31, No. 8, pp. 999–1004.

Wald, A. (1940), "The fitting of straight lines if both variables are subject to error", *The annals of mathematical statistics*, Vol. 11, No. 3, pp. 284–300.

Wantzelius, D.G. and Goetz, K.L. (1977), "Circuit for automatically zeroing aortic flow base line from electromagnetic flowmeter", *American Journal of Physiology-Heart and Circulatory Physiology*.

Watral, Z., Jakubowski, J. and Michalski, A. (2015), "Electromagnetic flow meters for open channels: Current state and development prospects", *Flow Measurement and Instrumentation*, Vol. 42, No. Journal Article, pp. 16–25.

Whitaker, S. (1986), "Flow in porous media I: A theoretical derivation of Darcy's law", *Transport in Porous Media*, Vol. 1, No. 1, pp. 3–25.

Williams, E.J. (1930), "The induction of electromotive forces in a moving liquid by a magnetic field, and its application to an investigation of the flow of liquids", *Proceedings of the physical society*, Vol. 42, No. 5, p. 466.

Wollaston, C. (1881), "Discussion on 'Earth currents'", *Journal of the Society of Telegraph Engineers and of Electricians*, Vol. 10, No. 35, p. 50.

Xu, K.J. and Wang, X.F. (2007a), "Identification and application of the signal model for the electromagnetic flowmeter under sinusoidal excitation", *Measurement Science and Technology*, Vol. 18, No. 7, pp. 1973–1978.

Xu, K.J. and Wang, X.F. (2007b), "Signal modeling of electromagnetic flowmeter under sine wave excitation using two-stage fitting method", *Sensors and Actuators A: Physical*, Vol. 136, No. 1, pp. 137–143.

Yin, S. and Li, B. (2013), "A New Approach for Solving Weight Functions of Electromagnetic Flowmeters Using Resistive Network Modeling", *Journal of Applied Mathematics*, Vol. 2013, pp. 1–7.

Zhivomirov, H. (2018), "A Method for Colored Noise Generation", *Romanian Journal of Acoustics and Vibration*, Vol. 15, No. 1, pp. 14–19.